

INDONESIAN THROUGHFLOW AND ITS EFFECT
ON THE CLIMATE OF THE INDIAN OCEAN

by

Tertia Hughes

A thesis submitted to
the Faculty of Graduate Studies and Research
in partial fulfilment of
the requirements for the degree of

MASTER OF SCIENCE

Department of Meteorology
McGill University
Montréal, Québec

Copyright (c) Tertia Hughes, January 1991

ABSTRACT

An idealized box model of the Indian Ocean forced by steady winds and Haney-type surface heat fluxes is used to examine the importance of the warm fresh throughflow from the equatorial Pacific on the climate of the Indian Ocean. In particular, the hypothesis proposed by Godfrey and Weaver (1991) that the buoyancy-forced Leeuwin Current off the west coast of Australia is a manifestation of a basinwide thermohaline circulation driven by the Indonesian throughflow is examined.

The stronger Sverdrup circulation dominates the thermohaline circulation in most of the model ocean except near the eastern boundary. The effects of the throughflow can however be determined by comparing two runs forced by a Pacific Ocean with either the warm, fresh profile of the western equatorial Pacific or a cooler, more saline profile more typical of the eastern equatorial Pacific. It is found that heat imported from the Pacific is transported zonally all the way across the Indian Ocean to the western boundary by the South Equatorial Current. The enhanced meridional steric height gradient south of the SEC drives an eastward return flow back to the eastern boundary, where it turns south to form the poleward Leeuwin Current. The reverse path is traced out by the waters immediately below the thermocline. None of these features are observed when the Pacific has the cooler profile typical of the eastern boundaries of other oceans.

The western boundary currents apparently play a very minor role in this basinwide thermohaline circulation. This differs from the warm water route proposed by Gordon (1986), and supports the alternative hypothesis that the heat from the equatorial Pacific is returned to the South Atlantic via the eastward-flowing Antarctic Circumpolar Current rather than past the Agulhas Retroflexion.

The Indonesian throughflow is shown to significantly affect the surface heat fluxes and the meridional heat transport in the Indian Ocean. The role of the throughflow in maintaining the very warm climate of the Indian Ocean (a net exporter of heat) is described.

Large-scale, fairly long period (> 100 days) barotropic eddies are found in the western portion of

the basin for some solutions. The generation mechanism for these eddies appears to be barotropic instability in the model South Equatorial Current.

RESUME

Un modèle idéalisé, sans relief, forcé par des vents constants et un échange de chaleur avec l'atmosphère du type Haney (1971), est utilisé pour établir l'importance pour le climat de l'océan Indien du flux d'eau chaude et relativement peu saline provenant du Pacifique équatorial. En particulier, on désire vérifier l'hypothèse de Godfrey et Weaver (1991) selon laquelle le courant de Leeuwin longeant la côte ouest de l'Australie serait une manifestation d'une circulation thermohaline à l'échelle du bassin causée par le flux océanique à travers l'archipel indonésien.

La circulation due aux vents domine la circulation thermohaline dans la plus grande partie du domaine, sauf à proximité du littoral est. On peut cependant déterminer l'effet du flux indonésien en comparant deux simulations différant par le profil de densité dans l'océan Pacifique, qui revêt soit les caractéristiques du Pacifique équatorial ouest (donc des températures relativement élevées et des salinités relativement basses) ou soit un profil plus typique du Pacifique équatorial est (où les températures sont plus basses et les salinités plus hautes). On constate que la chaleur importée du Pacifique est transportée zonalement par le courant sud équatorial (SEC) jusqu'à la limite ouest de l'océan Indien. L'amplification du gradient méridional de hauteur stérique au sud du SEC produit un écoulement parallèle au SEC mais dans la direction opposée, qui est dévié vers le sud en s'approchant de la frontière est, formant ainsi le courant de Leeuwin en direction du pôle. Le trajet inverse est adopté par l'eau immédiatement sous la thermocline. Ces propriétés ne sont pas reproduites lorsque les températures plus froides caractéristiques du Pacifique est sont utilisées.

Les courants à la frontière occidentale de l'océan semblent jouer un rôle très mineur dans cette circulation thermohaline. Ceci diffère du trajet proposé par Gordon (1986) et appuie l'hypothèse alternative que la chaleur en provenance du Pacifique équatorial est transmise à l'Atlantique sud dans la direction est par le courant antarctique circumpolaire plutôt que dans la direction ouest en contournant la pointe de l'Afrique.

Il est montré que le transport indonésien affecte les flux de chaleur à la surface et le transport

méridional de chaleur dans l'océan Indien. La contribution au climat particulièrement chaud de l'océan Indien (un exportateur de chaleur) est décrite.

Dans la partie ouest du bassin, on retrouve des tourbillons barotropes de grandes dimensions et à période relativement longue (> 100 jours) dans plusieurs solutions. Le mécanisme pour la génération de ces tourbillons dans le modèle semble être une instabilité barotrope dans le courant sud équatorial.

ACKNOWLEDGEMENTS

I sincerely thank my supervisor, Dr Andrew J Weaver, for his excellent guidance and encouragement throughout this research project. I would also like to thank Dr J Stuart Godfrey for his very helpful advice, Prof Lawrence A Mysak for suggesting some valuable references and Mr Thierry Reynaud for helping me translate the Abstract.

During this period, I was supported financially by an NSERC research award.

CONTENTS

Abstract.....	ii
Résumé	iv
Acknowledgements	vi
Contents	vii
List of Tables	viii
List of Figures	ix
1. Introduction	1
2. Ocean Circulation Theories	11
3. The Model	14
3.1 The numerical model	14
3.2 The basin configuration and choice of parameters	17
3.3 The sequence of runs	24
4. Results	29
4.1 The wind-driven circulation	29
4.2 The thermohaline component	39
4.2.1 Consequences of the Haney surface boundary condition	39
4.2.2 The eastern boundary regimes	44
4.2.3 The basinwide circulation	47
4.3 The heat budget	61
4.4 Comparison with Godfrey and Weaver (1991)	77
4.5 Shear instability in the model South Equatorial Current	81
5. Limitations of the Model and Further Experiments	86
5.1 Difficulties with the first two runs	86
5.2 High viscosity experiments	92
6. Summary and Conclusions	115
References	119

LIST OF TABLES

Table	Page
1. Estimates of the Indonesian throughflow (taken from Gordon, 1986; Kindle et al, 1986 and Gordon, 1989)	5
2. Depths of the levels in this model and the model of Godfrey and Weaver (1991)	19
3. The sequence of runs	25
4. Heat budgets for the Leeuwin and Peru runs and for the Leeuwin and Peru runs of G-W	76
5. Heat budgets for the Leeuwin-2 and Peru-2 runs and for the Leeuwin-2 run at 5000 days	103

LIST OF FIGURES

Figure	Page
1 1. The Indian Ocean. The contours show the average salinity in the 10° to 20°C layer of the main thermocline (from Gordon, 1986). The intersections of the 20°C isotherm and the surface, and of the 10°C isotherm and the sea floor (B) are drawn as thick dashed lines	2
1 2. Observed large scale surface circulation from ship drift data during a) the North-East Monsoon and b) the South West Monsoon (taken from Woodberry et al., 1989)	4
1 3. Annual mean net downward heat flux (taken from Oberhuber, 1988). The contour interval is 25 W/m ² and the shaded areas indicate insufficient data	9
3 1. The model basin. The depth is 5000m everywhere except for the passage between the oceans, which is 1200m deep	18
3 2. The model of Godfrey and Weaver (1991), with the northward wind stress in dynes/cm ² . The depth is 5000m everywhere and a symmetry condition is imposed at the equator	18
3 3. The numerical grid for the horizontal velocities. The tracers are carried on a separate grid out of phase by a ½ interval and the vertical velocities are calculated independently for each grid	22
3 4. The apparent atmosphere temperature distribution T ^a (y) in °C (adapted from Haney, 1971)	23
3 5. Profile of zonal wind stress (in dynes/cm ²) used in our model. In G-W, the zonal component is identically zero	23
3 6. Vertical profiles of a) temperature in °C and b) salinity in ppt used as an initial condition in the Indian basin and a restoring condition in the Pacific basin. The solid line is for the Leeuwin run and the dashed line is for the Peru run	26
3 7. Kinetic energy density (in 10 ⁻¹ kg/m s ²) as a function of time a) Leeuwin run b) Peru run	28
4 1. Barotropic (vertically-integrated) streamfunction (in Sv) for a) the Leeuwin run b) the Peru run	30
4 2. Horizontal velocities at z=20m and z=60m (levels 1 and 2) a) and b) Leeuwin run c) and d) Peru run	31-32
4 3. Temperatures in °C at z=20m and z=60m (levels 1 and 2) a) and b) Leeuwin run c) and d) Peru run	34-35

4 4	Overtuning (zonally-integrated) streamfunction (in Sv) as a function of latitude for a) the Leeuwin run b) the Peru run	36
4 5	Vertical velocities in 10^{-4} cm/s at $z=40$ m and $z=80$ m (1^{st} and 2^{nd} interfaces) a) and b) Leeuwin run c) and d) Peru run Solid contours indicate upwelling and dashed contours downwelling	37-38
4 6	Velocity difference (Leeuwin - Peru) at a) $z=20$ m and b) $z=275$ m (levels 1 and 5)	40
4 7	Steric height in m along the northern boundary (with respect to a reference depth of 1600m) at $z=20$ m and $z=275$ m (levels 1 and 5) a) and b) Leeuwin run c) and d) Peru run	42
4 8	Steric height in m along the eastern boundary (with respect to a reference depth of 1600m) at $z=20$ m and $z=275$ m (levels 1 and 5) a) and b) Leeuwin run c) and d) Peru run	43
4 9	Velocity vectors at every 2^{nd} gridpoint near the eastern boundary at $z=20$ m and $z=60$ m (levels 1 and 2) a) and b) Leeuwin run c) and d) Peru run	45
4 10	Meridional-vertical section of temperature (in $^{\circ}$ C) along 113° E (two gridpoints from the eastern boundary) a) Leeuwin run b) Peru run	46
4 11	Horizontal velocities at $z=275$ m (level 5) a) Leeuwin run b) Peru run	48
4 12	Velocity vectors at every 2^{nd} gridpoint near the eastern boundary at $z=275$ m (level 5) a) Leeuwin run b) Peru run	49
4 13	Temperatures in $^{\circ}$ C at $z=275$ m (level 5) a) Leeuwin run b) Peru run	50
4 14	Meridional vertical section of temperature (in $^{\circ}$ C) along 74° E a) Leeuwin run b) Peru run	52
4 15	Meridional-vertical section of temperature (in $^{\circ}$ C) along 46° E (two gridpoints from the western boundary) a) Leeuwin run b) Peru run	54
4 16	Steric height in m along the western boundary (with respect to a reference depth of 1600m) at $z=20$ m and $z=275$ m (levels 1 and 5). a) Leeuwin run b) Peru run	55
4 17	Difference in temperature (Leeuwin - Peru) in $^{\circ}$ C at a) $z=20$ m and b) $z=60$ m (levels 1 and 2)	57
4 18	Difference in temperature (Leeuwin - Peru) along a) 113° E b) 74° E c) 46° E	58-59
4 19	Vectors of velocity difference (Leeuwin - Peru) at $z=275$ m (level 5)	60

5.4. Zonal-vertical section of temperature (in °C) at 0°N: a) Leeuwin run b) Peru run	90
5.5. Zonal-vertical section of northward velocity at 0°N: a) Leeuwin-2 run b) Peru-2 run (cf. Fig. 5.1) ..	93
5.6. Horizontal velocities at z=2750m (level 13) a) Leeuwin-2 run b) Peru-2 run (cf. Fig. 5.2)	94
5.7. Vertical velocities in 10^{-4} cm ² /s at z=2500m (interface 12) a) Leeuwin-2 run b) Peru-2 run. Solid contours indicate upwelling and dashed contours downwelling (cf. Fig. 5.3)	95
5.8. Horizontal velocities at z=20m and z=60m (levels 1 and 2): a) and b) Leeuwin-2 run c) and d) Peru-2 run (cf. Fig. 4.2)	96-97
5.9. Temperatures in °C at z=20m and z=60m (levels 1 and 2): a) and b) Leeuwin-2 run c) and d) Peru-2 run (cf. Fig. 4.3)	98-99
5.10. Zonal-vertical section of temperature (in °C) at 0°N: a) Leeuwin-2 run b) Peru-2 run (cf. Fig. 5.4)	100
5.11. Surface heat fluxes in W/m ² a) Leeuwin-2 run b) Peru-2 run. Positive (solid) contours indicate that heat is being released by the ocean (cf. Fig. 4.21)	101
5.12. Velocity difference (Leeuwin-2 - Peru-2) at a) z=20m and b) z=60m (levels 1 and 2) (cf. Fig. 4.6)	104
5.13. Difference in surface heat flux (Leeuwin-2 - Peru-2) in W/m ² . Positive (solid) contours indicate that the Leeuwin-2 ocean is releasing more heat to the atmosphere (cf. Fig. 4.22)	105
5.14. Difference in temperature (Leeuwin-2 - Peru-2) along a) 113°E b) 74°E c) 46°E (cf. Fig. 4.18)	105-106
5.15. Horizontal velocities at z=275m (level 5): a) Leeuwin-2 run b) Peru-2 run (cf. Fig. 4.11)	108
5.16. Temperatures in °C at z=275m (level 5): a) Leeuwin-2 run b) Peru-2 run (cf. Fig. 4.13)	109
5.17. Overturning (zonally-integrated) streamfunction in Sv as a function of latitude for a) the Leeuwin-2 run b) Peru-2 run (cf. Fig. 4.4)	110
5.18. Kinetic energy density in 10^{-1} kg/m s ² for a) the Leeuwin-2 run b) the Peru-2 run (cf. Fig. 3.7)	111
5.19. Total northward heat transport in 10^{15} W a) Leeuwin-2 run b) Peru-2 run (cf. Fig. 4.23a)	112
5.20. Total northward heat transport in 10^{15} W at 2800 days a) Leeuwin-2 run b) Peru-2 run	113

1. INTRODUCTION

The Indian Ocean is the smallest and the warmest of the world's three major oceans. With the Red Sea and the Persian Gulf, it occupies nearly 15% of the globe, but most of its area is in the southern hemisphere (Fig.1.1). The Subtropical Convergence at roughly 40°S is often taken as the southern boundary, although the Indian Ocean does exchange water with the Antarctic Circumpolar Current. The ocean floor is very flat over large regions but as in the Atlantic, the bed is scarred by a fairly prominent mid-ocean ridge, as well as by a number of submarine canyons, some related to the three large rivers discharging into the basin in the north, the Ganges, the Indus and the Brahmaputra (Ross, 1988). The Indian subcontinent divides the northern ocean into the Arabian Sea, noted for its high surface salinity due to evaporation, and the Bay of Bengal, with a fresh surface layer caused by river runoff (Pickard and Emery, 1982). In the east, the only fairly deep passages into the Indian Ocean through the Indonesian Archipelago are two channels 1200 to 1500 metres deep on either side of Timor Island, although water from the Banda and Arafura Seas may also pass over the broad shallow northwest shelf of Australia. The temperature and salinity profiles in the Indonesian seas have been found to be virtually homogeneous with those of the western equatorial Pacific (Levitus, 1982).

The Indian Ocean is fascinating to physical oceanographers first and foremost because of its seasonally reversing equatorial circulation driven by the monsoon winds. In the subtropics, the counter-clockwise gyre circulation is similar to that in other southern oceans, and during the North-East Monsoon (November to March), the westward North Equatorial Current (NEC), the eastward Equatorial Countercurrent (ECC) and the westward South Equatorial Current (SEC) are analogous to those in the Atlantic and Pacific Oceans, if a bit further south. But during the South-West Monsoon (May to September), the NEC and the ECC are replaced by the eastward Monsoon Current and the fast northward-flowing Somali Current appears along the coast of Somalia

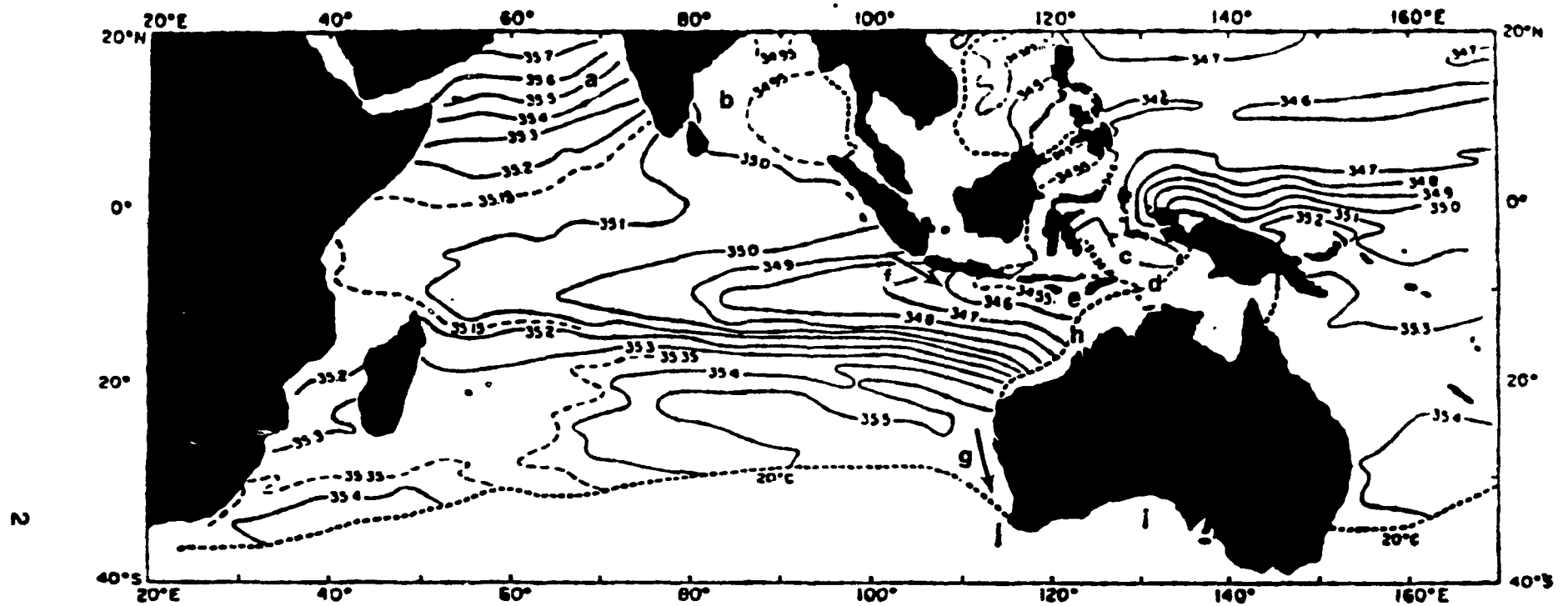


Fig.1.1. The Indian Ocean. The contours show the average salinity in the 10° to 20°C layer of the main thermocline (from Gordon, 1986). The intersections of the 20°C isotherm and the surface, and of the 10°C isotherm and the sea floor are represented by thick dashed lines.

- | | |
|------------------|---------------------------|
| a. Arabian Sea | f. South Java Current |
| b. Bay of Bengal | g. Leeuwin Current |
| c. Banda Sea | h. Northwest Shelf |
| d. Arafura Sea | i. Great Australian Bight |
| e. Timor Island | j. Cape Leeuwin |

(Fig.1.2). A persistent double eddy circulation has repeatedly been observed in the coastal circulation off Africa during this season.

Numerical modellers have been successful in reproducing many of these features (reviewed in Knox and Anderson, 1985, and Luther, 1987), however the emphasis has usually been on the dynamics of the western boundary currents or the Equatorial Undercurrent, and the role of the throughflow from the Pacific has not been fully considered. For example, Woodberry et al. (1989) presented a realistic simulation of the large scale surface circulation in the Indian Ocean which captured many of the observed seasonal variations; however, the model failed to reproduce the eastern boundary currents (Leeuwin Current and Undercurrent, South Java Current) in part because an Indonesian throughflow was not imposed.

The flow of fresh western tropical Pacific water through the relatively shallow passages of the Indonesian Archipelago may be tracked as strong tongues of low salinity water extending zonally more than halfway across the Indian Ocean (Godfrey and Golding, 1981). The magnitude of the net mass transport has unfortunately not been clearly established. The direction of the throughflow is agreed upon, as is the seasonal cycle (minimum during the southern hemisphere summer and maximum in winter), but estimates of the annual mean transport range from 2 Sv to 18 Sv (see Table 1). The Indonesian throughflow is thought to be directly responsible for the weakness of the East Australian Current in the Pacific and the strength of the South Equatorial Current in the Indian Ocean (Godfrey and Golding, 1981), and indirectly responsible for the anomalous Leeuwin Current off the west coast of Australia. It is a crucial link in the 'warm water route' proposed by Gordon (1986) as part of a global thermohaline circulation connecting the world's oceans. Gordon speculated that deep water formed in the North Atlantic is transported into the Pacific (and to a lesser extent, the Indian Ocean) via the Antarctic Circumpolar Current and rises through the thermocline. Some of the warmed water then passes into the Indian Ocean and is advected right across it by the South Equatorial Current to join the rapid poleward Agulhas Current along Africa. The thermocline water that escapes the Agulhas Retroflexion at the southern tip of Africa flows into the South Atlantic, contributing to the

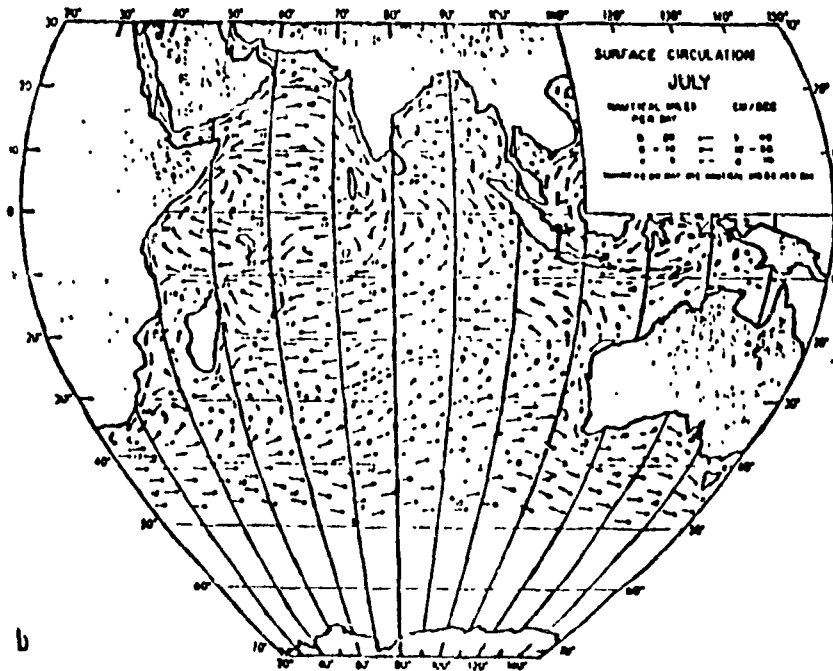
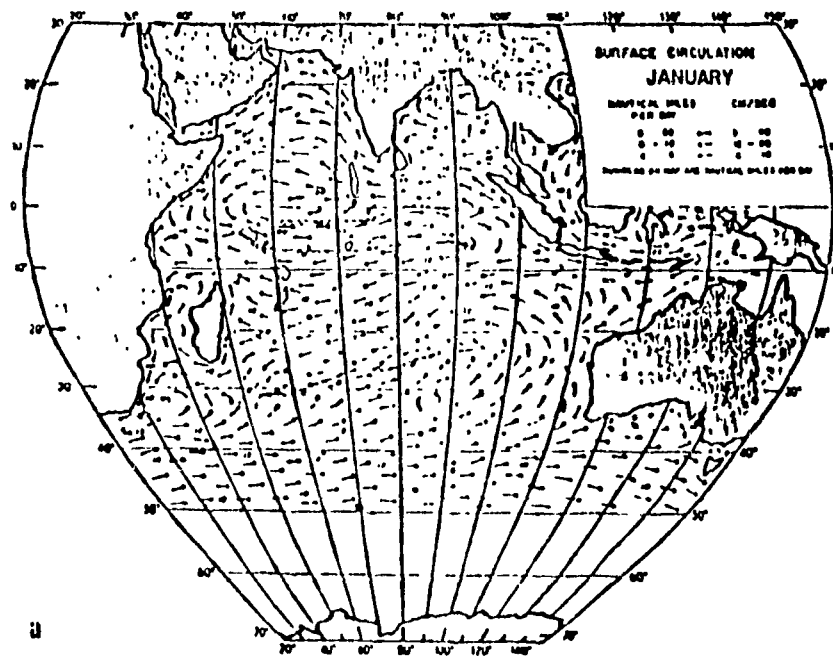


Fig.1.2. Observed large scale surface circulation from ship drift data during a) the North-East Monsoon and b) the South-West Monsoon (taken from Woodberry et al., 1989).

TABLE 1

Estimates of the Indonesian Throughflow
(taken from Gordon, 1986, Kindle et al., 1986 and Godfrey, 1989)

Wyrki (1961a)	1 to 2.5 Sv	seasonal surface transport based on dynamic heights
Cox (1975)	18 Sv	GCM
Godfrey and Golding (1981)	10 Sv	based on depth-integrated steric height P
Gordon and Piola (1983)	14 Sv	advective box model
Fine (1985)	5 Sv	box model of tritium distributions
Fu (1986)	7 Sv	inverse method applied to six Indian Ocean stations
Gordon (1986)	8.5 Sv	assuming 20 Sv production rate for NADW, uniform upwelling in the world ocean and "cold water route" is insignificant
Kindle, Heburn and Rhodes (1986)	2 to 12 Sv	seasonal reduced-gravity model
Godfrey (1989)	16 Sv 10-13 Sv	P Levitus data, assuming geostrophic balance for the throughflow

unique northward heat flux there.

However, the intention here is not to follow the mass transported through the Indonesian Archipelago but to examine the role of the throughflow as a means of purely thermohaline forcing. The transport of heat into the Indian Ocean by the inflow of warm western equatorial Pacific surface waters and the subsequent release of the heat to the atmosphere may be found to contribute to the climate of the Indian Ocean even neglecting the role of the net mass throughflow. This hypothesis was first proposed by Godfrey and Weaver (1991, hereafter referred to as G-W), who, in modelling the Leeuwin Current along the eastern boundary, found it to be part of a basin-wide thermohaline circulation, driven by cooling of warm west Pacific waters.

The Leeuwin Current is very different from eastern boundary currents in other oceans. For example, the equatorward Peru Current at the same latitude off South America is a typical broad slow eastern boundary current, carrying cool water northward from higher latitudes to complete the anticyclonic subtropical gyre in the South Pacific. (Pickard and Emery, 1982) Equatorward winds drive upwelling at the coast. Quite the opposite is seen off Australia, where the fast narrow Leeuwin current actually accelerates poleward into the prevailing winds. In fall and winter (for the southern hemisphere), the current is a shallow (< 300 m) stream of warm low-salinity water centred at the shelf break, with speeds of up to 1.8 m/s, as described by Church et al. (1988) The current deepens poleward, and its width shrinks from about 200 km to less than 100 km. A deep thermocline (> 50 m) and downwelling are associated with low biological productivity (Batteen and Rutherford, 1990). In summer, the flood of fresh tropical water over the Northwest Shelf is partially blocked by a local reversal of the flow there, but current meters at the shelf edge west of Australia still measure poleward velocities (Boland et al., 1988). The coastal circulation is however weaker and the TS characteristics are closer to those of the interior, where northeastward flow (known as the West Australian Current) is observed (Church et al., 1988). The net mass transport by the Leeuwin Current is probably negligible, because of the presence of an equatorward undercurrent (Godfrey and Ridgway, 1985); however, large amounts of heat must be transferred southward by the surface flow, which can be

traced all the way into the Great Australian Bight in infrared satellite photos (Church et al., 1988).

Numerous investigations into the unique large meridional steric height gradient off western Australia and its reversal with depth, forming the Leeuwin Current-Undercurrent system, have led researchers to discard the Indonesian throughflow as the direct source of the distinctive eastern boundary regime, as most of this water continues westward across the ocean. It is the warm temperatures of the west Pacific which are communicated to the equatorial Indian Ocean, which are of utmost importance. Godfrey and Golding (1981) first speculated that the existence of the Leeuwin Current depended on the presence of the throughflow while Godfrey and Ridgway (1985) subsequently suggested that the longshore steric height gradient was also related to the throughflow.

Kundu and McCreary (1986) found that, in a model without vertical mixing, no Leeuwin Current could be produced. With vertical mixing, a small part of the model throughflow could be induced to bend southward but the resulting coastal circulation did not conform to observations of the Leeuwin Current. The first successful model of the current was that of McCreary, Shetye and Kundu (1986) who used a meridional density gradient to force a geostrophically balanced onshore flow at the surface. The reversal of the density gradient at a deeper level produced the undercurrent. They also generated seasonal variability by modulating the longshore wind. Another aspect of the problem was solved by Thompson (1987), who showed that if the wind-mixed layer near an eastern boundary is deep enough, the longshore pressure gradient can force downwelling despite an upwelling-favourable wind. He modelled the Leeuwin Current as a surface-trapped flow braked by offshore transport in a bottom frictional layer. The experiments of Weaver and Middleton (1989, 1990) confirmed that the seasonal warm water flood over the Northwest Shelf served to enhance the current locally but that the fundamental cause of the poleward-intensifying current was the geostrophically-balanced onshore flow. They described a linear analytic model that demonstrated the balance between the pressure gradient forcing and bottom friction, and they noted the importance of the shelf break in trapping the longshore current.

Most recently, simulations by G-W have shown that the Leeuwin Current is linked to convective

processes, as first suggested by Godfrey and Ridgway (1985). South of about 20°S, heat is lost to the atmosphere at the surface, causing the vertical density profile to become unstable. This is very different from the eastern boundaries of the Pacific and Atlantic Oceans, where annual mean heat flux maps show a net heat gain between about 40°N and 40°S (Fig.1.3). G-W found that in their model the convectively mixed layer deepened poleward as the temperature of the overlying atmosphere decreased. The meridional gradients of temperature and density that developed in the upper model layers drove the onshore zonal geostrophic flow, which turned south at the boundary, in keeping with mass continuity. G-W also demonstrated that, in the absence of both a Sverdrup circulation and a net mass throughflow, the replacement of the Pacific heat source by a reservoir whose temperatures and salinities were closer to those off South America could change the eastern boundary regime from a Leeuwin Current-like behaviour to a flow more reminiscent of the Peru Current, a more typical equatorward eastern boundary current.

The purpose of this study is to follow up on the observation of G-W that the heat imported from the warm Pacific could be tracked all the way around the reduced Indian Ocean basin in their model. In much of the real Indian Ocean, the Sverdrup relation is thought to give the best first approximation to the circulation (Godfrey and Golding, 1981; Godfrey, 1989), while the weaker thermohaline flow would manifest itself most clearly in the Leeuwin Current at the eastern boundary where the Sverdrup forcing is weak. By comparing the advection of heat in an idealized Indian Ocean basin, forced by a near-equatorial throughflow from either a warm reservoir resembling the western tropical Pacific or a cooler one representing the equatorial waters off South America, we hope to determine the importance of the heat transport through the Indonesian Archipelago, in the presence of an average wind stress and a simplified heat exchange with the atmosphere over a realistic surface area. The results of G-W suggest that the effects on the surface heat flux fields of changing the temperature and salinity profile of the Pacific are not confined to the neighbourhood of the eastern boundary but may affect the entire Indian Ocean.

The outline of this thesis is as follows. In Chapter 2, a brief qualitative review of the pertinent

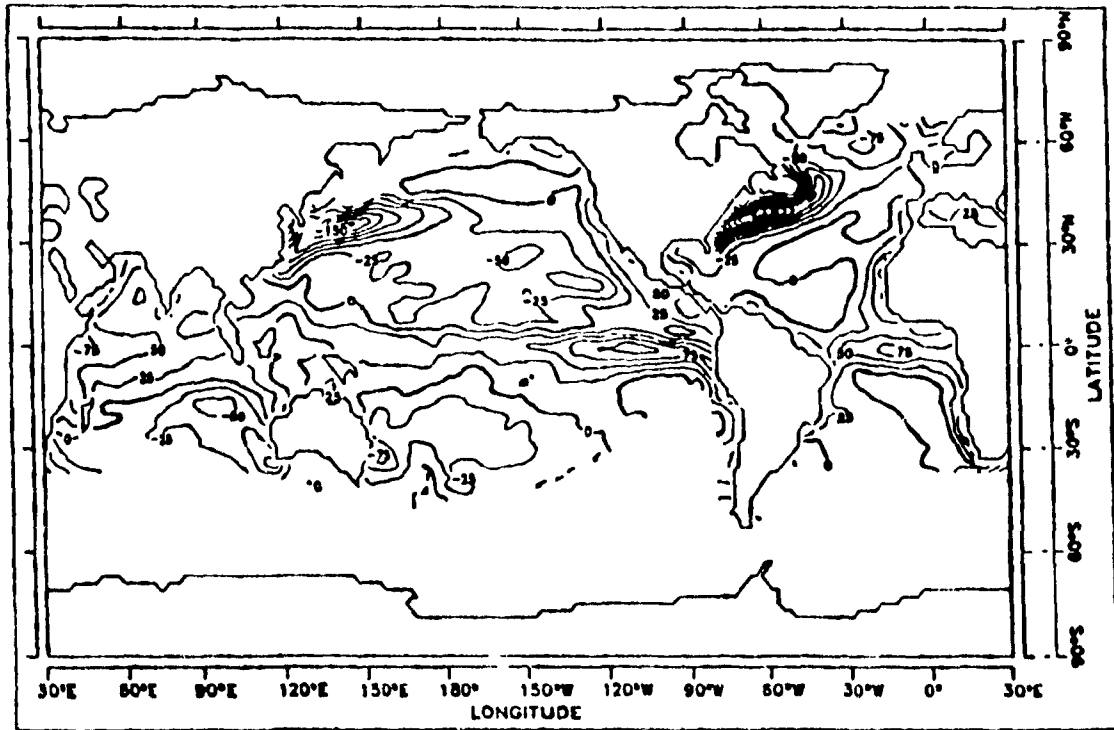


Fig.1 3. Annual mean net downward heat flux from Oberhuber (1988). The contour interval is 25 W/m^2 and shaded areas indicate insufficient data.

theories of the wind-driven and thermohaline components of the ocean circulation is given. In Chapter 3, the numerical model is presented, followed by a description of the basin configuration and the sequence of runs. The model results are discussed in Section 4: the wind-driven component, which is common to all runs, is described first, then the thermohaline circulation, and especially the differences in the circulation as forced by either a warm or a cool throughflow. The effects on the heat budget are examined and a comparison is made with the results of G-W. In Chapter 5, the shortcomings of the model and two additional runs that were done to resolve some of these difficulties are mentioned, and in Chapter 6, a summary and the conclusions are given.

2. OCEAN CIRCULATION THEORIES

The purpose of this chapter is only to give a brief qualitative description of the ocean circulation theories invoked in later chapters, the full development can be found in Gill (1982) or Pond and Pickard (1983) among others.

The response of the ocean circulation in the upper one thousand metres is thought to be governed by the wind driving (Pond and Pickard, 1983). The frictional stress by the surface wind directly forces the surface Ekman current that dies away over a characteristic depth of order one hundred metres. The Coriolis force due to the Earth's rotation causes the current to spiral vertically; although this is nearly impossible to observe outside a laboratory, it has the consequence that the transport in the shallow Ekman layer is rotated 90 degrees to the right (left) in the northern (southern) hemisphere. The convergence or divergence of the Ekman circulation also creates pressure gradients and downwelling or upwelling to depths ten times greater. The total mass transport above the depth of no motion can be calculated from the Sverdrup equation, which establishes the proportionality between the depth-integral of the northward transport and the wind stress curl. The inclusion of friction allowed Stommel to show that, on a rotating planet, the principle of conservation of vorticity could only be satisfied by an asymmetric circulation with intensified currents and lateral shear on the western side. The first comprehensive solution for the wind-driven circulation in a flat-bottomed ocean was given by Munk in 1950. He included realistic winds, a meridionally varying Coriolis parameter (β -plane approximation) and both lateral and vertical friction, however he left out the density-driven contribution, as well as the inertial effects which are important in the intensified western boundary currents.

The large scale upper-ocean circulation in the world ocean is in general very well described by the barotropic streamfunction calculated from the wind stress distribution. But the circulation is also modified in important ways by the surface fluxes of heat and salt which drive the deep baroclinic

thermohaline circulation. A description of the purely thermohaline overturning induced by the differential solar heating on a hemisphere is given by K. Wyrki (1961b). A shallow layer of water is warmed in equatorial regions and travels poleward in either hemisphere. As it approaches the high latitudes, heat is lost to the rapidly cooling (because of its lower heat capacity) atmosphere and the densifying water may be compelled to sink if its salinity is high or if the surface winds are forcing Ekman convergence in the upper layers. The cooled deep water spreads equatorward and, on very long time scales, diffuses, upward through the thermocline. However, the deep sinking of dense ice-cold water happens at only a few locations in the world today, and there because exceptional conditions prevail. The Ross and Weddell Seas in the southern hemisphere are the only known sources of bottom water.

On a rotating planet, the thermohaline circulation acquires a zonal component. Zonally oriented surface isotherms in the geostrophic interior of the oceans are balanced by eastward flow in both hemispheres, forcing a zonal-vertical cell

However, in most sectors of the ocean, the weaker density-driven flows are subordinate to the wind-forced currents. The large-scale circulation in the subtropical oceans in either hemisphere consists of a basin-wide anticyclonic gyre, with weak equatorward flow over most of the ocean's width and a fast narrow poleward western boundary current closing the loop. The essential redistribution of heat from the equator to the polar regions is now the responsibility of the western boundary current, which starts its journey in the warm water masses of the low latitudes and returns poleward the mass from both the slow equatorward flow over the rest of the basin and the upward diffusion of the deep water (Wyrki, 1961). A horizontal circulation gyre is however usually less effective in transporting heat than an overturning cell because the temperature variation along a latitude circle is less than the difference between the deep ocean and the thin surface layer (Bryan, Manabe and Pacanowski, 1975).

Stommel (1965) showed that the thermohaline circulation can be thought of as an internal mode in the mass transport, vanishing in a vertical integral, but weakening or reinforcing the wind-driven currents at any particular depth. Bryan, Manabe and Pacanowski (1975) noted that the Ekman

transport associated with the trade winds favours an efficient meridional thermohaline overturning cell at low latitudes, but that at higher latitudes, the westerly winds and the thermohaline circulation are opposed.

Finally, a complete ocean theory must take into account the coupling of the barotropic and baroclinic components. The two interact through the nonlinear terms in the momentum equations, through the advection terms in the conservation equations for heat and salt, and through the joint effect of baroclinicity and relief (JEBAR), in which the baroclinic mode contributes a term to the depth-averaged vorticity equation because of the non-uniform bottom topography (Holland, 1973). Although they are not the main focus of climate studies, transient effects such as internal and external waves and tidal motions may also be mentioned as some of these are instrumental in establishing the final equilibrium.

3. THE MODEL

3.1. The Numerical Model

The numerical model we have used is the Cox (1984) version of the Bryan-Cox primitive equation ocean general circulation model. The equations are formulated in spherical coordinates ($z, \lambda, \phi =$ depth, longitude, latitude) and seven variables are solved for: the zonal, meridional and vertical components of velocity u, v and w , the pressure p , the density ρ , the potential temperature T and the salinity S . A small number of fundamental assumptions enter into the construction of the seven model equations. The Boussinesq approximation justifies the neglect of small local variations about the mean density in the two horizontal momentum equations:

$$(1) \frac{\partial u}{\partial t} + L[u] \cdot v = \frac{-1}{\rho_0 a \cos \phi} \frac{\partial p}{\partial \lambda} + A_{TV} \frac{\partial^2 u}{\partial z^2} + A_{TH} \left\{ \frac{\nabla^2 u + (1 - \tan^2 \phi)u}{a^2} - \frac{2 \sin \phi}{a^2 \cos^2 \phi} \frac{\partial v}{\partial \lambda} \right\}$$

$$(2) \frac{\partial v}{\partial t} + L[v] + fu = \frac{-1}{\rho_0 a} \frac{\partial p}{\partial \phi} + A_{TV} \frac{\partial^2 v}{\partial z^2} + A_{TH} \left\{ \frac{\nabla^2 v + (1 - \tan^2 \phi)v}{a^2} + \frac{2 \sin \phi}{a^2 \cos^2 \phi} \frac{\partial u}{\partial \lambda} \right\}$$

where $L[a]$ is the advection operator:

$$L[a] = \frac{1}{a \cos \phi} \left\{ \frac{\partial (ua)}{\partial \lambda} + \frac{\partial (va \cos \phi)}{\partial \phi} \right\} + \frac{\partial (wa)}{\partial z}$$

∇^2 is the horizontal Laplacian:

$$\nabla^2 a = \frac{1}{a^2 \cos^2 \phi} \left\{ \frac{\partial^2 a}{\partial \lambda^2} + \frac{\partial (a \cos \phi)}{\partial \phi} \frac{\partial a}{\partial \phi} \right\}$$

and f is the Coriolis parameter: $f = 2\Omega \sin\phi$.¹ The vertical momentum equation is reduced to the hydrostatic approximation by the assumption that the vertical scale of the motion is small compared to the horizontal scale:

$$(3) \quad \frac{\partial p}{\partial z} = -\rho g$$

The continuity equation appropriate for the oceans is the version for incompressible fluids:

$$(4) \quad \frac{1}{a \cos\phi} \frac{\partial u}{\partial \lambda} + \frac{1}{a \cos\phi} \frac{\partial (v \cos\phi)}{\partial \phi} + \frac{\partial w}{\partial z} = 0$$

The flow is assumed to conserve heat and salt:

$$(5) \quad \frac{\partial T}{\partial t} + L[T] = A_{TV} \frac{\partial^2 T}{\partial z^2} + A_{TH} \nabla^2 T$$

$$(6) \quad \frac{\partial S}{\partial t} + L[S] = A_{TV} \frac{\partial^2 S}{\partial z^2} + A_{TH} \nabla^2 S$$

and the equation of state gives density as a polynomial expansion in T , S and p :

$$(7) \quad \rho = \rho(T, S, p)$$

Small-scale processes causing mixing of momentum and of heat or salt are parametrized by lateral and vertical viscosities (A_{TH}, A_{TV}) and diffusivities (A_{TH}, A_{TV}). This can also be thought of as a way of providing closure for the equations formulated in terms of mean and eddy quantities. The rigid lid approximation ($w=0$ at $z=0$) is made, so as to eliminate high frequency external gravity waves. The

¹ In the Cox (1984) version of the model, the terms $-uv \tan\phi/a$ and $+u^2 \tan\phi/a$ on the left-hand sides of equations (1) and (2) respectively, representing the curvature of the Earth in the expansion of the nonlinear terms, were neglected as they are small.

no-slip ($u,v=0$) condition is imposed on all lateral boundaries and with the rigid lid approximation, this allows the construction of a barotropic streamfunction which is constant on boundaries. No normal tracer flux (zero gradient of T and S) is allowed through solid boundaries. Bottom friction is quadratic in velocity with a 10° turning angle (Gill, 1982):

$$(8) \quad (\tau^{\lambda b}, \tau^{\phi b}) = \rho_0 c_0 [u^2 + v^2]^{\frac{1}{2}} (u \cos \alpha - v \sin \alpha, u \sin \alpha + v \cos \alpha)$$

where $c_0 = 1.3 \times 10^{-3}$ and $\alpha = [-10^\circ$ for $\phi > 0$, 0° for $\phi = 0$, $+10^\circ$ for $\phi < 0$].

The model equations are solved using centred time (leapfrog) differencing for the advective terms (with forward Euler timesteps at regular intervals to prevent the solution splitting) and forward differencing for the diffusive terms. The Coriolis term is handled semi-implicitly so as to allow a time step longer than the inertial period, and so is the hydrostatic component of pressure, to partially filter the internal waves. The finite differencing scheme conserves energy, apart from dissipative effects, in the sense that the nonlinear terms in the momentum equations do not act as a source of fictitious kinetic energy, and also exchanges between the kinetic and potential energy pools are accomplished without leakage (Semtner, 1986). The grid structure is composed of rectangular elements and follows the Arakawa B-scheme, in which horizontal velocities and tracers (e.g. temperature and salinity) are carried on separate meshed grids, and vertical velocity is calculated at levels intermediate between the main grids (see Cox (1984) or Semtner (1986) for further details).

The coupling to the atmosphere is accomplished by prescribing the wind stress τ as a body force in the top model layer:

$$(9) \quad \frac{A_{MV}}{\partial z} \partial (u,v) = \frac{(\tau^\lambda, \tau^\phi)}{\rho_0}$$

and the surface fluxes of heat and salinity. The Ekman spiral in the wind-mixed layer is not resolved, but the depth-integrated transport is legitimized by rotating currents in the surface layer 90° to the right (left) in the northern (southern) hemisphere. Convection is handled implicitly: when the density

profile in the water column becomes unstable, the vertical diffusivity is increased to 1×10^4 cm²/s in the unstable layers, causing them to mix virtually completely over one timestep.

3.2. The Basin Configuration and Choice of Parameters

Following the example of G-W, we have designed a simple rectangular, flat-bottomed ocean basin five kilometres deep everywhere and driven by steady winds. (Fig.3.1) The 'Indian' and 'Pacific' basins are adjacent and are linked by a single channel 1200 metres deep between 8°S and 13°S. A strip of ocean has been included south of 'Australia' (the narrow L-shaped land wall dividing the Pacific and Indian basins south of the gap) as this area is potentially important in the surface heat budget. This also allows for realism in the neighbourhood of Cape Leeuwin (14°E, 35 4°S). The Pacific Ocean in these simulations is simply a reservoir restored to its initial temperature and salinity profiles with a 2.5-day e-folding timescale. The boundaries are vertical walls at 15°N, 44°E, 40°S and 130°E; the artificial 'Pacific' occupies the region east of 115.2°E and north of 33.2°S, so the model Indian Ocean is 70° wide (except for south of Australia where it extends another 16° east into the Great Australian Bight) and 55° meridionally. This represents an expansion of the basin used by G-W (Fig.3.2), which was bounded by 0°N, 84°E, 40°S and 130°E. In their model, the Indonesian opening was right on the equator (from 0°N to 5°S) and was the same depth as the oceans it divides. They used a symmetry boundary condition at the equator since they had no northern hemisphere. Also, seventeen levels of increasing thicknesses in the vertical (Table 2) are used here while G-W had only ten. Such high vertical resolution is to discourage the generation of spurious equatorial cells in the overturning streamfunction, following Weaver and Sarachik (1990); this is particularly relevant in the present study where the system is more energetic than in G-W. In both models, the enclosed ocean requires zero net mass transport through the Indonesian passage.

The eddy coefficients used to parametrize the sub-grid scale mixing of momentum and temperature reproduce the choices of G-W. The horizontal diffusivity A_{TH} is set to 8×10^6 cm²/s

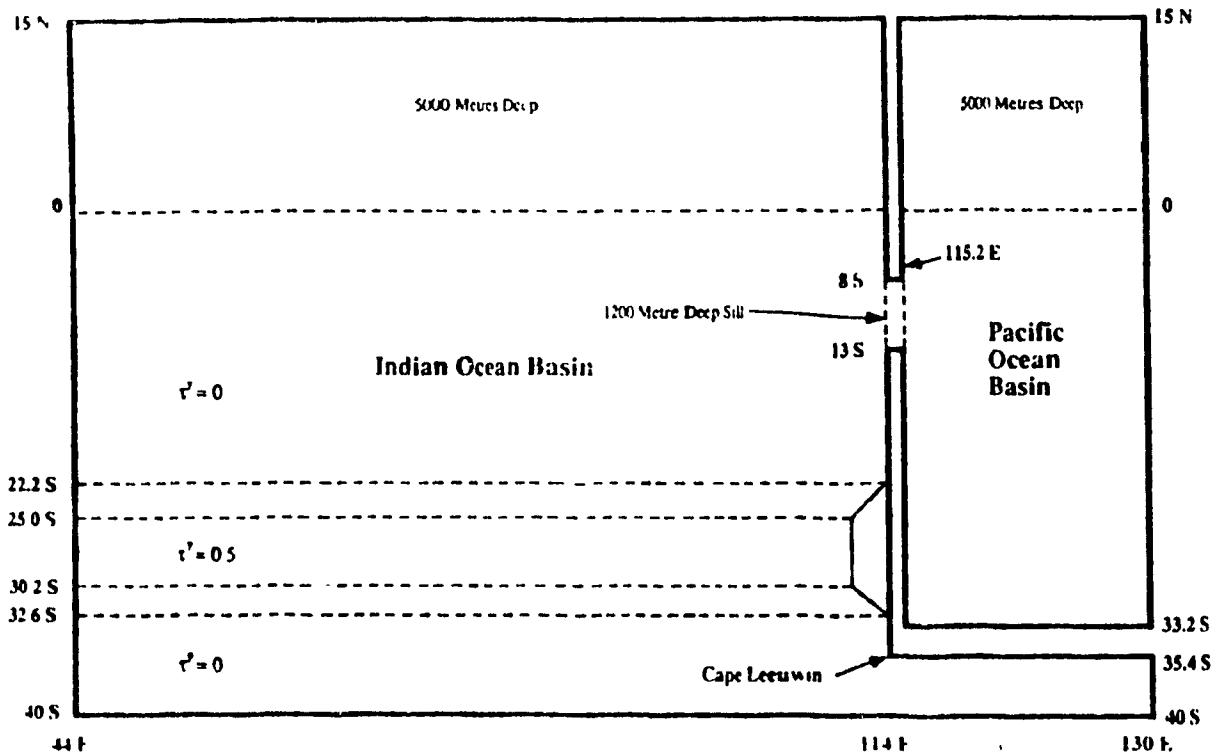


Fig.3.1. The model basin. The depth is 5000m everywhere except for the passage between the two oceans, which is 1200m deep.

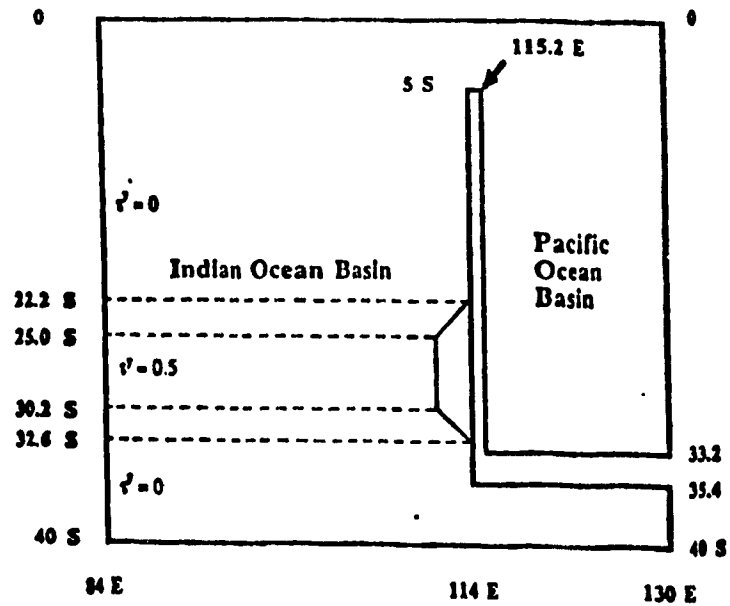


Fig.3.2. The model of Godfrey and Weaver (1990), with the northward wind stress in dynes/cm². The depth is 5000m everywhere and a symmetry condition is imposed at the equator.

Level	This model	Model of G-W
1	40 m	40 m
2	80 m	80 m
3	140 m	140 m
4	220 m	230 m
5	330 m	360 m
6	470 m	640 m
7	660 m	960 m
8	900 m	1600 m
9	1200 m	3200 m
10	1600 m	5000 m
11	2000 m	
12	2500 m	
13	3000 m	
14	3500 m	
15	4000 m	
16	4500 m	
17	5000 m	

¹ Horizontal velocities and tracers are calculated at the midpoints of each level and vertical velocities are calculated at interfaces.

everywhere, while the vertical diffusivity A_{TV} increases with depth from $A_{TVS}=0.2 \text{ cm}^2/\text{s}$ to $A_{TVB}=1.4 \text{ cm}^2/\text{s}$ according to the formula (Bryan and Lewis, 1979):

$$(10) \quad A_{TV} = (A_{TV2500} + C_z \tan^{-1}[4.5 \times 10^{-3} \times (z - 2.5 \times 10^3)]) \text{ cm}^2/\text{s}$$

where $A_{TV2500} = 0.8 \text{ cm}^2/\text{s}$ is the vertical diffusivity at a depth of 2500 metres and the range between top and bottom is given by $C_z = 1.2 \text{ cm}^2/\text{s}$. The vertical eddy viscosity A_{VV} has a uniform value of $1.0 \text{ cm}^2/\text{s}$ but the horizontal viscosity A_{MH} varies linearly with zonal grid spacing:

$$(11) \quad A_{MH} = \Delta x_u \times 10^8 \text{ cm}^2/\text{s}$$

where Δx_u is the zonal grid spacing in degrees. (This is done to satisfy the grid Reynolds numerical stability criterion as discussed below.) In general, it is desirable that A_{TH} and A_{MH} be as small as possible in order to not obscure the transports of heat and salt by currents (Holland, 1973). A_{TV} is of critical importance in obtaining a realistic depth for the thermocline. A_{VV} is invoked in calculating the depth of the Ekman layer, but as Holland (1973) points out, this is not of importance except near the equator, where the Ekman depth exceeds the depth of the first model layer. The selection of the mixing coefficients is however also motivated by considerations of numerical stability. A viscous boundary layer must be resolved at the solid boundaries where the no-slip condition is imposed (Bryan, 1986):

$$(12) \quad A_{MH} > \frac{\beta(2\Delta_H)^3}{\pi\sqrt{3}} \quad \text{where } \Delta_H \text{ is the x or y grid spacing}$$

and there is a restriction on the grid Reynolds number when a centred differencing scheme is used:

$$(13) \quad \text{Re}_H = \frac{U\Delta_H}{A_{MH}} < 2$$

(A similar condition on the Péclet number involving A_{TH} need not be verified as the computational

mode in the density field will be suppressed by the viscosity in the momentum equation through geostrophy.)

The grid laid out by G-W was designed to focus especially on the eastern boundary region, to best resolve the Leeuwin Current. We have kept this arrangement, although our ocean basin is now much wider. The variable grid spacing is 0.4° by 0.4° off Australia but is gradually increased to 1.0° by 1.0° as we move north and west (Fig 3.3). The highly artificial Pacific Ocean is of no dynamical interest, so the zonal grid length has been further relaxed there, attaining 1.5° in the extreme east. (An extremely weak computational mode is in fact excited in the Pacific, as can be seen in Fig 4.1 from the checkerboard pattern of the zero contour in the barotropic streamfunction in that basin, but this should not have further consequences for the outcome of the experiment.)

The parametrization of the heat exchange at the air-sea interface has the form proposed by Haney (1971):

$$(14) \quad Q(x,y) = -\lambda [T(x,y) - T^*(y)] = -\rho_0 C_p \frac{\Delta z_1}{\tau_R} [T(x,y) - T^*(y)]$$

where T^* is an apparent atmospheric temperature, a function of latitude only (Fig.3.4), $T(x,y)$ is the ocean temperature at the first model level, $C_p=4000 \text{ J/(kg } ^\circ\text{C)}$ is the specific heat of water at constant pressure and $\rho_0=1000 \text{ kg/m}^3$ is a reference density. The coefficient λ is set to $36 \text{ W/(m}^2 \text{ } ^\circ\text{C)}$, which is equivalent to forcing the surface layer of depth $\Delta z_1 = 40 \text{ m}$ to the apparent atmospheric temperature $T^*(y)$ with a $\tau_R = 51 \text{ day}$ timescale. The Haney forcing represents the effect of a steady, zonally uniform atmosphere exchanging heat with the ocean through radiative, sensible and latent heat fluxes. The apparent temperature is based upon annual mean values for the surface air temperature, the relative humidity and the surface wind speed. The Haney-type boundary condition is widely used, however, Bryan (1986) has pointed out that the efficient forcing of the surface layer to a zonal temperature distribution may introduce a bias into the meridional heat transport

Surface fluxes of salinity are assumed to be of secondary importance and no form of salinity

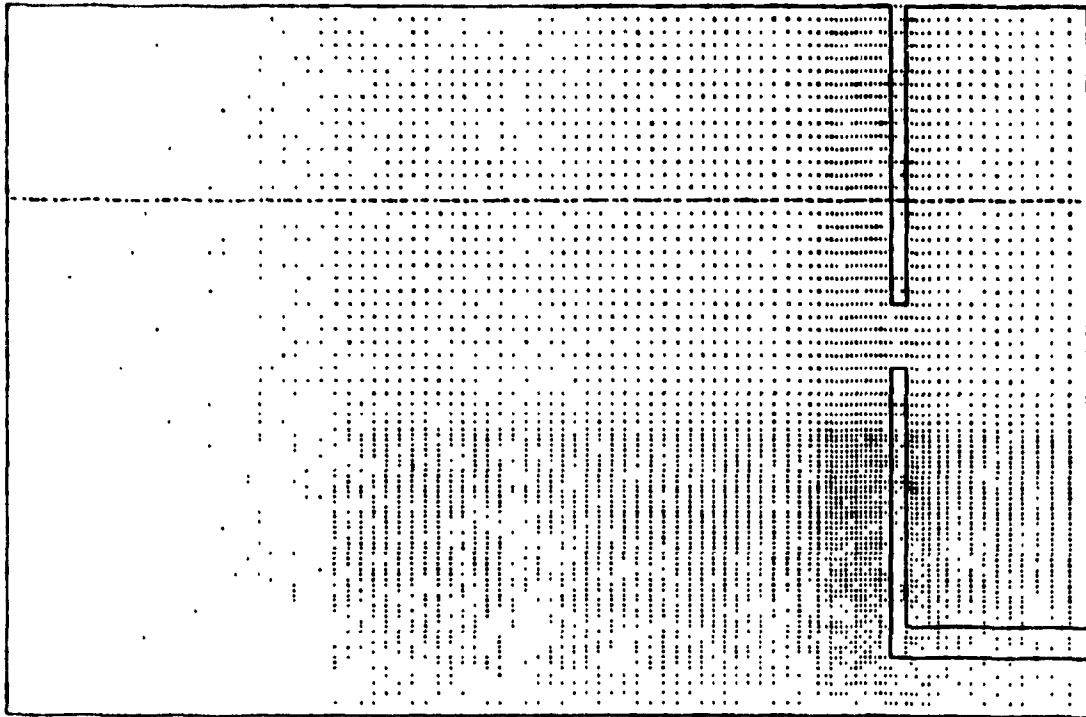


Fig.33. The numerical grid for horizontal velocities. The tracers are carried on a separate grid out of phase by a $\frac{1}{2}$ interval and vertical velocities are calculated independently for each grid.

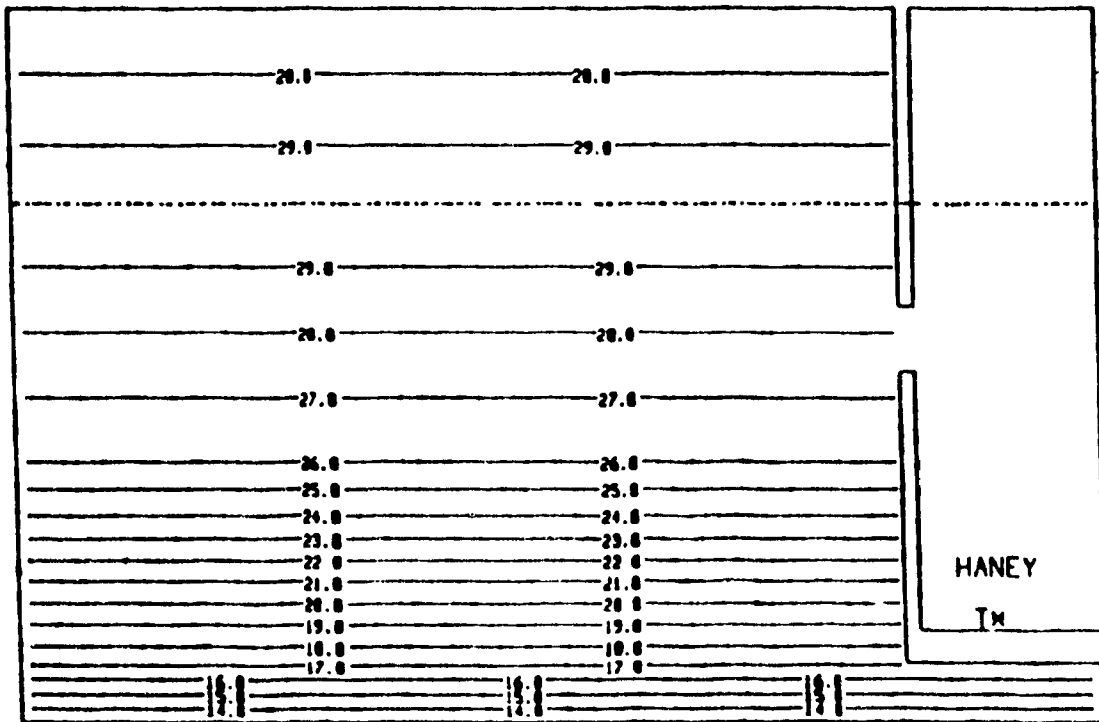


Fig.3.4. The apparent atmosphere temperature distribution $T^*(y)$ in $^{\circ}\text{C}$ (adapted from Haney, 1971).

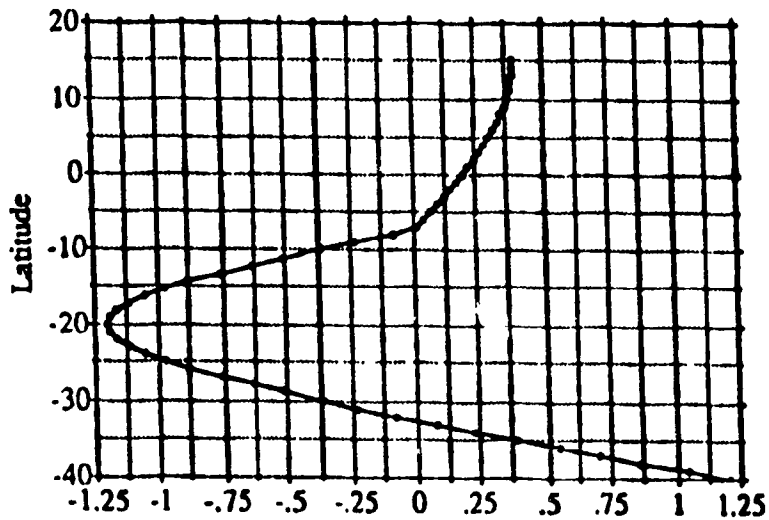


Fig.3.5. Profile of zonal wind stress (in dynes/cm²) used in our model (eastward positive). In G-W, the zonal component is identically zero.

forcing other than the throughflow has been imposed.

The meridional component of the imposed wind matches the wind stress used by G-W. It consists of a band of northward wind stress with a constant value of 0.5 dynes/cm^2 in the Indian Ocean basin between 25.0°S and 30.2°S , decaying linearly to the north and south to zero at 22.2°S and 32.6°S (see Fig.3.1). This equatorward component does not contribute to the curl but is included to allow the possibility of Ekman upwelling at the eastern boundary. It is also consistent with annual mean winds to the west of both the Australian and South American continents. Unlike G-W, we also have a zonal component: the profile is shown in Fig.3.5 and is a sinusoidal fit to the annual mean winds portrayed in Godfrey (1989).

3.3. The Sequence of Runs

Four runs (listed in Table 3) were carried out: the first two are the basic experiment and the third and fourth are tests of the vertical mixing coefficients and the initial condition.

In the first two runs, the two basins are initially identical and the undisturbed temperatures and salinities are homogeneous at any given depth. The initial vertical stratification, to which the Pacific reservoir is restored throughout the integration, is chosen to be either a warm profile with a fresh surface layer (the Leeuwin run) or a cooler profile with temperatures and salinities more typical of the eastern equatorial Pacific (the Peru run). These conditions on temperature and salinity (illustrated in Fig.3.6) are identical to the Leeuwin and Peru runs of G-W and are based on real data from the equatorial regions in either ocean. This is the only difference between the first two runs in this study. The differences between our runs and those of G-W are i) the non-zero wind stress curl, ii) the greater number of levels in the vertical, iii) the larger Indian Ocean basin, which has been expanded westward and northward, iv) the positioning of the Indonesian gap, which has been moved southward from the dynamic equatorial waveguide to a more realistic latitude (8°S to 13°S) and v) the depth of the sill, which now prevents the communication of the deep waters in the two oceans.

TABLE 3				
The Sequence of Runs				
EXPERIMENT	Initial Condition in Indian Ocean	Restoring Condition in Pacific Ocean	A_{TV} (in cm^2/s)	A_{TV} (in cm^2/s)
Leeuwin	warm profile	warm profile	1.0	increasing with depth
Peru	cool profile	cool profile	1.0	increasing with depth
Leeuwin-2	cool profile	warm profile	20.0	1.0
Peru-2	cool profile	cool profile	20.0	1.0

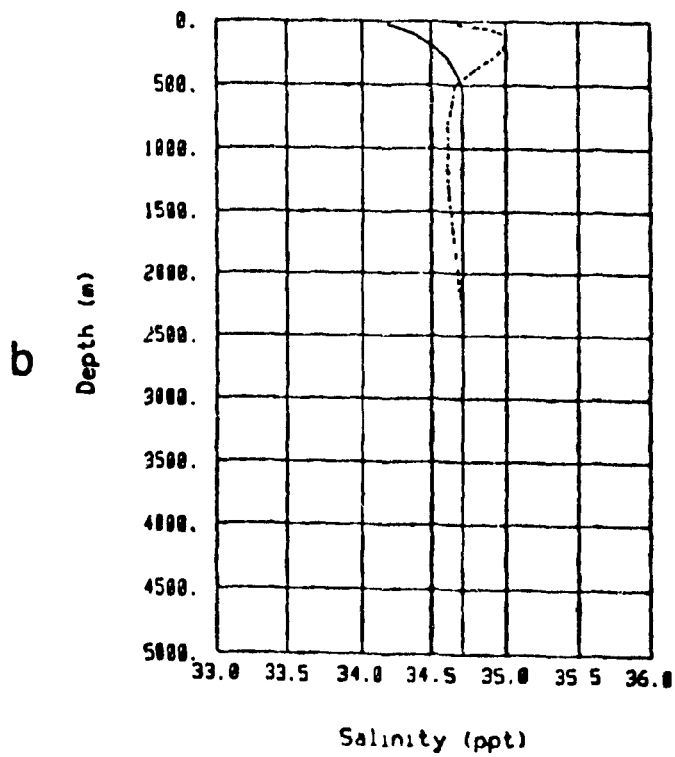
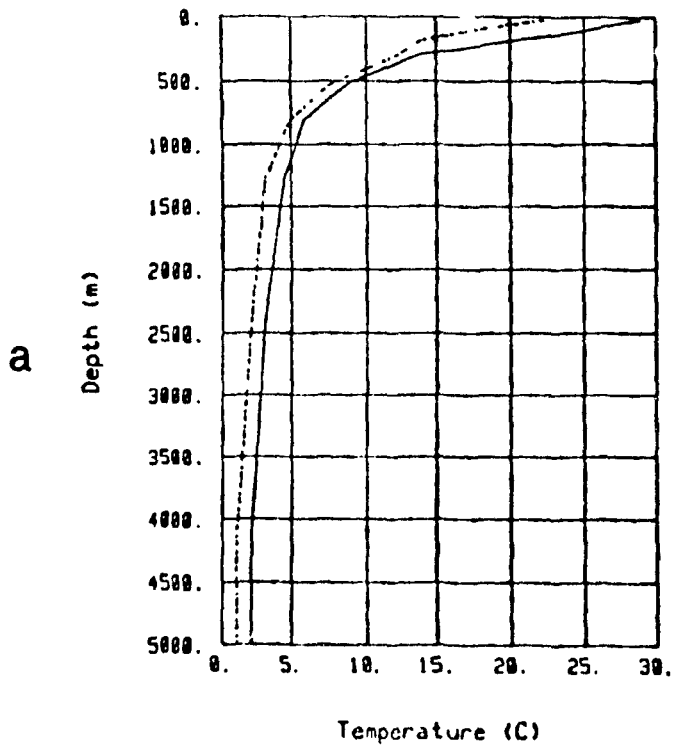


Fig 3.6. Vertical profiles of a) temperature in °C and b) salinity in ppt used as an initial condition in the Indian basin and a restoring condition in the Pacific basin. The solid line is for the Leeuwin run and the dashed line for the Peru run.

Both the Leeuwin and the Peru experiments were run for 3000 days with a timestep of 1600 seconds. The model evolves towards a quasi-equilibrium, where the total kinetic energy is still fluctuating quite strongly, but lacks an overall trend (Fig.3.7). The integration was subsequently pursued a further 200 days, to clarify the nature of the large-scale eddies especially prominent in the Peru run.

In the third and fourth runs, the vertical viscosity A_{TV} has been increased to $20 \text{ cm}^2/\text{s}$ and the vertical diffusivity has been changed to a uniform value ($A_{TV} = 1.0 \text{ cm}^2/\text{s}$). The Peru-2 run is otherwise identical to the first Peru run. The Leeuwin-2 run is initialised with the higher densities of the Peru Pacific but then forced with the warm fresh throughflow of the Leeuwin Pacific. The new runs were also integrated to 3000 days, but the Leeuwin-2 run was continued to 5000 days, to verify the equilibrium reached.

The results consist of the fields of u, v, w, T, S, ψ (streamfunction), surface heat flux, etc., for each individual run at 3000 days and for the differences (Leeuwin - Peru) between the first two runs and between the last two runs. The discussion in most of this thesis will concern only the first two runs. The motivation for the second set of runs and the comparison between the first and second sets will be given in the next-to-last section.

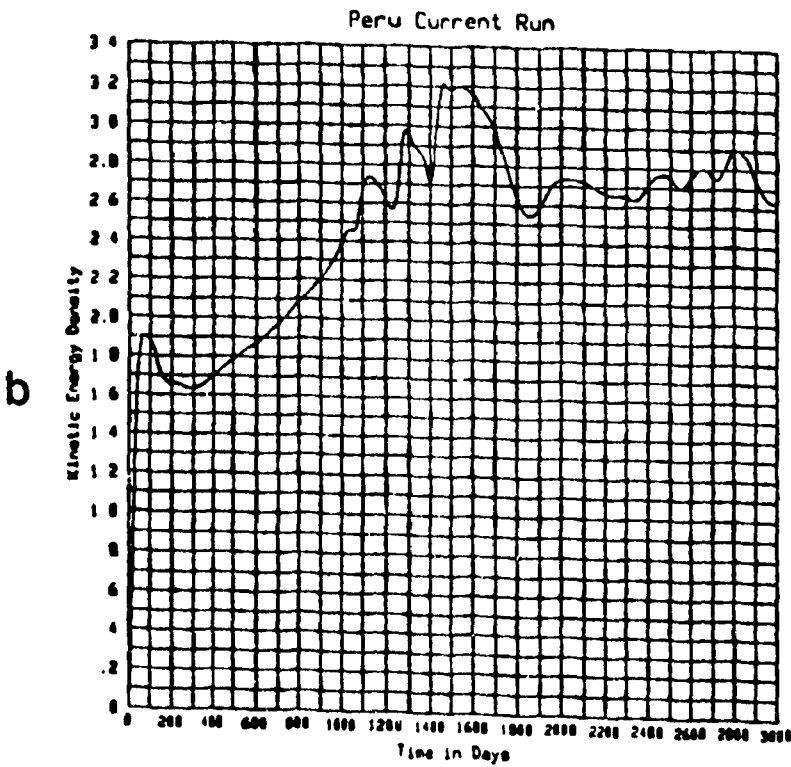
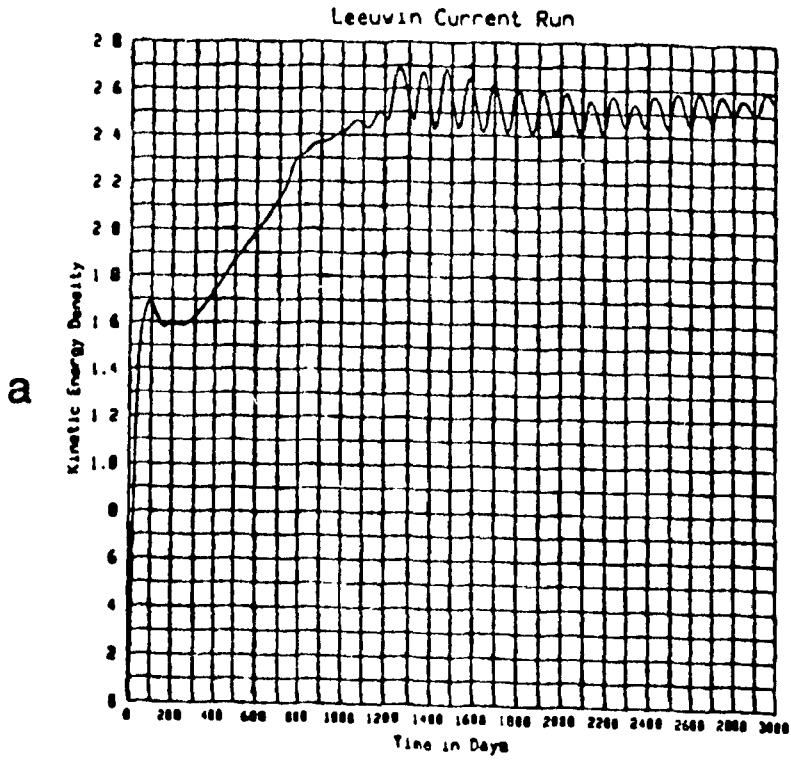


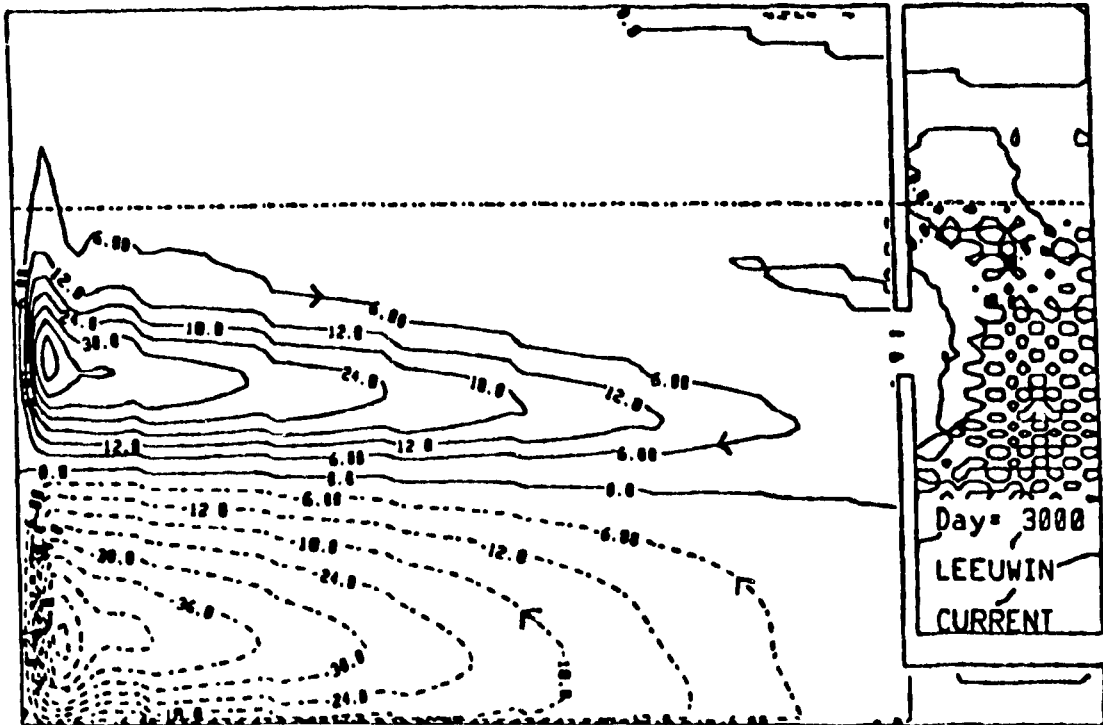
Fig 3.7. Kinetic energy density (in 10^{-1} kg/m s^2) as a function of time: a) Leeuwin run b) Peru run.

4. RESULTS

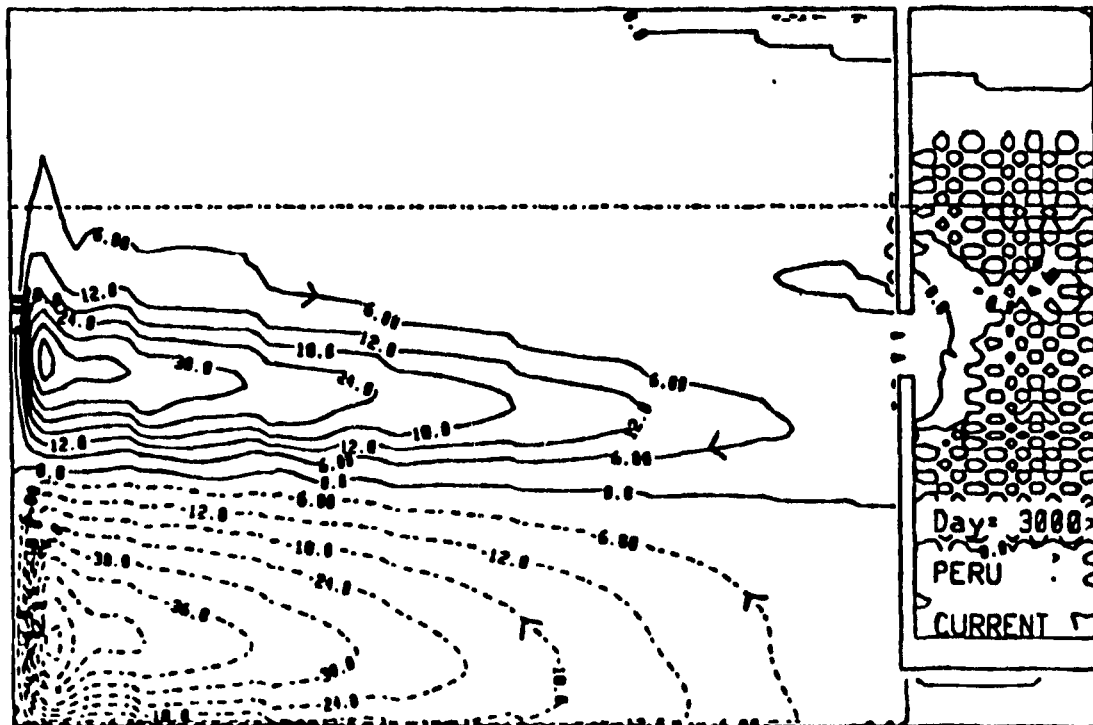
4.1. The Wind-Driven Circulation

In our simple, flat-bottomed ocean model, it is very helpful to be able to sort out the circulation into a wind-driven and a thermohaline component. Aside from small nonlinear effects, the barotropic streamfunction in a horizontal plane is a faithful reflection of that part of the circulation which is driven by the imposed winds, and which is therefore common to both the Peru and Leeuwin runs.

The barotropic streamfunction for the Leeuwin run is shown in Fig.4.1a; the corresponding plot for the Peru run (Fig.4.1b) is almost indistinguishable. The velocity vectors for the first two levels ($z=20\text{m}$ and $z=60\text{m}$) for both runs are plotted in Fig.4.2. The wind stress curl that we have chosen drives a system of two gyres with opposite rotations in the southern hemisphere. The clockwise (which we will hereafter refer to as cyclonic although it extends into the northern hemisphere) "tropical" gyre consists of a strong westward current a bit south of the Indonesian channel and an even stronger eastward return flow just to the north of the gap. At the western boundary the westward current splits into a very fast equatorward current and a slower poleward flow. Some of the equatorward jet actually crosses the equator but most of the mass is returned eastward by the second zonal jet completing the gyre. The poleward boundary current is fed along its course by westward flow from the interior up to about 5° - 10° from the southern border, then undergoes reflection in the southwest corner and travels eastward along the southern wall as part of the second "subtropical" gyre. The zero of wind stress curl falls along 20°S and this corresponds well to the separation between the two gyres in the depth-averaged context of the barotropic streamfunction, except near the eastern boundary, where the Indonesian throughflow pushes the zero transport line southward (through nonlinear effects and a small JEBAR contribution from the sill). The tropical gyre is more strongly surface intensified than the subtropical gyre so although the mass transport in the latter is higher, the



a



b

Fig.4.1. Barotropic (vertically-integrated) streamfunction (in Sv) for a) the Leeuwin run b) the Peru run.

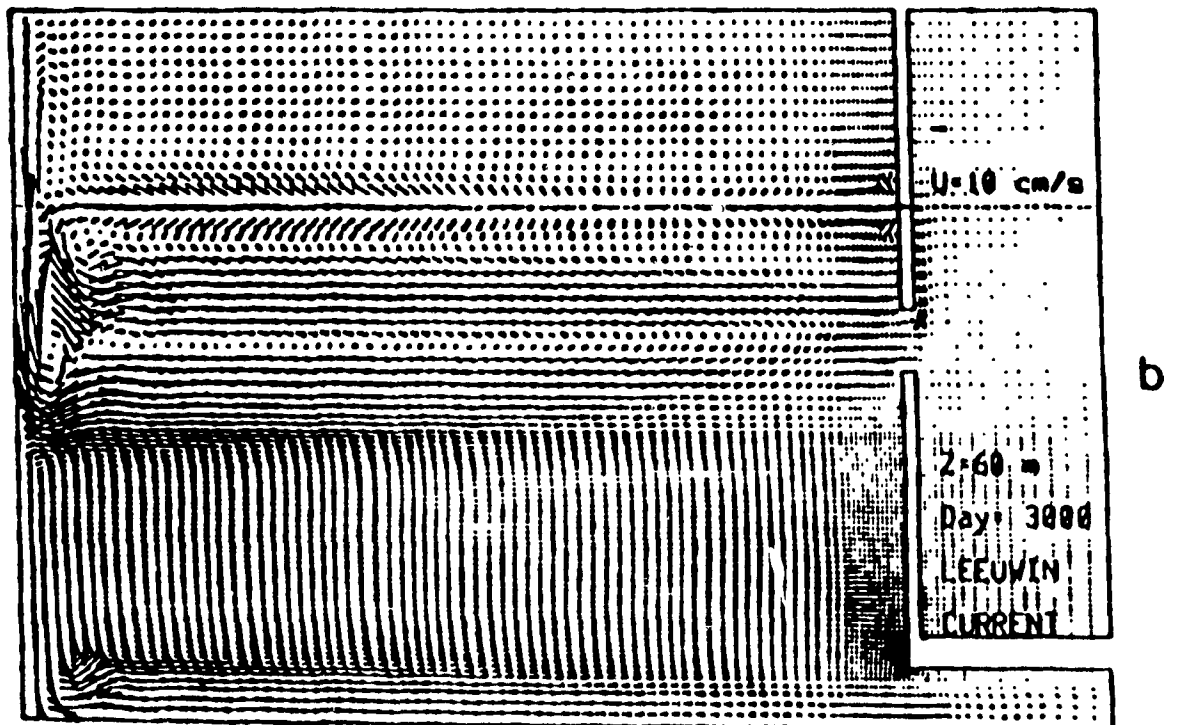
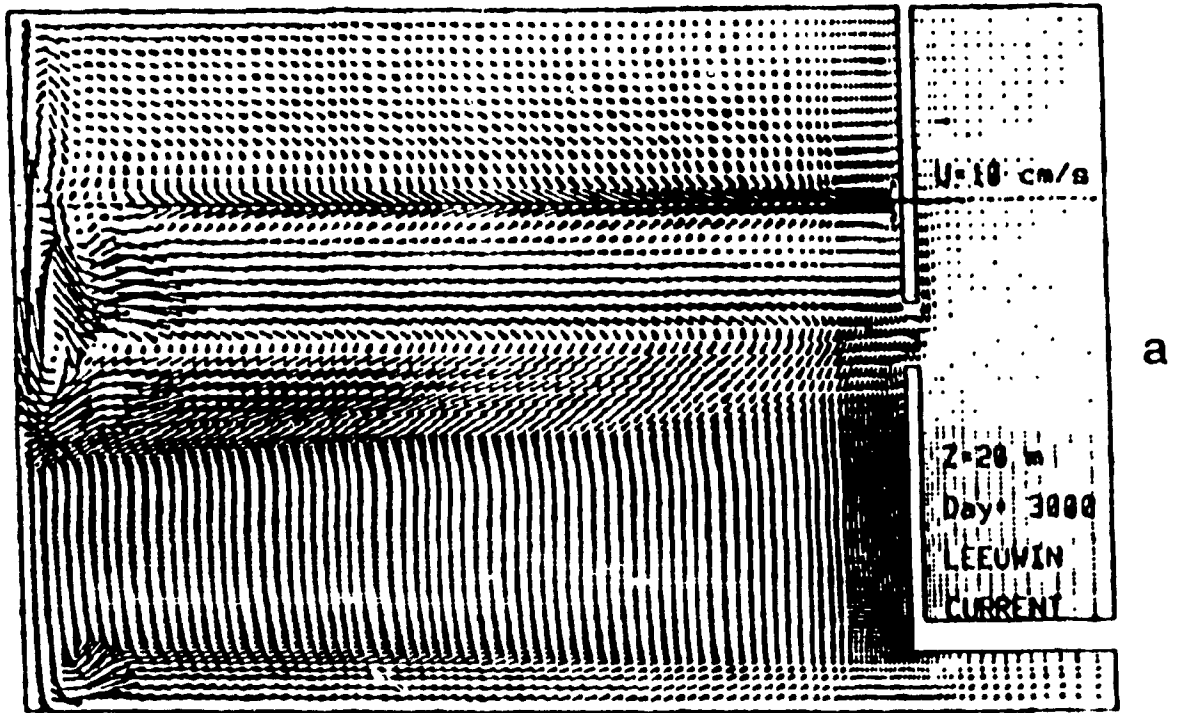
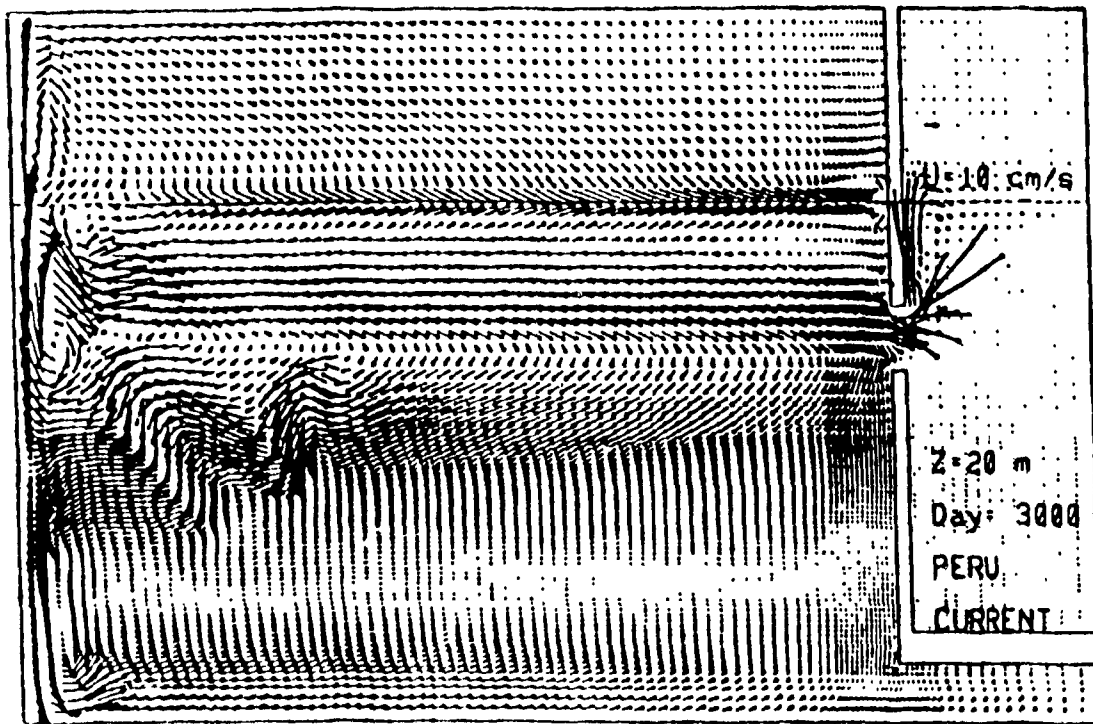
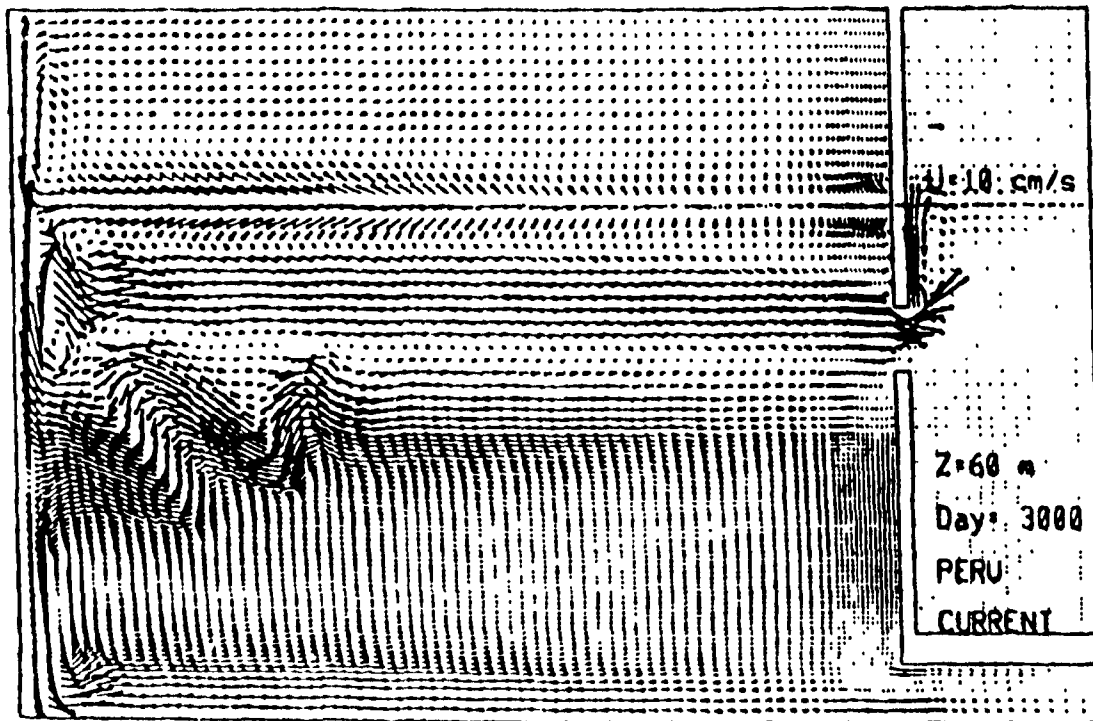


Fig.4 2 Horizontal velocities at $z=20\text{m}$ and $z=60\text{m}$ (levels 1 and 2). a) and b) Leeuwin run c) and d) Peru run. A scaling vector is given in the top right corner of this and all subsequent velocity vector figures. The vector tails are on gridpoints



c



d

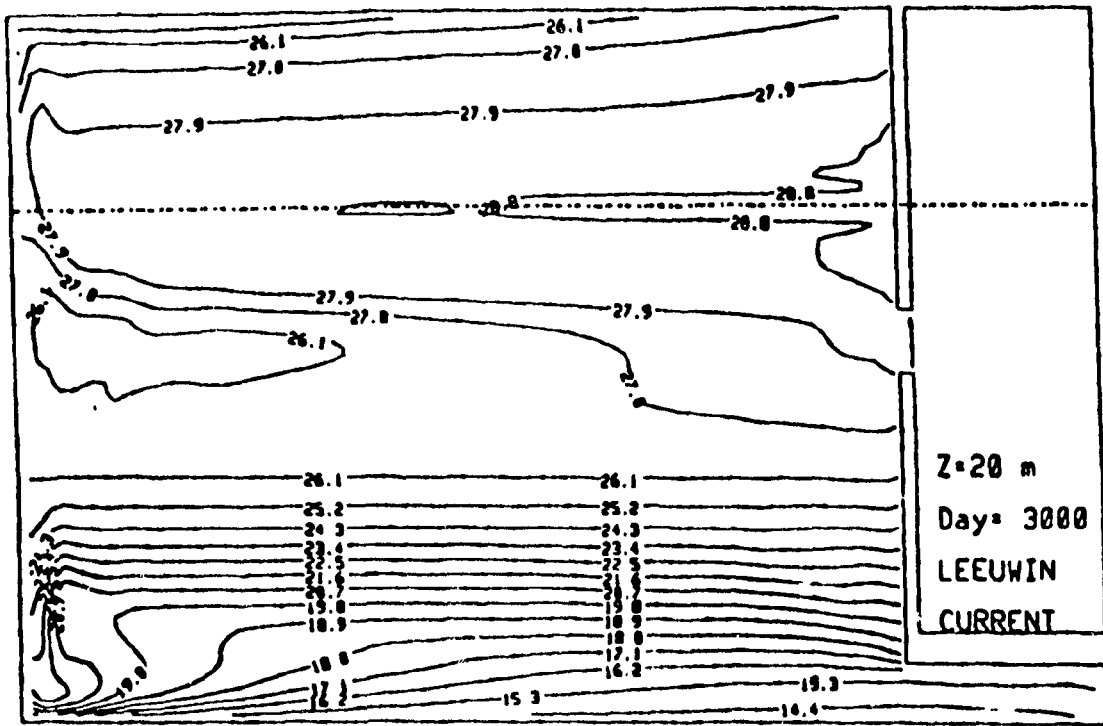
Fig.4.2. Cont. Horizontal velocities at $z=20\text{m}$ and $z=60\text{m}$ (levels 1 and 2): a) and b) Leeuwin run c) and d) Peru run.

surface currents (along the western boundary for example) are faster in the former. In the northern hemisphere, the magnitude of the wind stress curl is slight and fades to zero at the northern boundary. This explains the absence of streamfunction contours north of the equator.

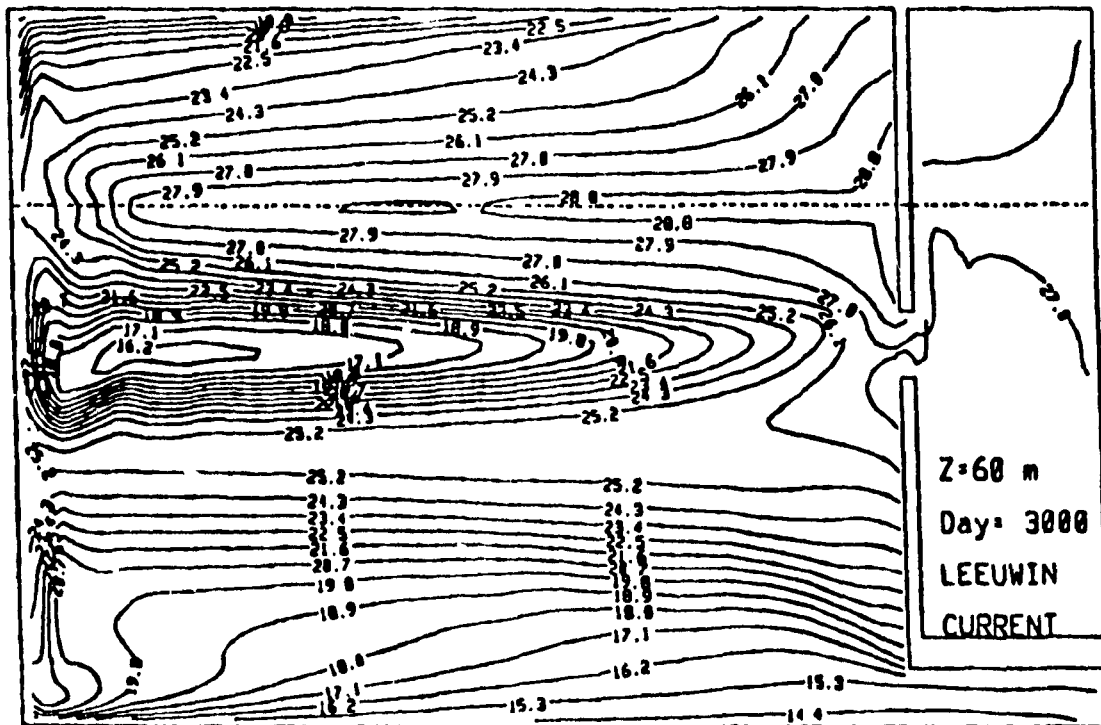
The Ekman rotation of the currents in the surface layer causes surface convergence and downwelling all along the equator where winds are westerly. The temperature contours at these two levels are drawn in Fig.4.3. The second level is at nearly the same temperature as the surface all along the equator. The convergence at 32.5°S and the divergence at 7.5°S where the zonal component of the wind changes sign are barely noticeable in the velocity vectors of either run, but in the overturning streamfunction we see shallow Ekman-driven cells in the surface layers (Fig.4.4). The Ekman theory does not hold right on the equator where the Coriolis parameter vanishes. There, the surface currents are not rotated and the westerly wind pushes warm surface water all the way across the basin to Indonesia and forces downwelling through continuity at the boundary.

The southerly wind stress between 32.6°S and 22.2°S should, in the southern hemisphere, drive fluid away from an eastern boundary, allowing deeper water to upwell at the coast, and we do indeed observe this in vertical velocity plots for the Peru run (Fig.4.5). The situation is opposite for the Leeuwin run where we find downwelling in a small patch at the southern tip of Australia, just beyond the influence of the longshore wind. At the second interface ($z=80\text{m}$), the wind can no longer act directly and the patch of negative vertical velocity has spread northward along the coast. This is a good test of our simulation of the Leeuwin Current, since the absence of upwelling is one of the essential characteristics of the real current. The analytic models of Thompson (1987) and Weaver and Middleton (1990) demonstrate how if the mixed layer is deep enough a longshore pressure gradient can overcome an upwelling-favourable wind, and produce downwelling strengthening downward from the surface to the base of the thermocline.

The model also produces spurious upwelling along the western boundary. Toggweiler et al. (1989) suggest that the unphysical partitioning of mixing processes into horizontal and vertical components rather than components parallel and perpendicular to surfaces of constant density may

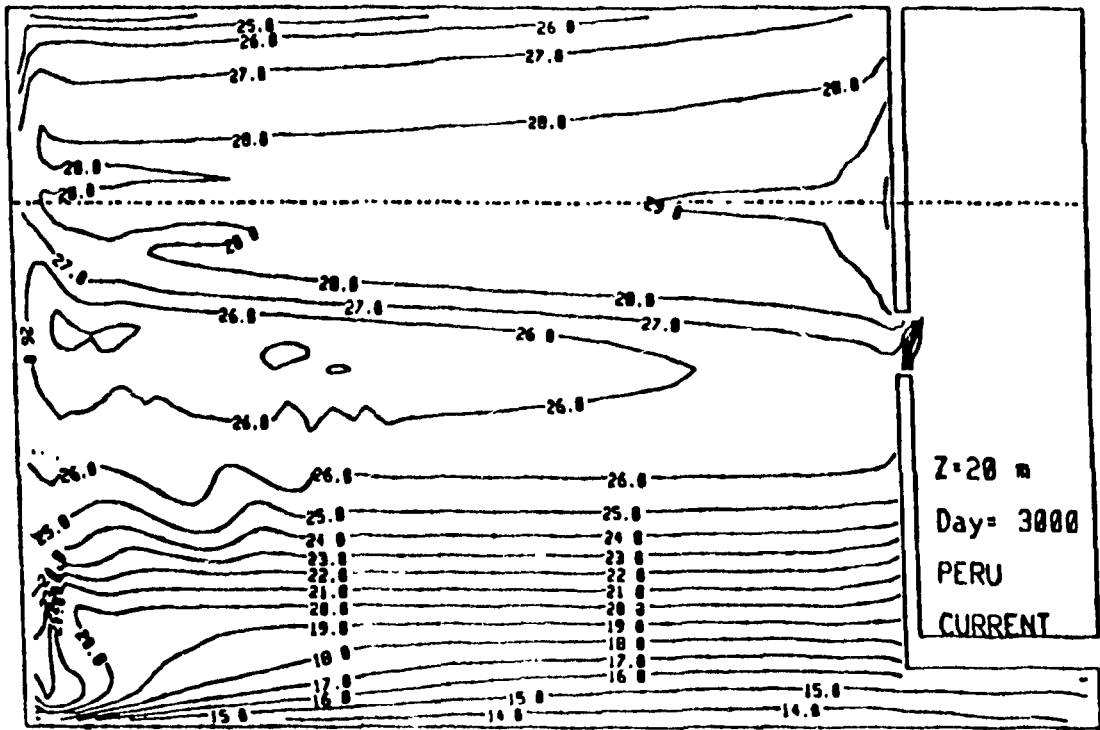


a

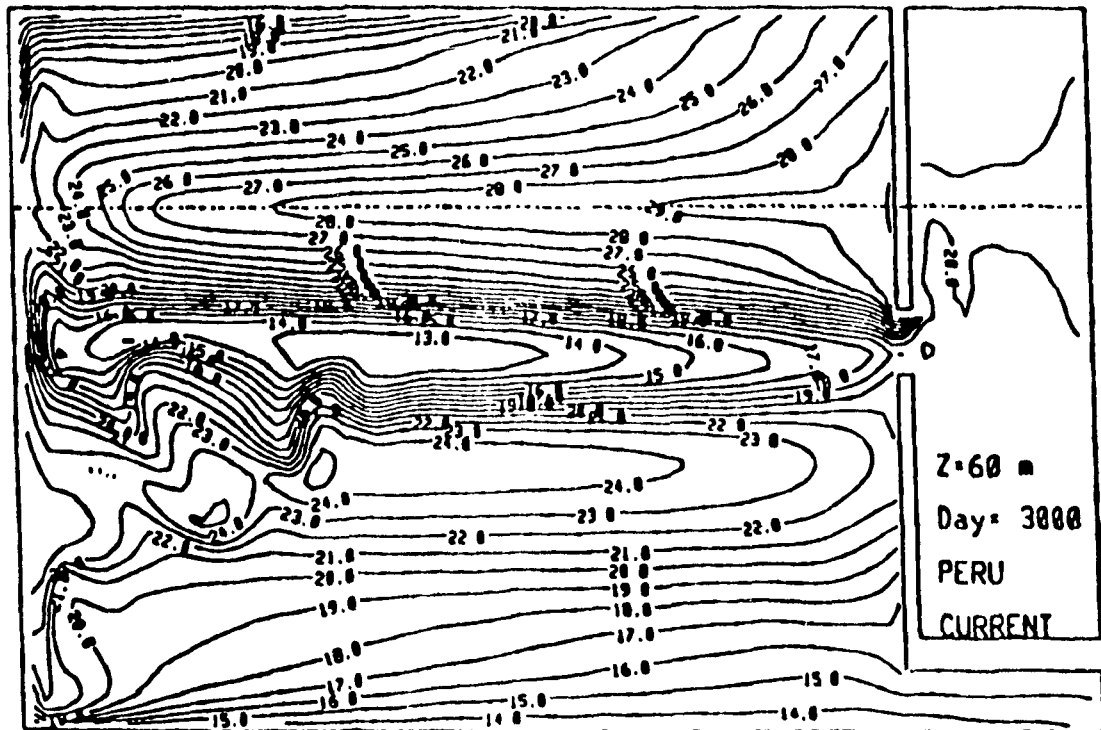


b

Fig.4.3. Temperatures in °C at z=20m and z=60m (levels 1 and 2): a) and b) Leeuwin run c) and d) Peru run.



c



d

Fig.4.3. Cont. Temperatures in °C at z=20m and z=60m (levels 1 and 2): a) and b) Leeuwin run c) and d) Peru run.

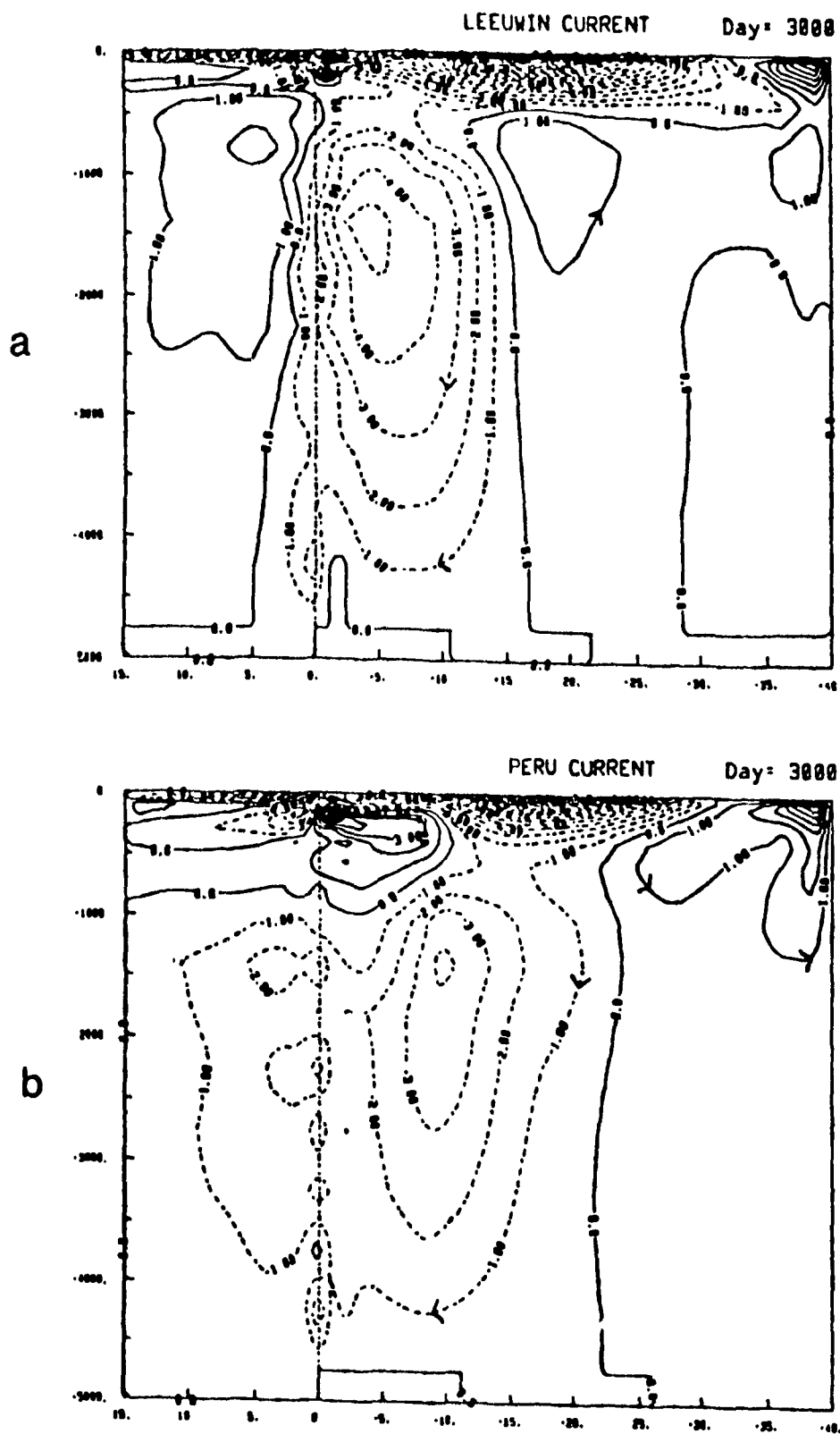
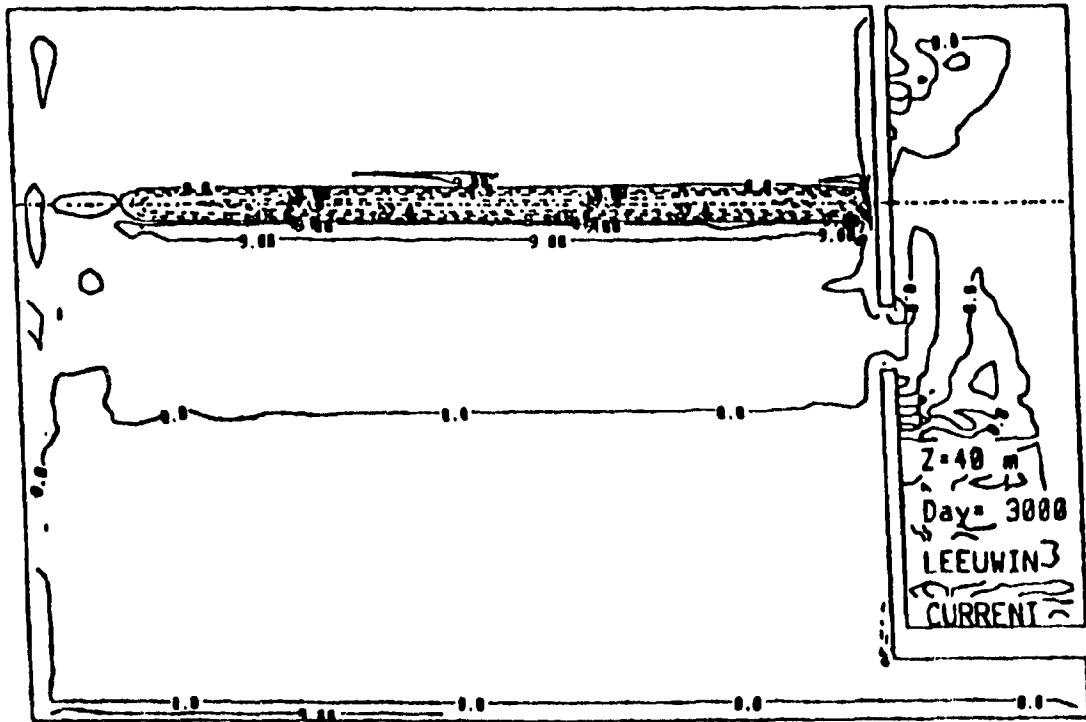
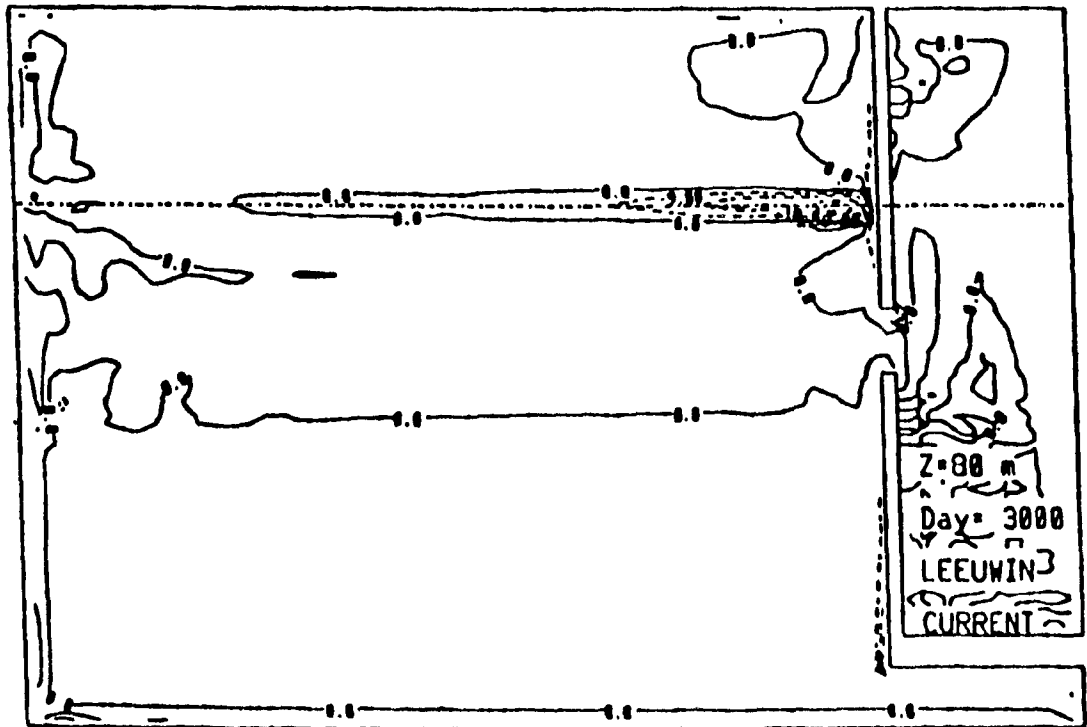


Fig.4.4. Overturning (zonally-integrated) streamfunction (in Sv) as a function of latitude for a) the Leeuwin run b) the Peru run.



a



b

Fig.4.5. Vertical velocities in 10^{-4} cm/s at $z=40\text{m}$ and $z=80\text{m}$ (1st and 2nd inter-faces): a) and b) Leeuwin run c) and d) Peru run. Solid contours indicate upwelling and dashed contours downwelling.

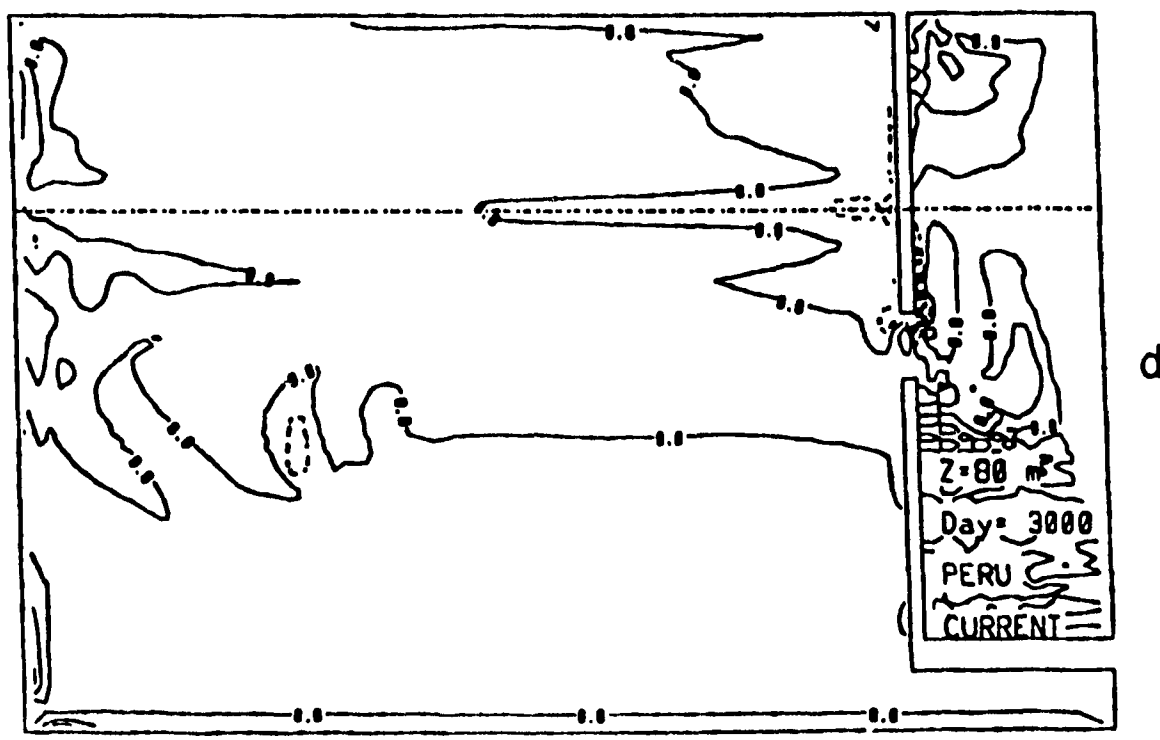
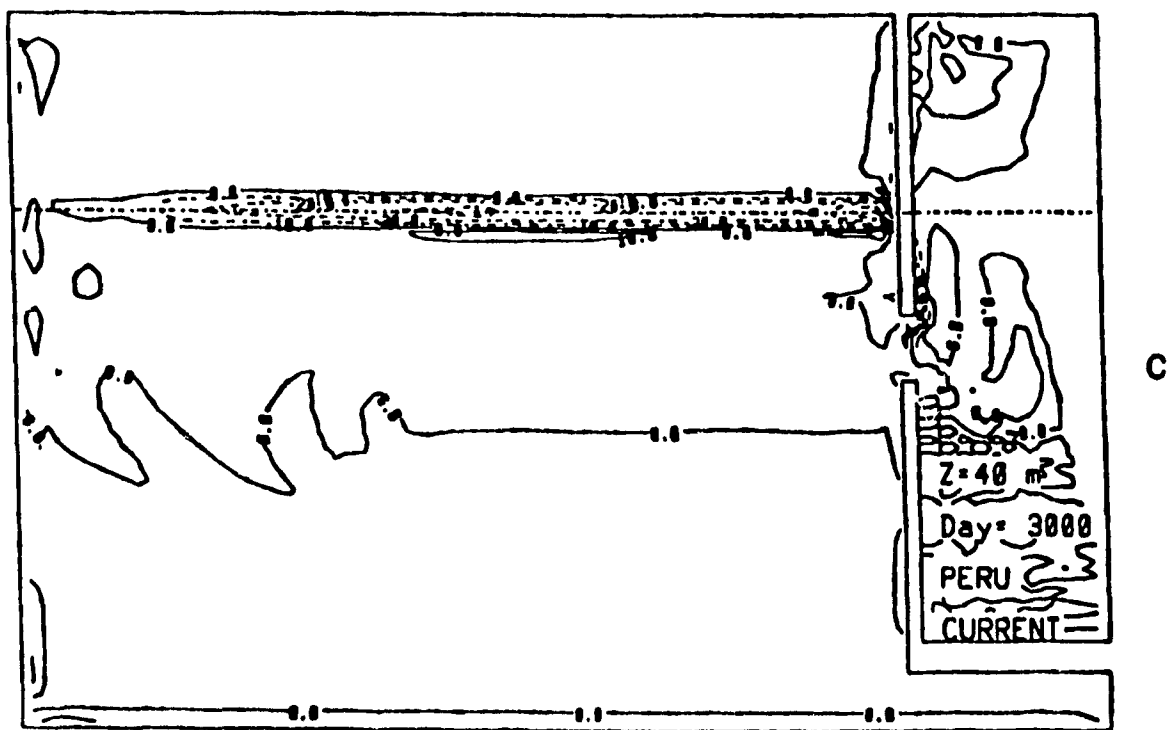


Fig.4.5. Cont. Vertical velocities in 10^{-4} cm/s at $z=40$ m and $z=80$ m (1st and 2nd interfaces): a) and b) Leeuwin run c) and d) Peru run. Solid contours indicate upwelling and dashed downwelling.

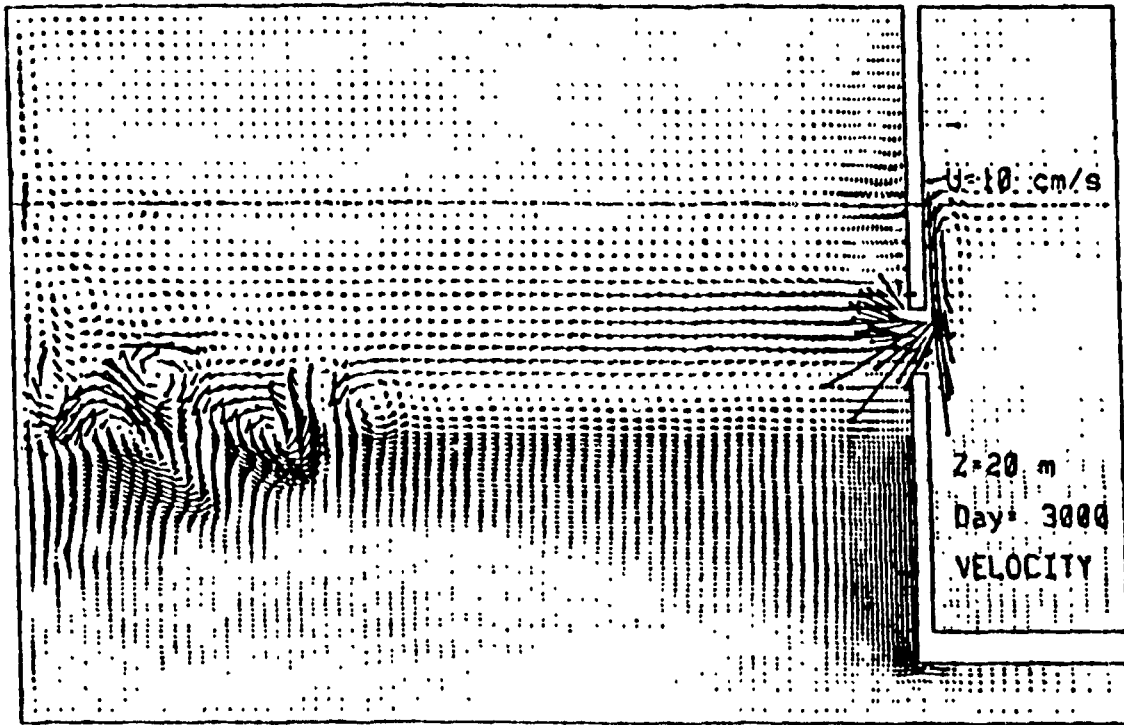
be a cause. Strong cross-shore gradients of density associated with the fast boundary currents are flattened by the lateral mixing scheme and the artificial transport of heat across the width of the current must be compensated for by upwelling along the inshore edge. The upwelling along the southern boundary is however more likely due to the northward Sverdrup transport carrying fluid away from the boundary.

Away from the boundaries, the Ekman convergence and divergence in the wind-driven gyres divide the ocean into areas of upwelling and downwelling (Fig 4.5). In the upper layers, the distribution of vertical velocity has weak upwelling between the equator and about 16°S (and everywhere in the northern hemisphere), and weak downwelling between 16°S and the southern boundary. At greater depths, the pattern is complicated by alternating pools of upwelling and downwelling along the equator; this effect will be discussed briefly in Chapter 5. But in the Peru run, the vertical velocity plots are dominated by the dynamics of the barotropic eddies generated near the western boundary (in Fig.4.2 these are more accurately described as meanders but from other figures it is clear that they are in fact complete eddies). This region of intense eddy circulation occupies a large area (from 10°S to 25°S and 44°E to about 84°E) and can be identified in every model field (e.g. temperature, salinity, streamfunction). Similar eddies occur in the Leeuwin run also, but they are not nearly as developed as in the Peru run (however, there is evidence that they are still growing). The velocity vectors in the difference plot reveal other much weaker eddies to the north of the major ones (Fig 4.6). The cause of the eddies is thought to be barotropic instability of the westward current: we shall present some evidence in support of this further on.

4.2. The Thermohaline Component

4.2.1. Consequences of the Haney Surface Boundary Condition

The Haney flux condition at the upper boundary interferes with the wind-driven circulation in the



a



b

Fig.4.6. Velocity difference (Leeuwin - Peru) at a) $z=20\text{m}$ and b) $z=275\text{m}$ (levels 1 and 5).

same ways in both the Leeuwin and Peru runs. The impact of the temperature forcing is seen by the zonal orientation of the isotherms at the first model level (see Fig.4.3), except where there is distortion by the fast western boundary currents, which can advect water meridionally on timescales shorter than the restoring condition.

The thermal forcing at the surface is partly responsible for the eastward flow in the northern hemisphere. In both runs, the difference in heating from the equator to 15°N causes quasi-zonal isotherms and drives eastward flow along them in the upper layers. The rise in steric height¹ along the northern boundary (Fig.4.7) also suggests a northward component, despite the small southward transport required by the negative wind stress curl. At deeper levels, the steric height gradient flattens out and even reverses (at $z=275\text{m}$), consistent with the thermohaline circulation as an internal mode. In the southern hemisphere, the surface temperature distribution again imitates the Haney apparent atmosphere, although in the equatorial region the wind-forced gyre is noticeable even at the first model level.

The Haney condition is not imposed in the Pacific reservoir. This discontinuity has an enormous effect on the dynamics of the Peru run, where the temperature to which the first layer of the Pacific is restored is more than 5°C cooler than the Haney temperature at the latitude of the Indonesian passage. A strong front appears at the opening and water cascades down the slope into the Pacific (see Fig.4.2). A steep meridional steric height drop is set up at the gap (Fig 4.8c). The fastest inflow happens at the northern limit of the channel because the temperature jump is greatest there and because the wind-driven gyre circulation has an eastward component there. In the Leeuwin run, the surface temperature of the Pacific Ocean is 29°C, only about 1°C warmer than the Haney temperature at the latitude of the opening. The throughflow is much weaker and almost southerly. In each case, a western boundary current (southward in the Leeuwin run and northward

¹ The steric height at a given depth is defined as the integral with respect to pressure of the specific volume anomaly δ between a reference depth and the chosen depth, where δ is the difference between the specific volume ($1/\text{density}$) at the measured p , S and T and the specific volume at the same pressure but a reference salinity and temperature of 35.00 ppt and 0°C (Gill, 1982).

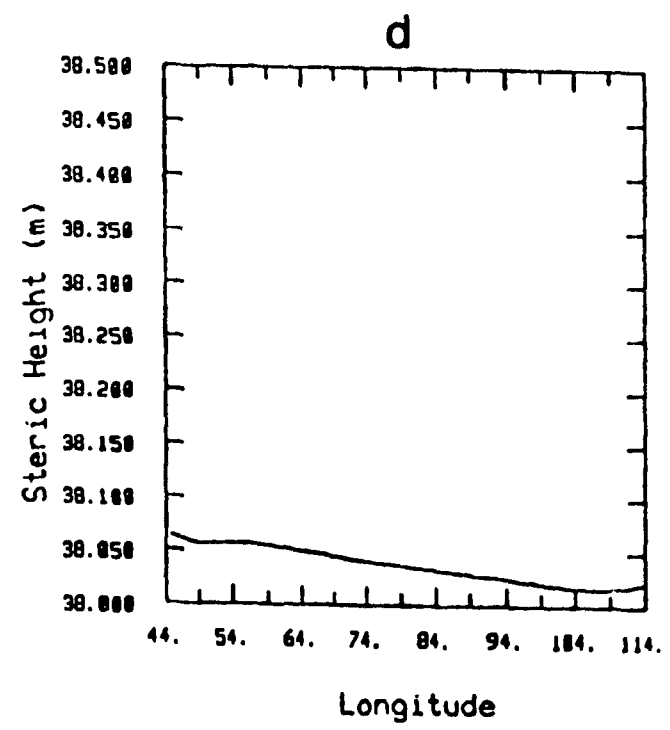
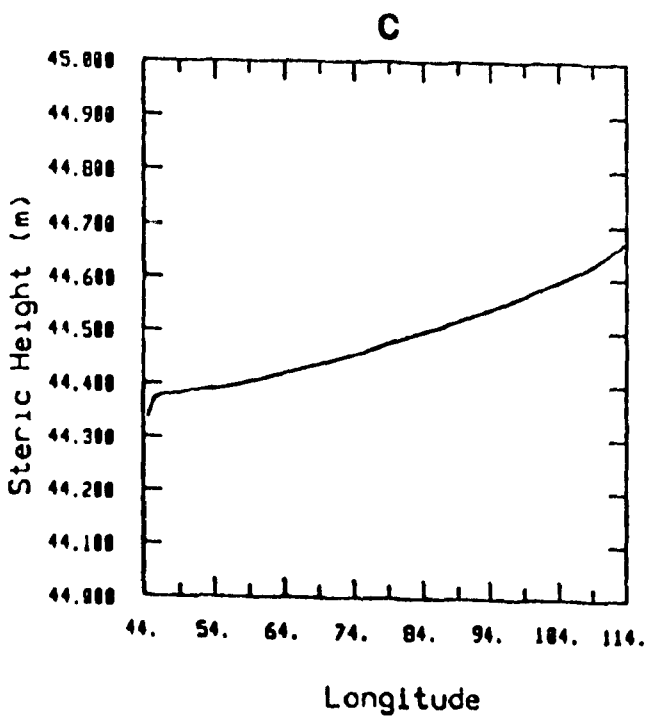
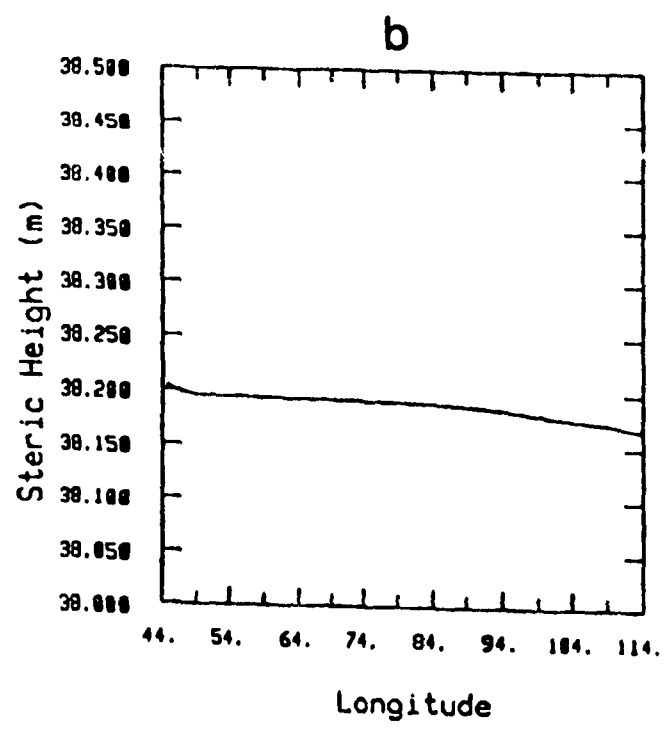
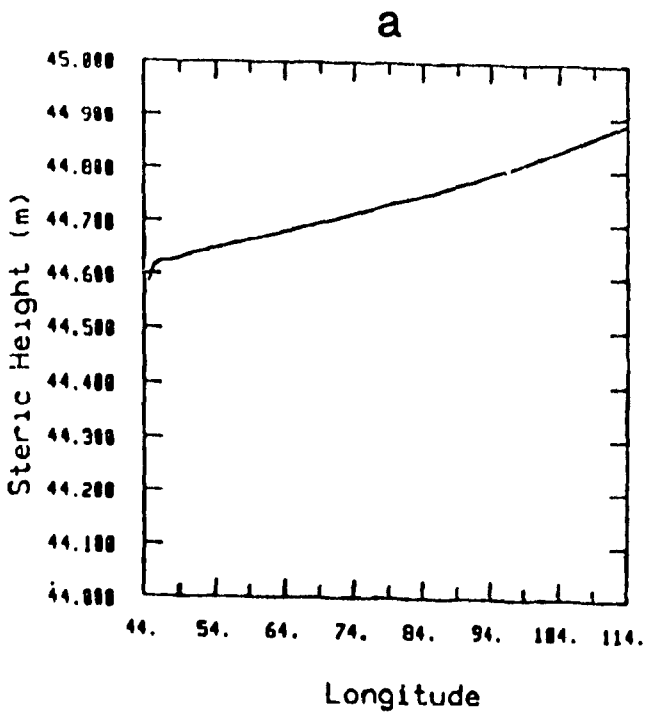


Fig.4.7. Steric height in m along the northern boundary (with respect to a reference depth of 1600m) at $z=20\text{m}$ and $z=275\text{m}$ (levels 1 and 5): a) and b) Leeuwin run c) and d) Peru run.

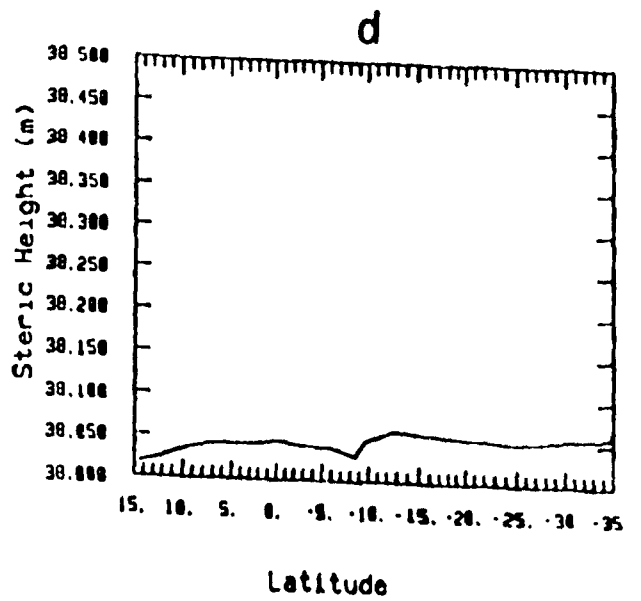
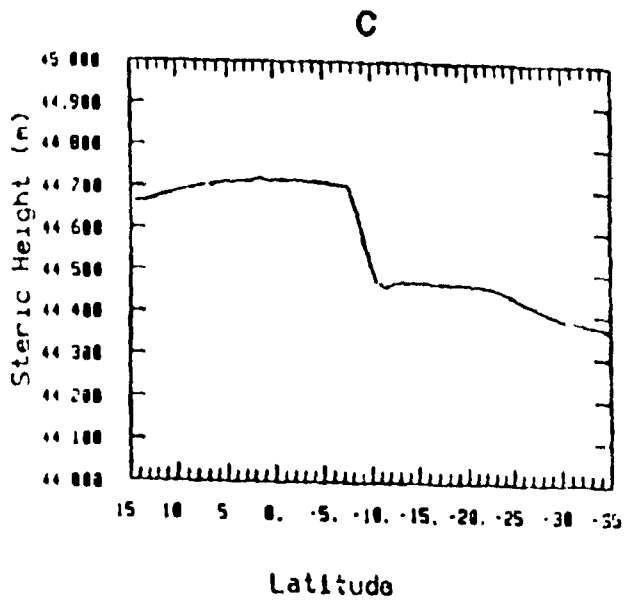
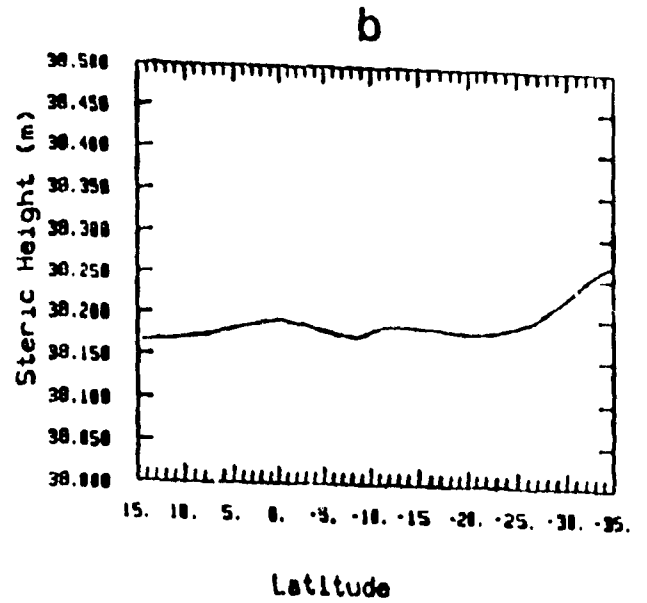
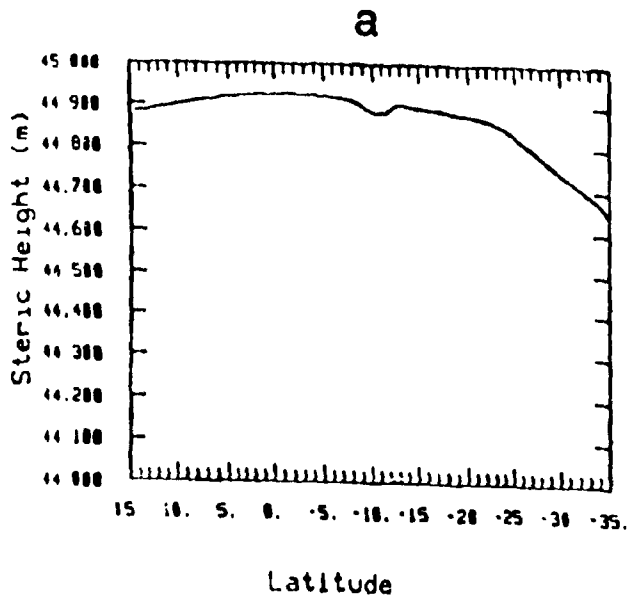


Fig.4.8. Steric height in m along the eastern boundary (with respect to a reference depth of 1600m) at $z=20\text{m}$ and $z=275\text{m}$ (levels 1 and 5): a) and b) Leeuwin run c) and d) Peru run.

in the Peru run) appears on the Pacific side of the Indonesian barrier.

4.2.2. The Eastern Boundary Regimes

Even in the presence of the annually-averaged Sverdrup circulation, the eastern boundary regimes of the two runs are opposite in every way. By reproducing the 'Leeuwin' and 'Peru' Currents of G-W in our more complete model, we are validating their hypothesis that the buoyancy forcing is a sufficient cause for the anomalous Leeuwin Current, and justifying their omission of the Sverdrup forcing which has its weakest effect at the eastern boundary anyway.

The eastern boundary current in the Leeuwin run is driven in the same way here as in G-W. The plot of steric height along the eastern boundary at $z=20\text{m}$ (Fig.4.8) shows the much larger meridional gradient (a drop of 25 cm between 13°S and 35°S) produced by the throughflow of warm fresh water to the north. In the Peru run, the steric height is significantly flatter except for the abrupt drop caused by the fast throughflow into the Pacific. The velocity vectors for the Leeuwin run at $z=60\text{m}$ (below the effective Ekman layer) show a substantial onshore flow halfway down the Australian continent (Fig.4.9). At the coast, the flow divides and most of the mass heads southeast. North of the divide, the boundary current is equatorward but very weak, and there is downwelling at most latitudes along the coast and especially at the southern tip of Australia. In the Peru run, the onshore flow is absent and the current is northward at all latitudes along the coast till it meets the westward zonal current into the interior (the model equivalent of the South Equatorial Current). The temperature contours at the same depth (in Fig.4.3) show the warm coastal climate of the Leeuwin run and the cool temperatures related to Ekman upwelling in the Peru run. At the surface, the temperature gradient along the Leeuwin coast seems smaller than in the Peru run (Fig.4.10 is a meridional-vertical section of temperature along 113.2°E), however below the surface sponge layer for the heat fluxes, the isotherms of the Peru run are nearly horizontal, while in the Leeuwin run, the mixed layer clearly deepens poleward, causing the meridional temperature gradient. Just as in G-W, this occurs because of increasingly vigorous

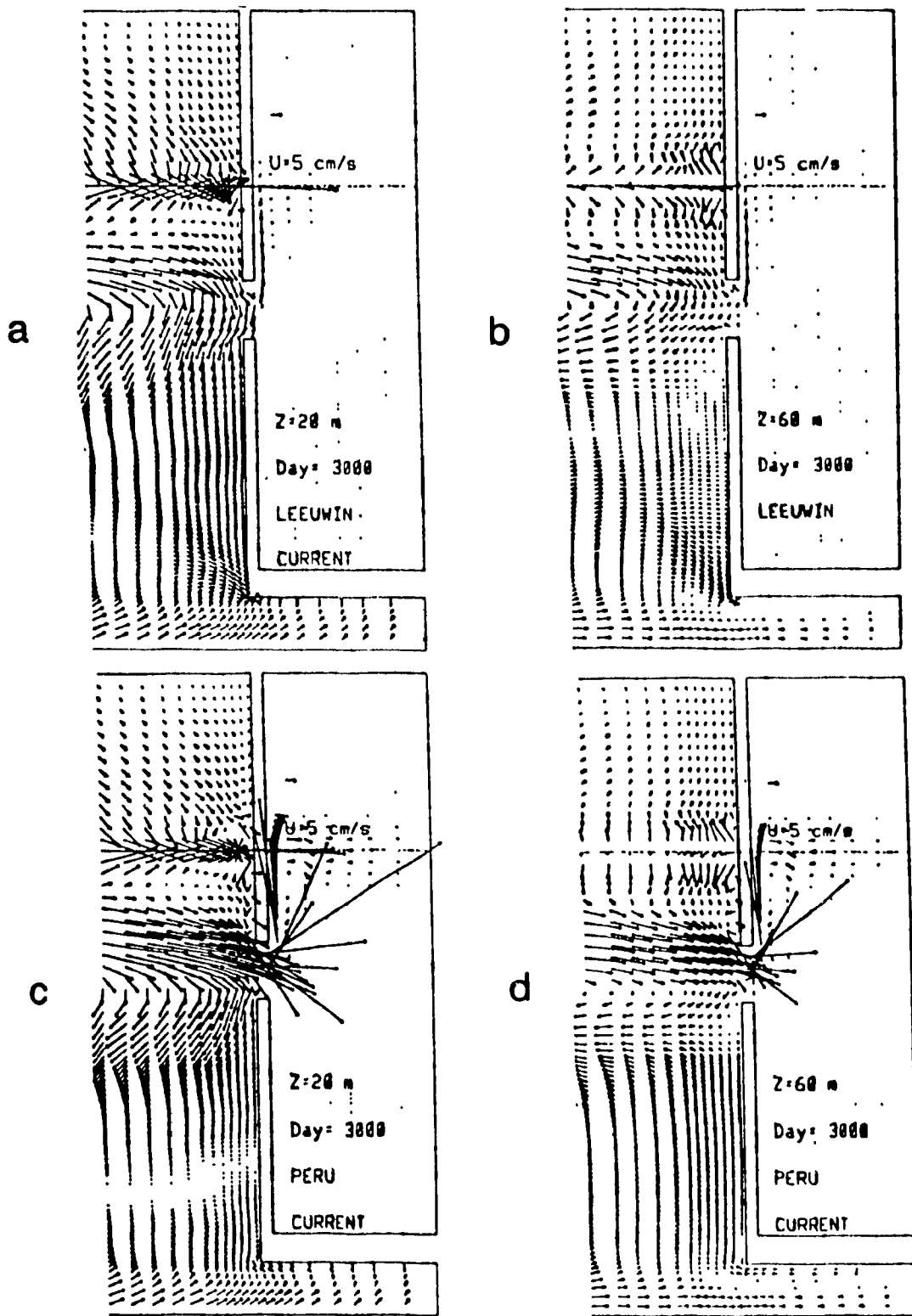


Fig.4.9. Velocity vectors at every 2nd gridpoint near the eastern boundary at $z=20\text{ m}$ and $z=60\text{ m}$ (levels 1 and 2) a) and b) Leeuwin run c) and d) Peru run.

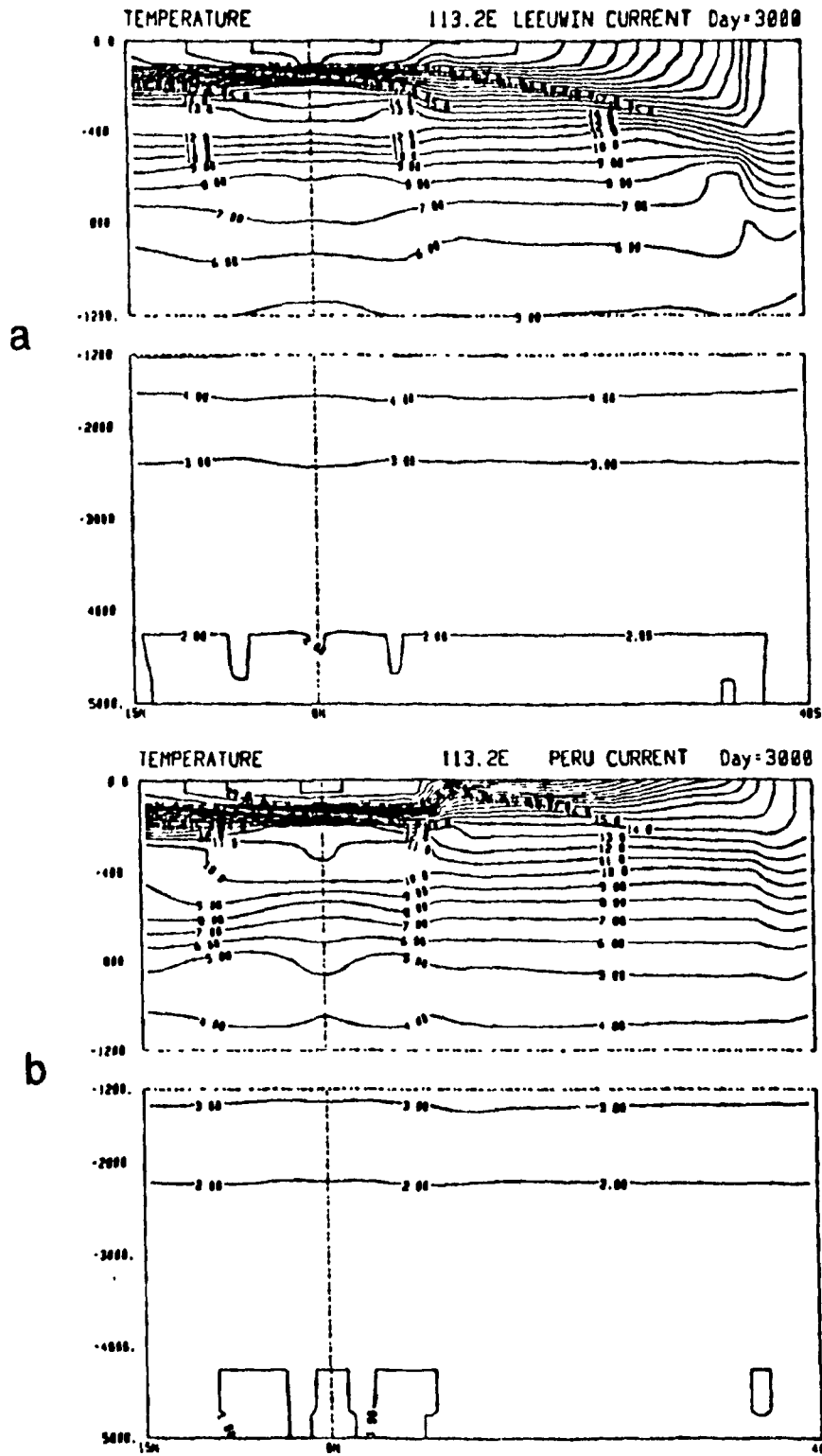


Fig.4.10. Meridional-vertical section of temperature (in °C) along 113.2°E (two gridpoints from the eastern boundary): a) Leeuwin run b) Peru run.

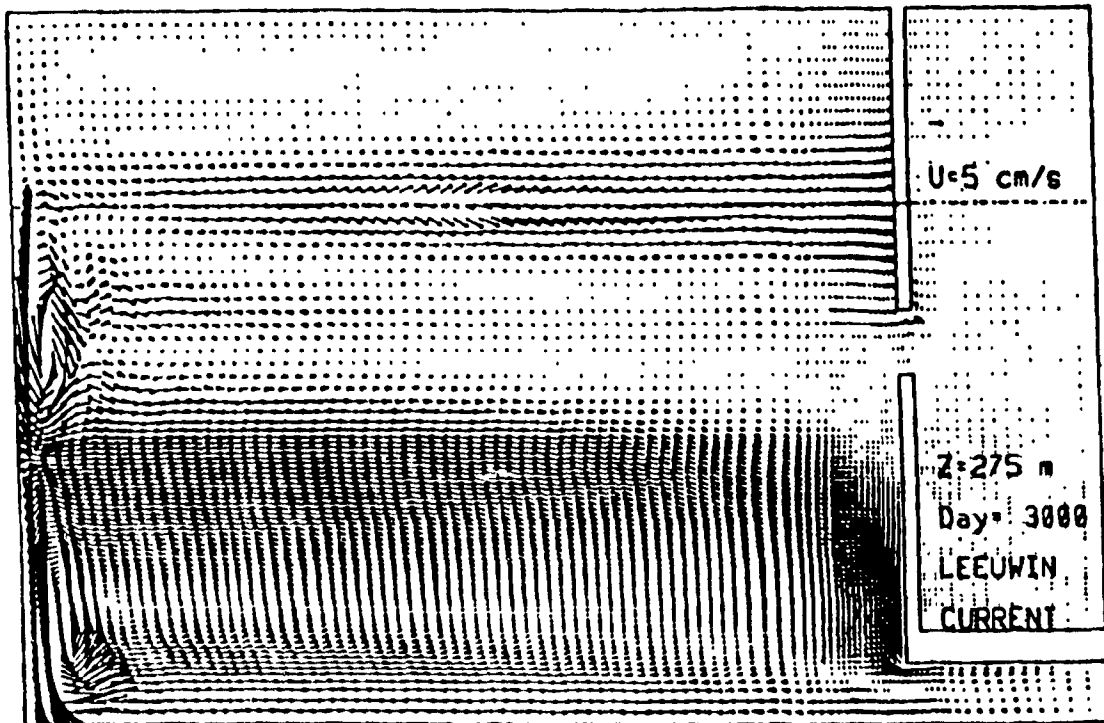
convective overturning as the surface releases heat to the increasingly cooler atmosphere.

The Leeuwin Current in this model is unrealistically weak. G-W have suggested a number of reasons for this which will be listed in Section 5.1 and we pause here only to note that they estimated that perhaps as much as 30% of the observed 50 cm drop in steric sea level (steric height at the surface) along western Australia could be attributed to the salinity effects which are lacking in our model. (For consistency with the other figures, we have presented the steric height at $z=20\text{m}$ rather than at the surface.)

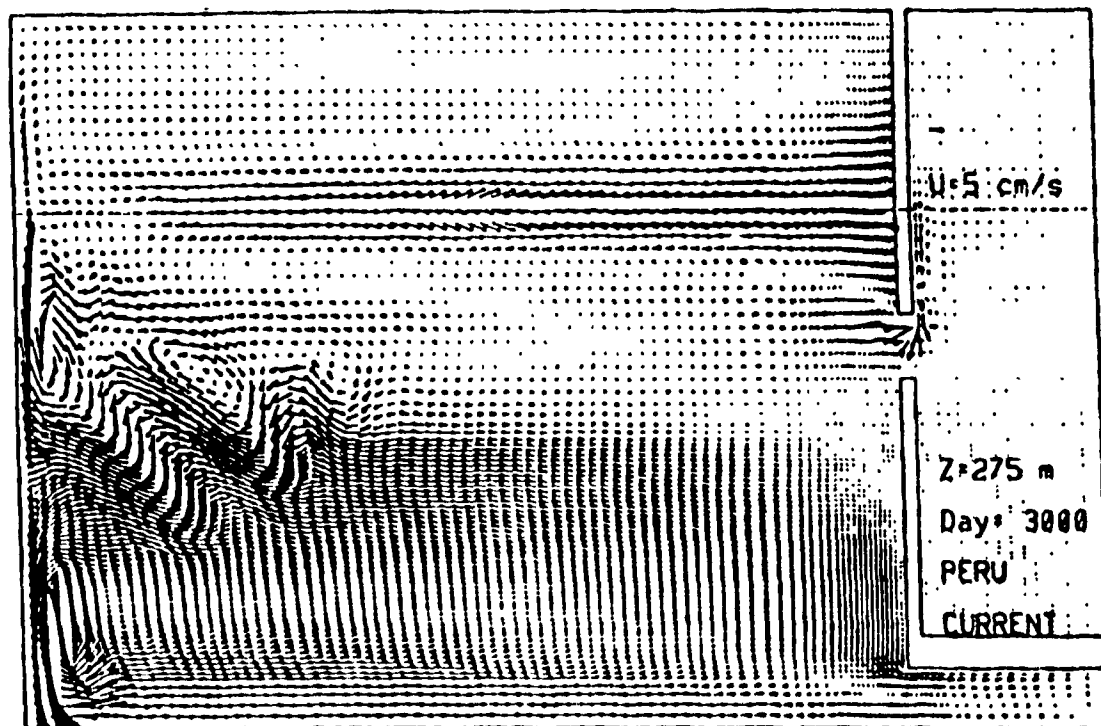
The difference in the eastern boundary regimes is felt all the way into the Great Australian Bight. In the Peru run, a westward current appears along the southern coast of Australia (Fig 4 9), feeding into the eastern boundary current, but this is partly just a consequence of the dead end reflecting the flow headed into the Pacific. If the barrier south of Australia were removed, we would see the eastern boundary current in the Leeuwin run rounding the corner into the bay, in closer accord with observations.

The reversal at depth of the density gradients that is expected in the buoyancy-driven coastal circulation of the Leeuwin run takes place at $z=275\text{m}$. By $z=180\text{m}$, the steric height along the eastern boundary is nearly flat, and by $z=275\text{m}$, a steep poleward rise is present (Fig 4 8). In the Peru run, the steric height slope is negligible at both these depths and the large drop caused by the surface flow into the Pacific has disappeared. The velocity vectors for the Leeuwin run at $z=275\text{m}$ (Fig.4.11) show the offshore flow required to geostrophically balance the reversed density gradient. The equatorward Leeuwin Undercurrent along the coast enhances the anticyclonic wind-driven gyre at this latitude (Fig 4.12). At this depth, the meridional temperature gradient is opposite in direction to the surface gradient and the undercurrent is advecting warmer temperatures northward (Fig 4 13). The temperature gradient has reversed in the Peru run also.

4.2.3. The Basinwide Circulation



a



b

Fig.4.11. Horizontal velocities at z=275m (level 5) a) Leeuwin run b) Peru run

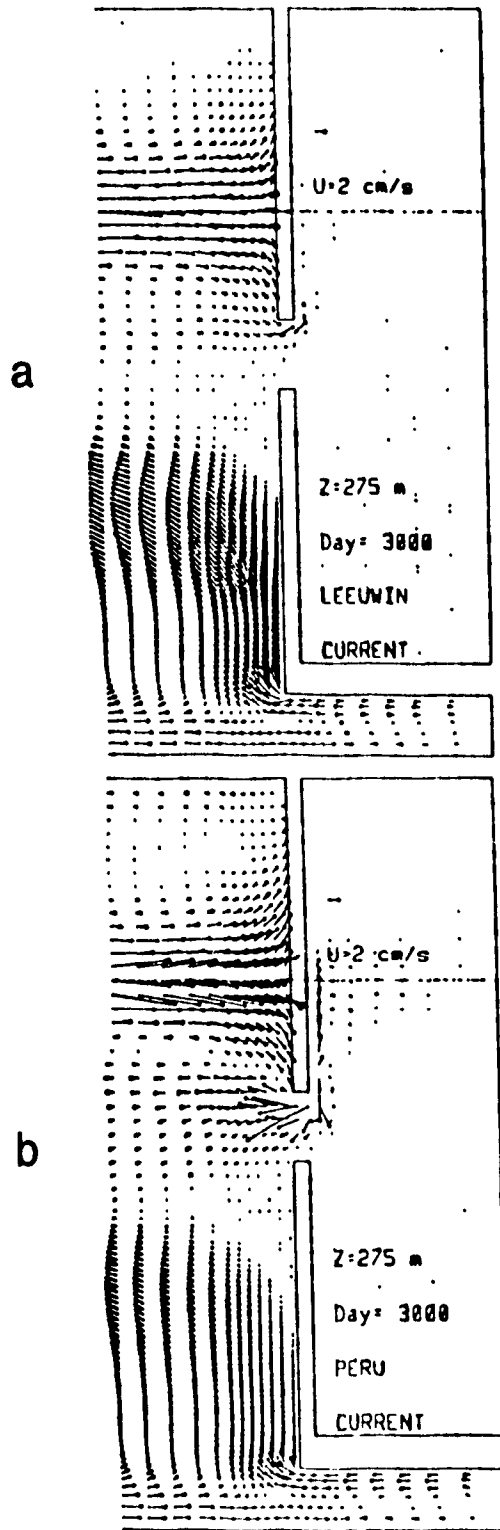
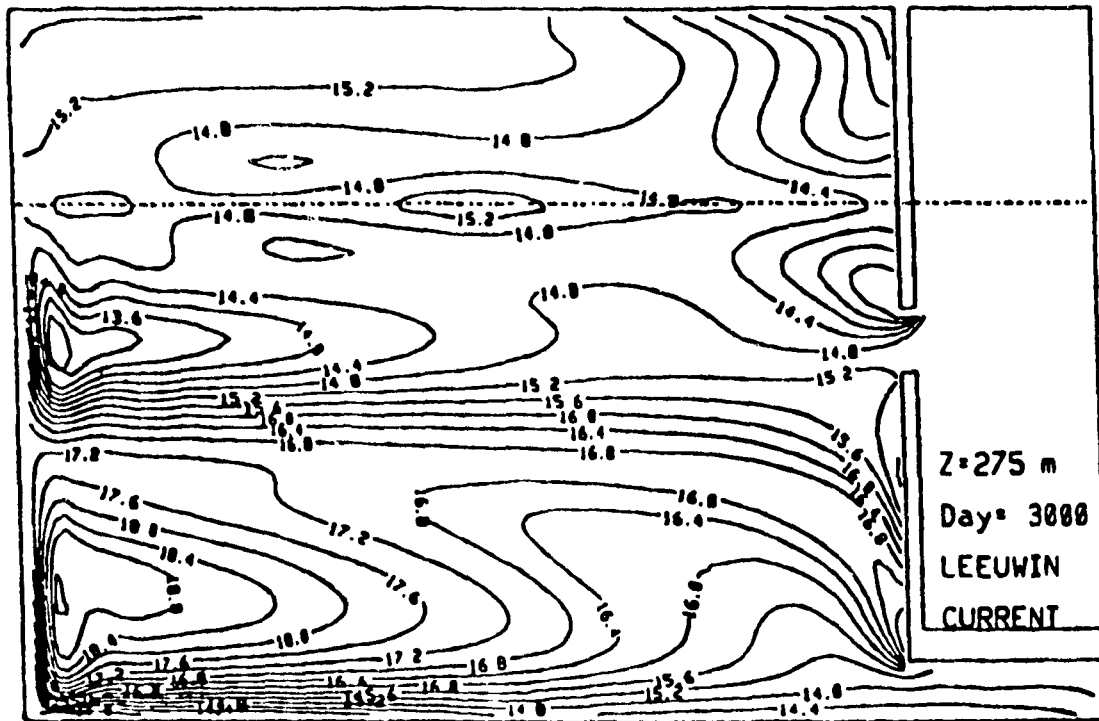
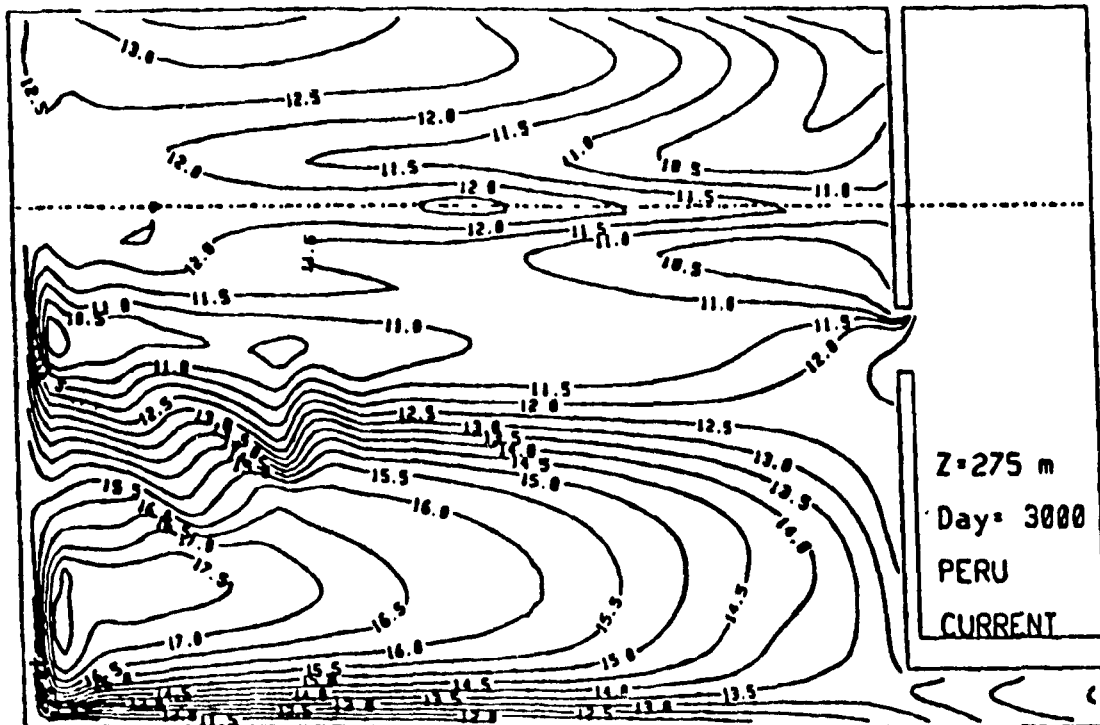


Fig.4.12. Velocity vectors at every 2nd gridpoint near the eastern boundary at z=275m (level 5): a) Leeuwin run b) Peru run.



a



b

Fig.4.13. Temperatures in °C at z=275m (level 5): a) Leeuwin run b) Peru run.

As discussed above, the surface temperatures in both runs are strongly constrained by the Haney flux condition at the air-sea interface. Away from the surface, the temperature contours conform much more closely to the double gyre pattern of the wind-driven circulation. The Ekman divergence and upwelling caused by the cyclonic circulation in the tropical gyre and the convergence and downwelling in the anticyclonic subtropical gyre account for the cool centre of the former and the warm centre of the latter (Fig 4.3). Deeper down, the tropical gyre can no longer be distinguished as clearly in the temperature contours, because the deep water pumped upward is not much cooler than the water at intermediate depths. The subtropical gyre is more evident because the temperature gradient crossed by the downwelling water is greater, so in a horizontal plane, the temperature difference between the vertically advected water and other areas is greater. The vertical section of temperature at 74°E for example shows how much deeper the subtropical gyre penetrates and also a slight southward slant with depth of the tropical gyre (Fig.4.14).

Since we have not imposed any form of salinity forcing at the upper boundary, the surface salinity field is fairly flat in both runs. At deeper levels, vertical advection produces horizontal salinity variations, but the different initial conditions in the two runs have opposite effects. In the Leeuwin run, the tropical gyre appears as a pool of higher salinity and the subtropical gyre as a pool of lower salinity, enhancing the density gradients associated with the temperature variations. In the Peru run, the initial profile has a salinity maximum just below the surface and the Ekman divergence in the tropical gyre tends to upwell fresher water, while the convergence in the subtropical gyre pumps more saline water downwards. The advection associated with the temperature discontinuity between the surface layers of the Indian and Pacific basins result in a salinity front at the gap in the first few layers

In the northwest corner, upwelling and cross-equatorial transport by the poleward western boundary current bring cooler water into the corner (Fig 4.3), although about 1°C less cool in the Leeuwin run. The surface flow over the rest of the northern hemisphere is more sedate and southeastward, and as the water travels out of the corner, it is warmed, causing the southwest-northeast tilt of the isotherms in the northern hemisphere and making the west coast of the

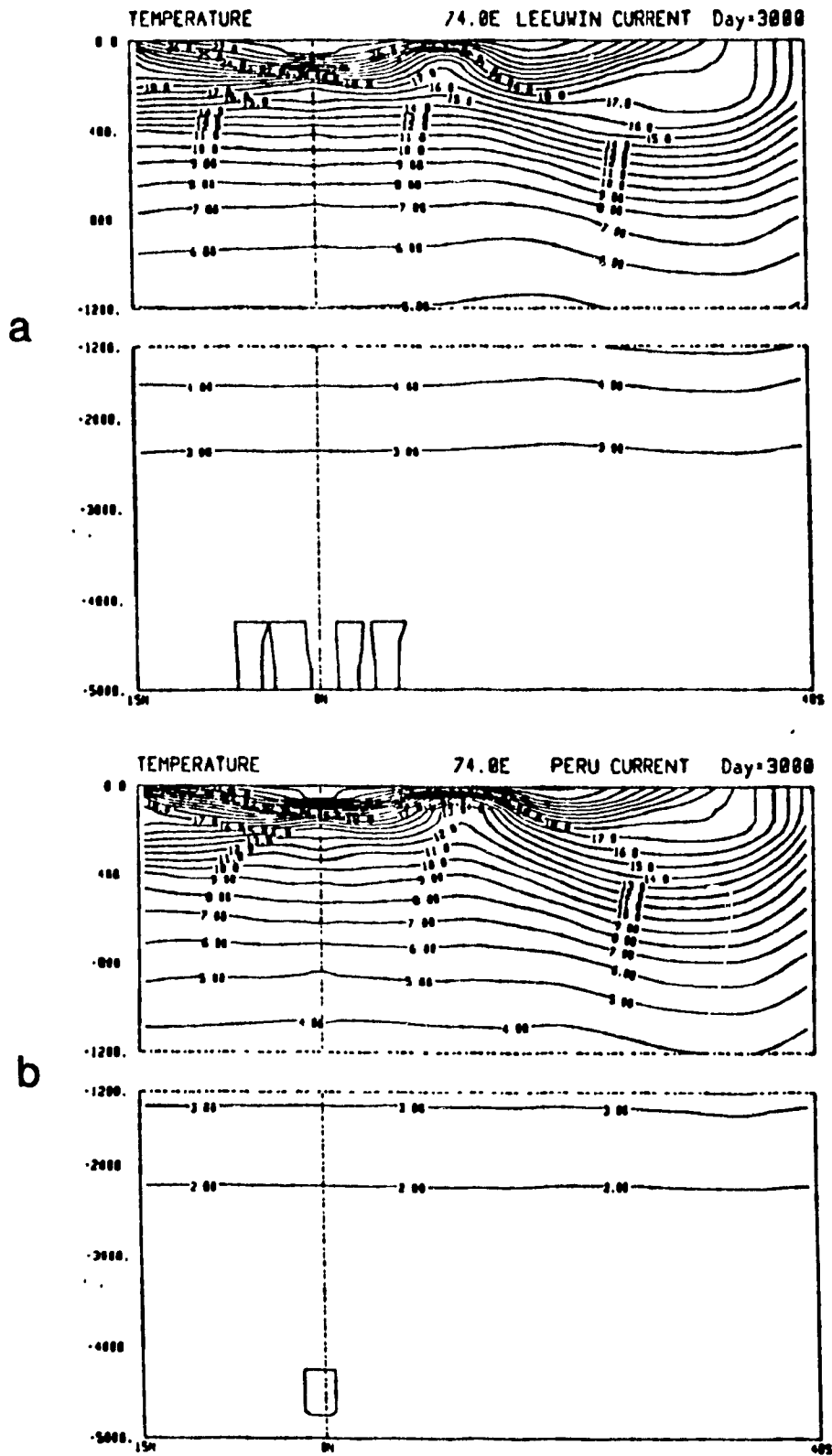


Fig.4.14. Meridional-vertical section of temperature (in °C) along 74°E: a) Leeuwin run b) Peru run.

ocean at least 1°C cooler than the east coast. A comparison of the meridional temperature sections at 46.0°E and 113.2°E (Fig.4.15 and Fig.4.10) shows how much deeper the mixed layer is along the east coast, where the equatorial wind is driving warm water onto the coast. The velocity difference vectors in the top layer (Fig.4.6) show that the northward western boundary current in the northern hemisphere is slightly weaker in the Leeuwin run. This current actually reverses direction at $z=275\text{m}$ (the same depth at which the eastern boundary current reverses) suggesting a thermohaline overturning cell with equatorward flow at this depth to balance the poleward transport at the surface (deduced from the steric height in Fig.4.7). In the southern hemisphere, the southward western boundary current closing the subtropical gyre (the model equivalent of the Agulhas current) advects warm water poleward to the southern boundary, releasing a substantial measure of heat to the atmosphere along the way and especially in the southwest corner. Both the northwest and the southwest corners of the Leeuwin ocean are warmer than in the Peru run.

At the latitude of the westward zonal jet in the southern hemisphere (the "South Equatorial Current"), the steric height along the western boundary rises more steeply in the Leeuwin run (Fig.4.16). (The magnitudes of the steric heights are also consistently higher in the warmer ocean of the Leeuwin run than in the Peru run.) The northward and southward branches along the western boundary are slightly augmented in the Leeuwin run (relative to the Peru run) from the difference vectors in Fig.4.6. This is a first indication that the effect of the throughflow reaches right to the opposite side of the ocean. Even with no net mass transport through the gap, the Indonesian throughflow is affecting the strength of the model SEC.

There are two major differences between the two runs which stand out in the plots of velocity difference at $z=20\text{m}$ (Fig 4.6). The two features are the westward jet from the Pacific and the band of eastward flow towards the Australian coast. Both of these are visible more than halfway across the ocean, until the zonal flow is broken up by the eddies of the Peru run.

It is not immediately apparent what proportion of the westward jet issuing from the Pacific in the difference field is due to the subtraction of the eastward throughflow in the Peru run. The gyre

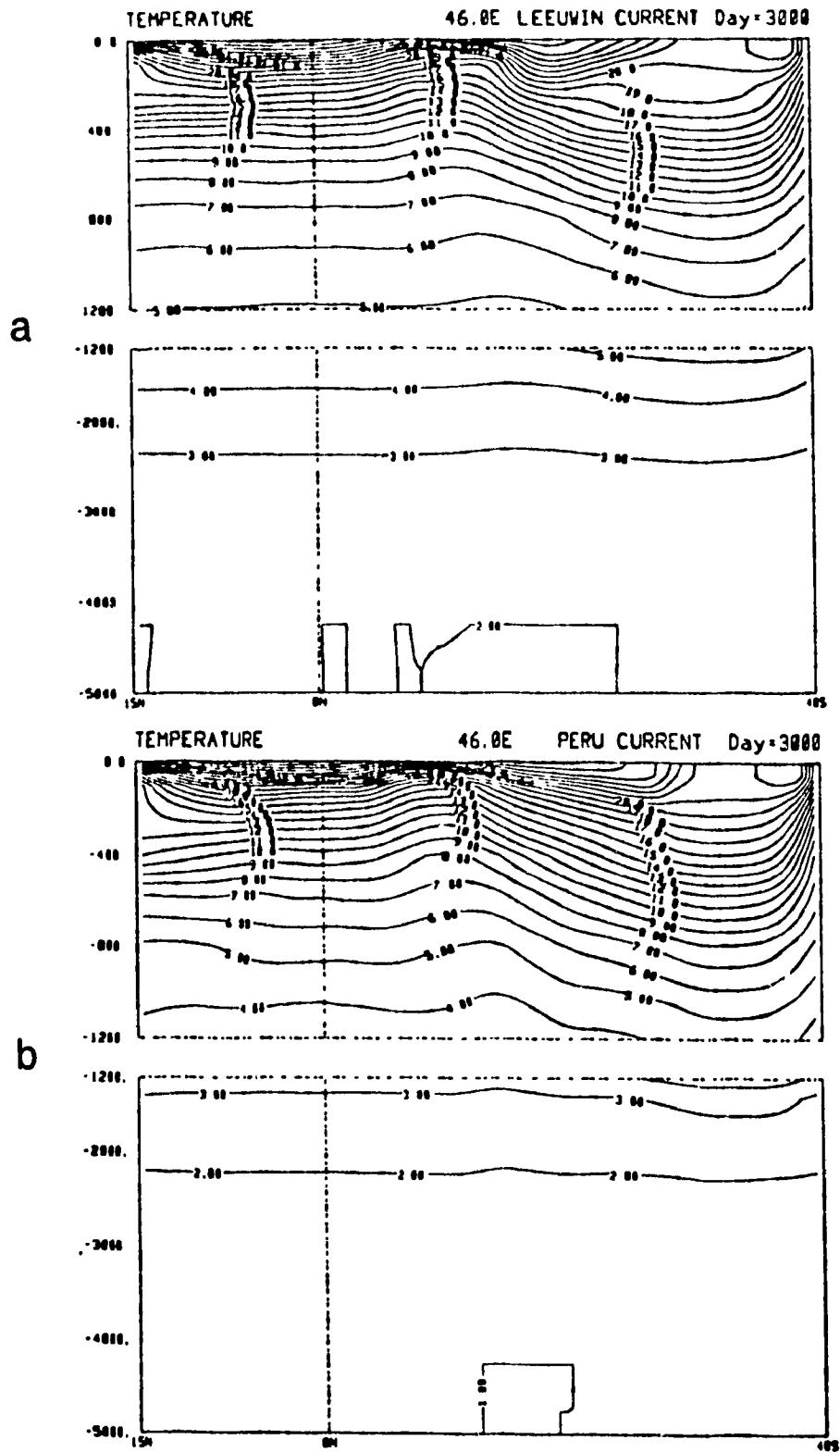


Fig.4.15. Meridional-vertical section of temperature (in °C) along 46°E (two grid-points from the western boundary): a) Leeuwin run b) Peru run.

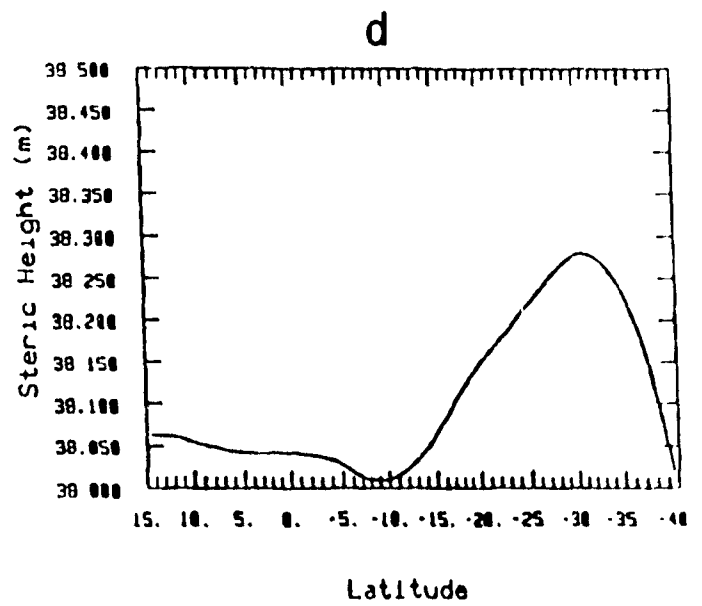
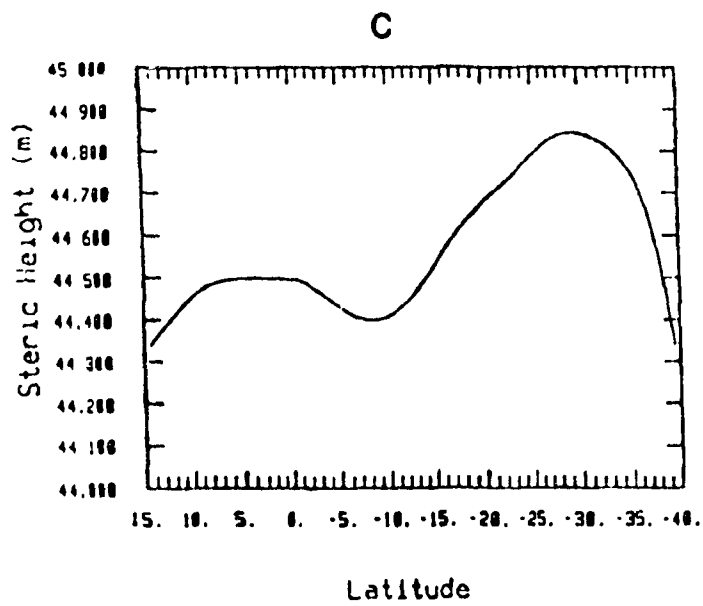
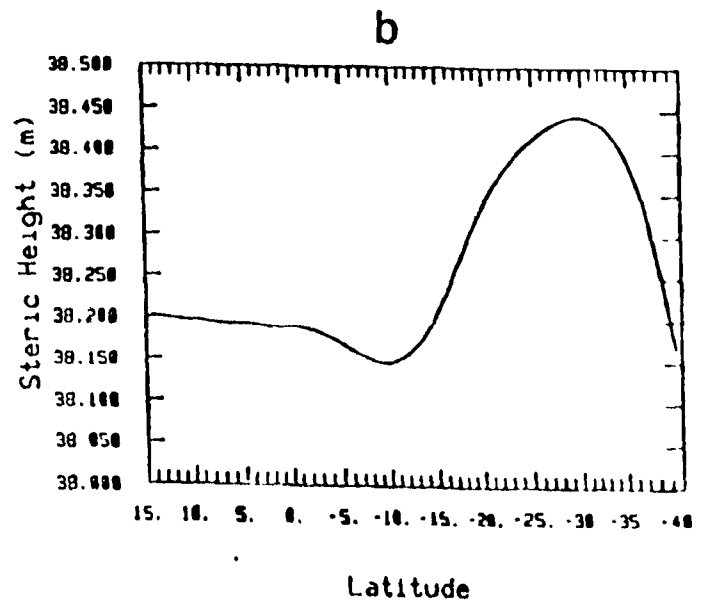
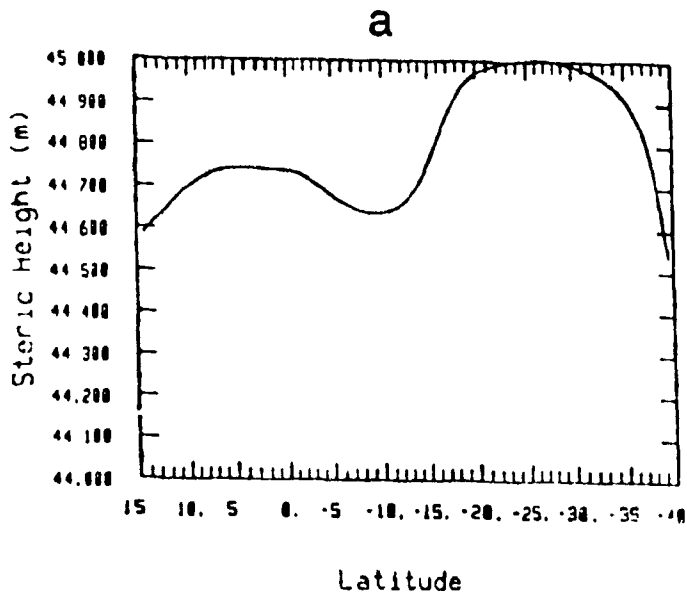


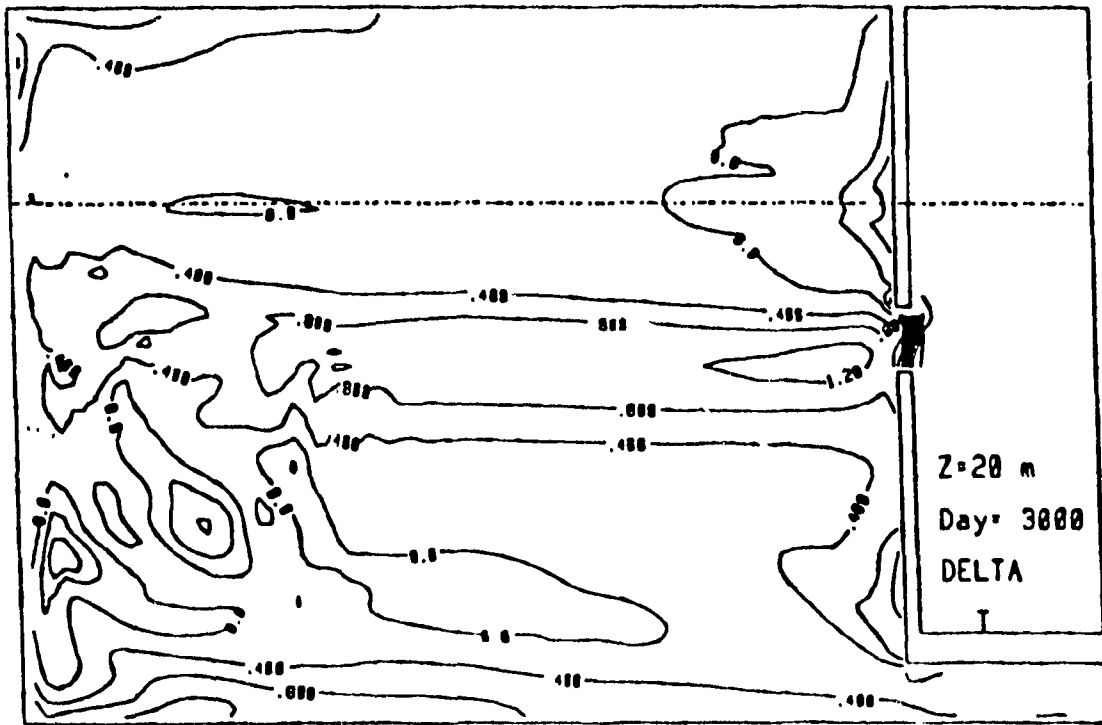
Fig.4.16. Steric height in m along the western boundary (with respect to a reference depth of 1600m) at $z=20\text{m}$ and $z=275\text{m}$ (levels 1 and 5): a) and b) Leeuwin run c) and d) Peru run.

circulation is too strong for the throughflow to appear as a distinct zonal jet in either individual run, but it is revealed in the difference field where the Sverdrup circulations in the two runs essentially cancel each other. The throughflow in the Peru run seems to be so much more dynamic than the throughflow in the Leeuwin run that it is not implausible for it to be the sole cause of the weaker SEC and western boundary currents in the Peru run. However, the temperature sections described in the next paragraph will make it clear that heat from the Pacific in the Leeuwin run is being transported right to the western boundary.

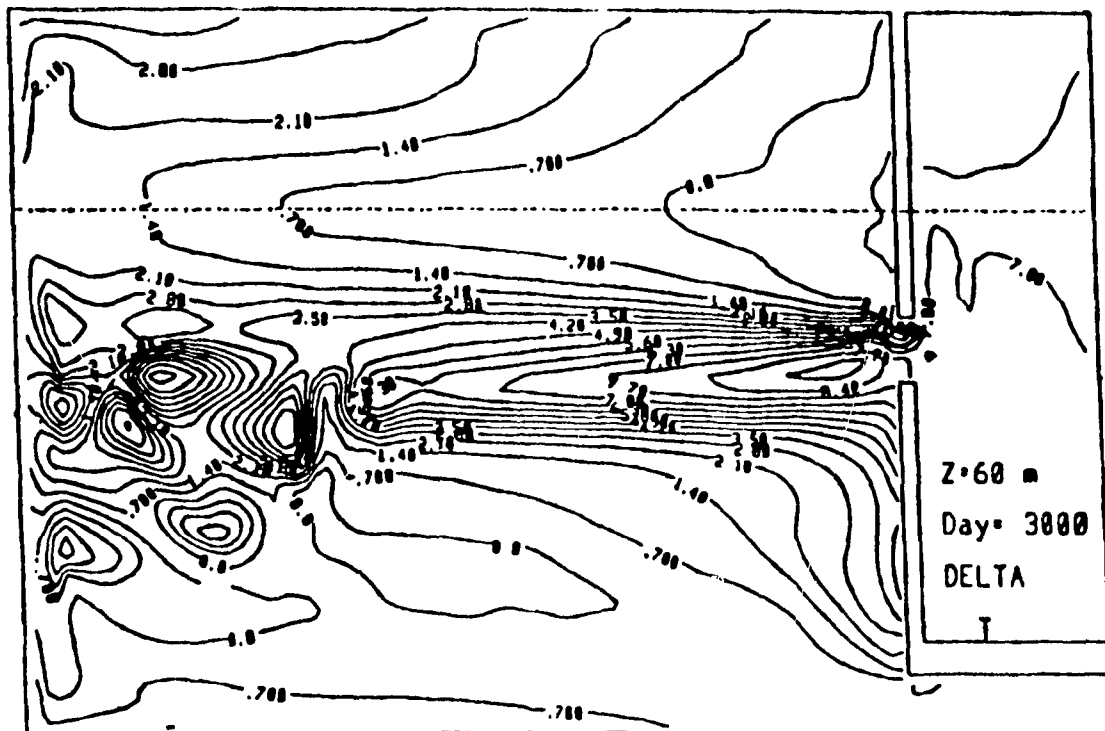
The plot of temperature difference at $z=60\text{m}$ (Fig.4.17) shows the throughflow reaching right across the ocean, although the eddies again confuse the signal in the western region. Vertical sections of temperature difference along each longitude show the throughflow as a distinct warm core just below the Haney-forced layer (Fig.4.18). (The throughflow is in fact visible in ΔT even at the first model level, where temperature variations are strongly damped by the Haney flux condition). Near the eastern boundary, the warm core is elongated southward because convection and downwelling are causing warmer temperatures all along the coast in the Leeuwin run. Further west, the core is more compact and is more or less centred on the SEC. The difference in temperature of 6°C in the SEC at 74°E cannot come only from the eastward throughflow in the Peru run: the warm throughflow of the Leeuwin run must therefore penetrate this far. At the western boundary, there is still a warm subsurface core but it is fragmented by the warm and cool pools associated with the Peru eddies.

The second difference that we cited was the band of eastward flow geostrophically balancing the greater meridional steric height gradient caused by the warm throughflow in the Leeuwin run. This zonal flow is not confined to the neighbourhood of the eastern boundary but appears to decay southward as the westward distance from the boundary increases (Fig.4.6).

Both of the two features discussed above also reverse direction at $z=275\text{m}$ (Fig 4.19). The strong surface flow into the Pacific in the Peru run must be compensated for at deeper levels to ensure that the depth-integrated transport through the Indonesian passage vanishes. In the east, the strength of the offshore flow associated with the reversed meridional density gradient of the Leeuwin



a



b

Fig.4.17. Difference in temperature (Leeuwin - Peru) at a) $z=20m$ and b) $z=60m$ (levels 1 and 2)

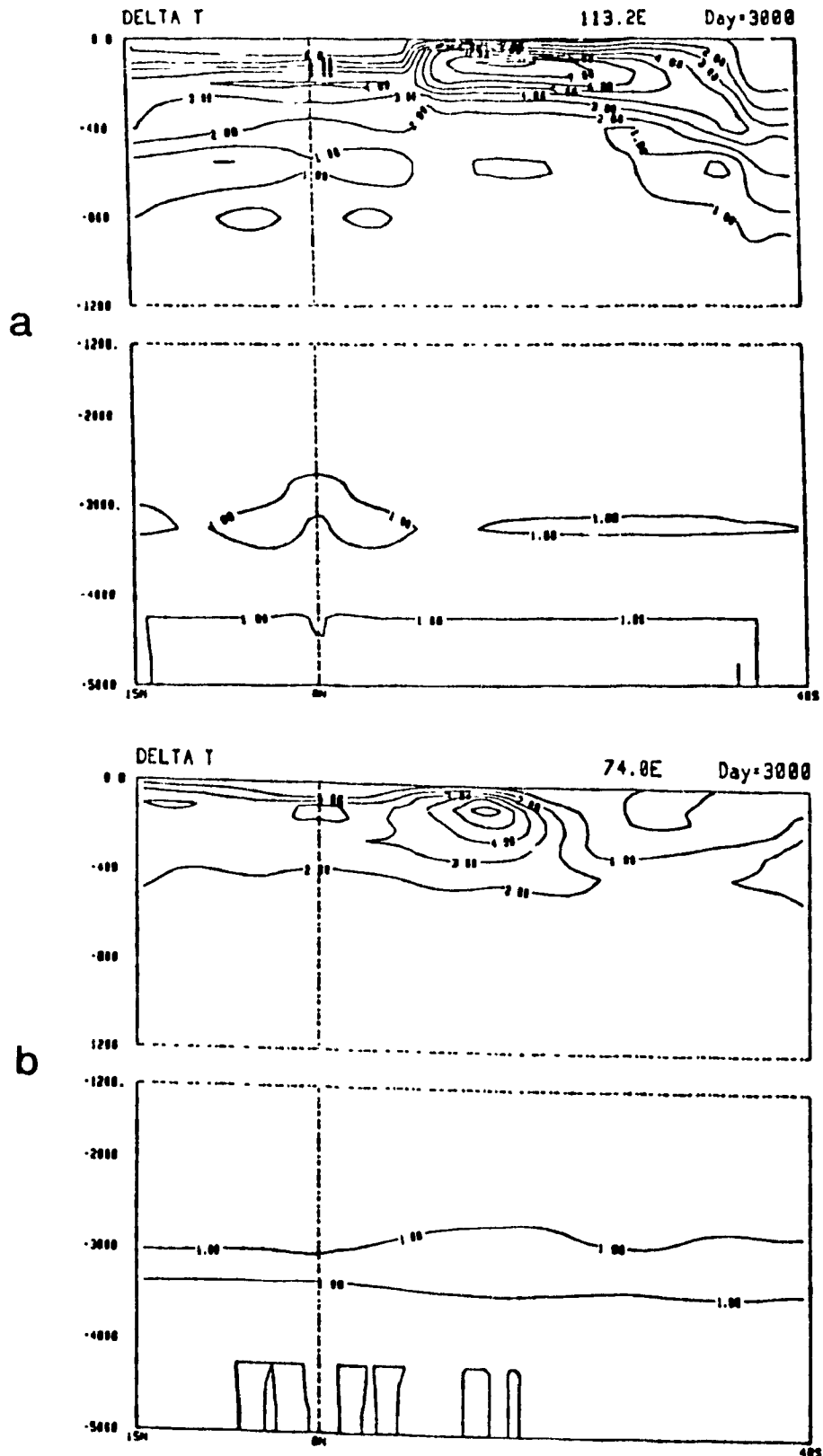


Fig 4.18. Difference in temperature (Leeuwin - Peru) along a) 113.2°E b) 74°E and c) 46°E.

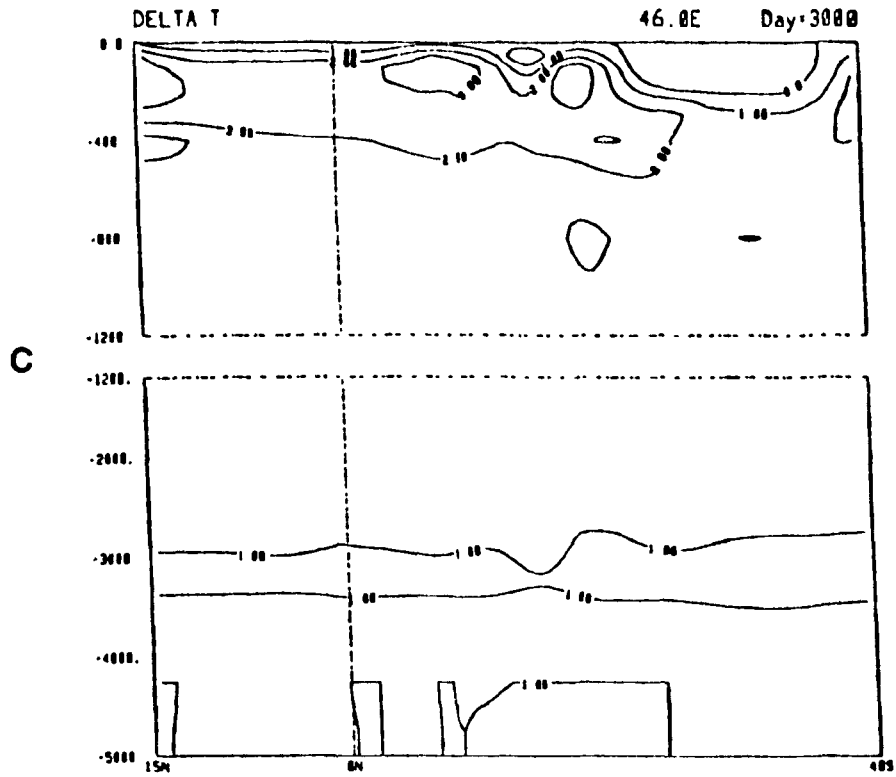


Fig.4.18. Cont. Difference in temperature (Leeuwin - Peru) along a) 113°E b) 74°E and c) 46°E.

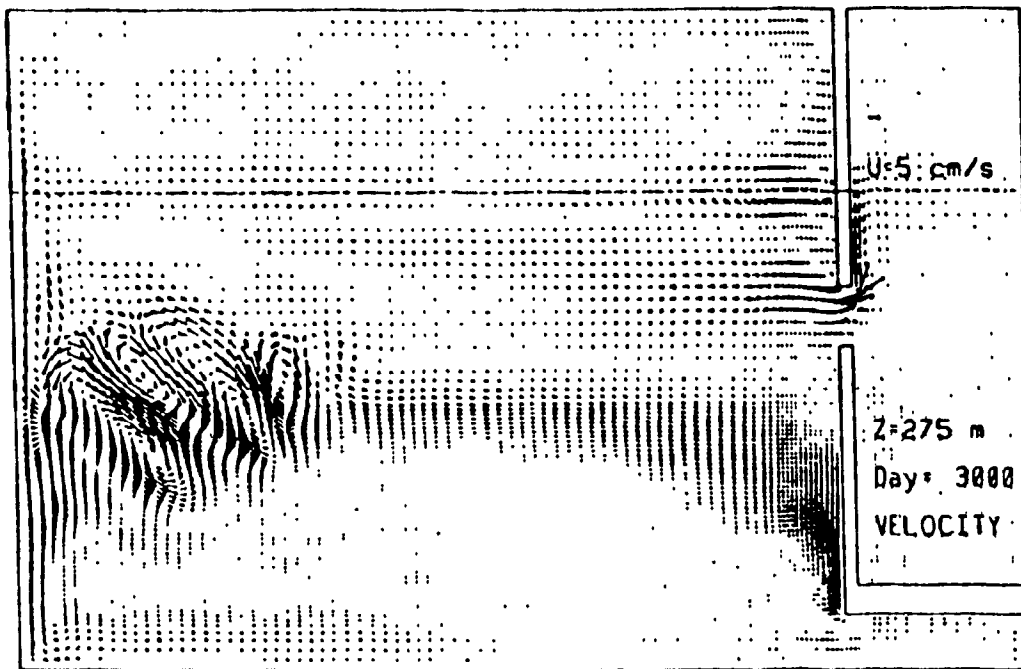


Fig.4.19. Velocity difference (Leeuwin - Peru) at z=275m (level 5).

Undercurrent is seen from the temperature contours at $z=275\text{m}$ (Fig.4.13): a tongue of cold water is advected out northwestward from the southern tip of Australia.

At much greater depths, the higher baroclinic modes are revealed as the strength of the surface intensified first mode fades. Fig 4.20 shows the alternating bands of eastward and westward flow at $z=4750\text{m}$, especially in the Leeuwin run.

4.3. The Heat Budget

The surface heat fluxes are mapped in Fig.4.21. In both runs, the Haney flux condition is heating almost the entire tropical region between about 17 or 18°S to the northern boundary at 15°N . Poleward of this, the ocean is losing heat to the atmosphere in most regions.

At low latitudes in the southern hemisphere, the location of the cool tropical gyre is easily identified in the map of surface heat fluxes. The surface heat fluxes are in general smaller in the subtropical gyre where the Haney temperature distribution is more closely adhered to, but the largest exchange anywhere in the model Indian ocean takes place in the southwest corner, where the "Agulhas" Current reflects. The advection of warm water by the southward western boundary current stands out clearly. The heat flux is positive (i.e. the ocean is warmer than the atmosphere) along the entire southern border, despite the upwelling there, but is smaller in the Peru run where the upwelled water is even cooler. A stripe of negative heat flux (heat into the ocean) is seen along the 35°S latitude circle, stretching right into the Great Australian Bight, due to the equatorward advection of cooler temperatures by the return flow of the anticyclonic subtropical gyre. Another localized effect is the narrow strip of positive heat flux along the equator near the eastern boundary, caused by the accumulation of the warmest surface water against the eastern shore under the action of the westerly equatorial wind. (This is perhaps a misleading representation of the real Indian Ocean, where winds reverse seasonally.)

The biggest difference between the heat flux fields of the two runs is the warm eastern boundary

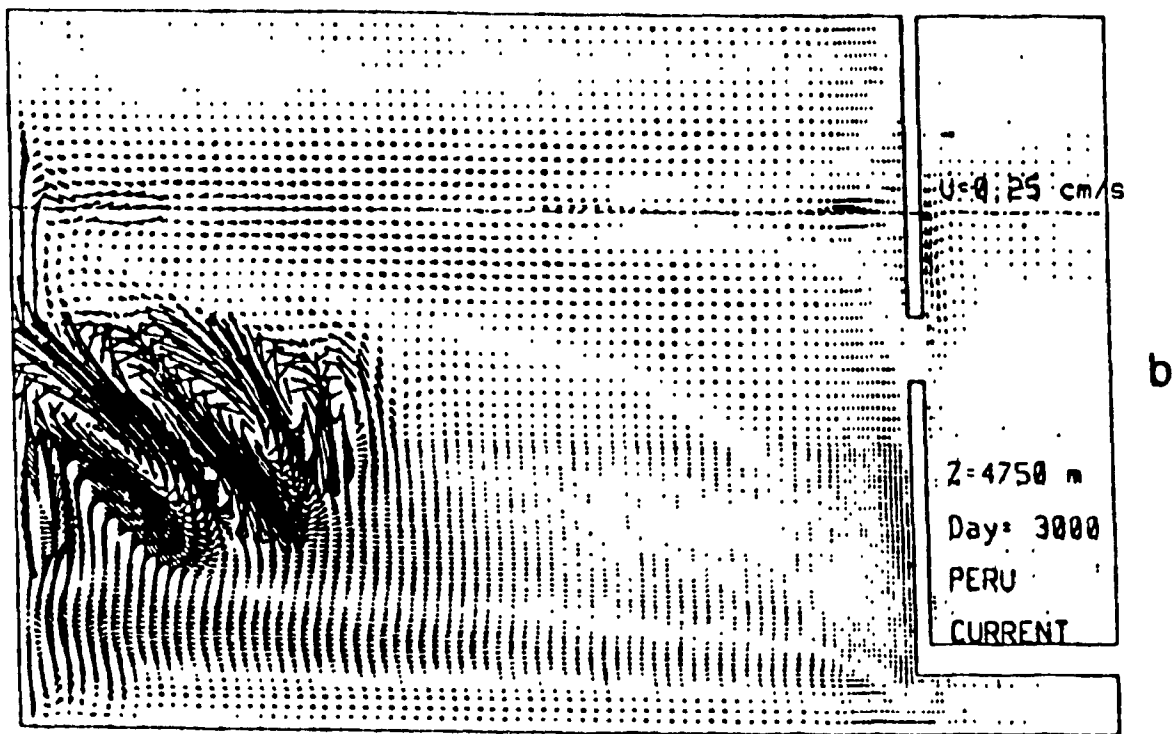
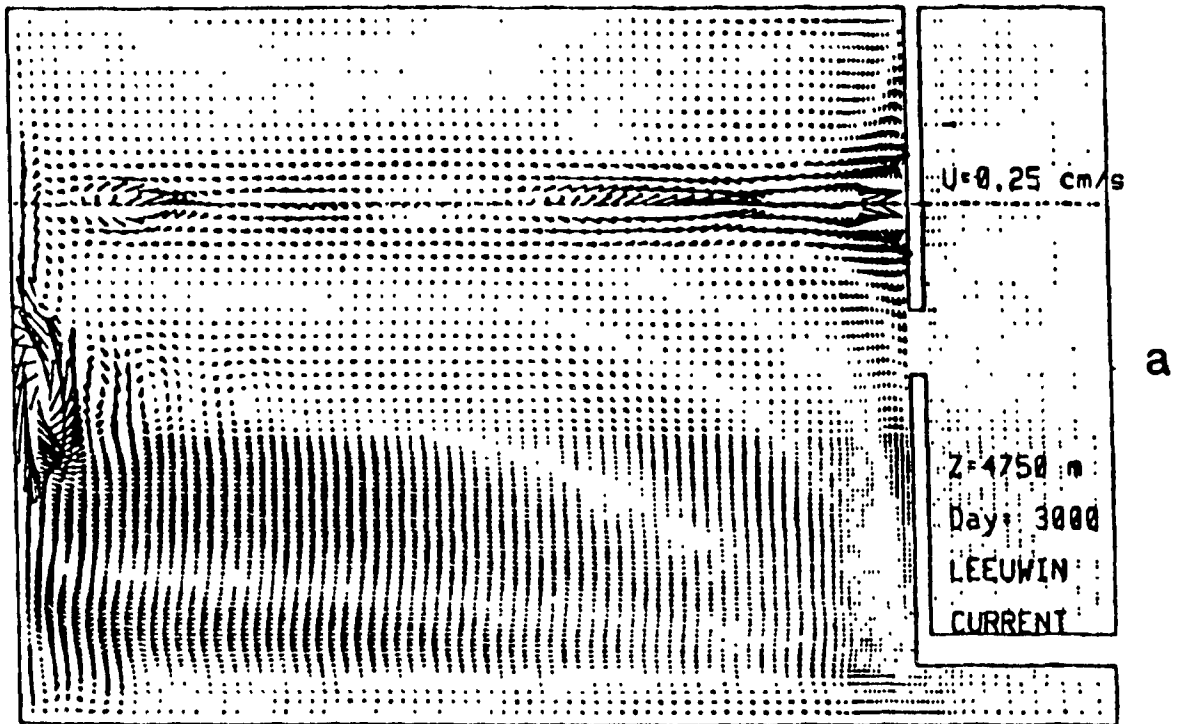
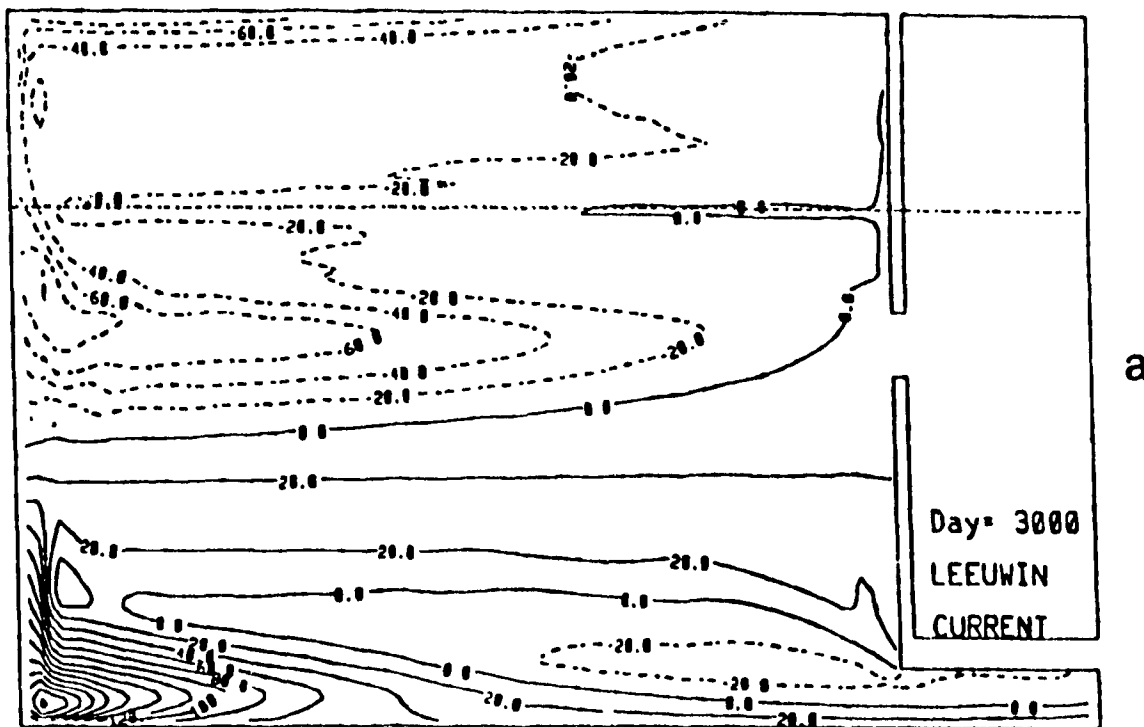
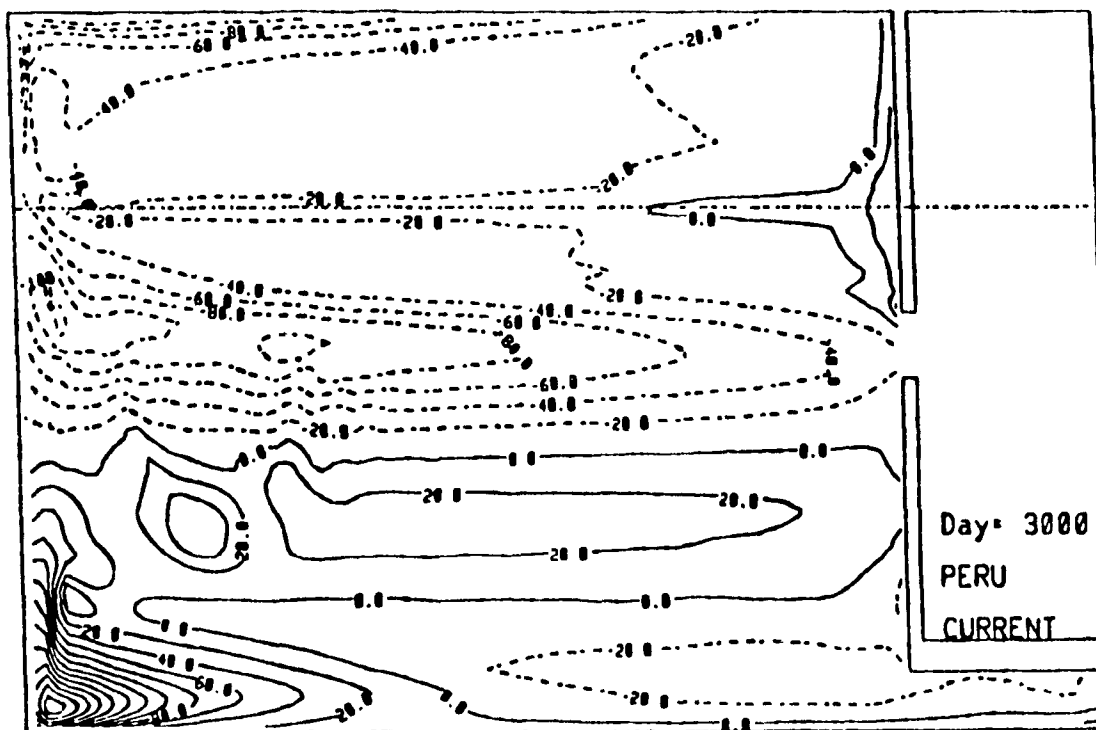


Fig.4 20. Horizontal velocities at z=4750m (level 17): a) Leeuwin run b) Peru run.



a



b

Fig.4.21. Surface heat fluxes $Q = \lambda(T - T^*)$ in W/m^2 : a) Leeuwin run b) Peru run. Positive (solid) contours indicate that heat is being released by the ocean.

of the Leeuwin run. Coastal upwelling in the cooler Peru run actually results in a patch of negative heat flux (heat into the ocean) at approximately 30°S and this is the site of the largest difference in surface heat flux anywhere: over 50 W/m² more is being emitted in the Leeuwin case. In the difference field (Fig.4.22), the throughflow can again be seen reaching across to the western boundary, although the magnitude of the difference fades westward. In the Leeuwin run then, less heat is taken up by the cool tropical gyre and the zone of negative heat flux does not extend right to the eastern boundary. The extra heat transported by the South Equatorial Current in the Leeuwin run is not apparently transferred to the western boundary currents, as the difference in surface heat flux there (or in temperature at either the first or second levels) is negligible. It is true that more heat is lost in the southwest corner of the Leeuwin run (up to 50 W/m² more) and less heat (nearly 40 W/m² less) is gained in the northwest corner, but this is due to the difference in temperature of the upwelled water. More heat is also lost along the southern edge of the domain. The only places where the Peru surface heat budget is actually warmer than in the Leeuwin run is in the warmest eddies and on the equator at the eastern boundary, and the latter is a spurious heat source caused by numerical diffusion (as will be discussed more thoroughly in Chapter 5).

The role of the oceans in modulating the extreme climates otherwise produced by the unequal interception of solar radiation in different latitudinal belts can be evaluated by integrating the meridional heat transport over each latitudinal section. The total transport is the sum of the advective and diffusive components:

$$(15) \quad F = F_{adv} + F_{diff}$$

$$(16) \quad F_{adv} = \rho_0 C_p \int_{\lambda_w}^{\lambda_e} \int_{-H}^0 (vT) (\cos\phi d\lambda) dz$$

$$(17) \quad F_{diff} = -\rho_0 C_p \int_{\lambda_w}^{\lambda_e} \int_{-H}^0 A_{TH} \left(\frac{\partial T}{\partial \lambda} \right) (\cos\phi d\lambda) dz$$

where λ_e and λ_w are the longitudes of the east and west boundaries, H is the total depth and the

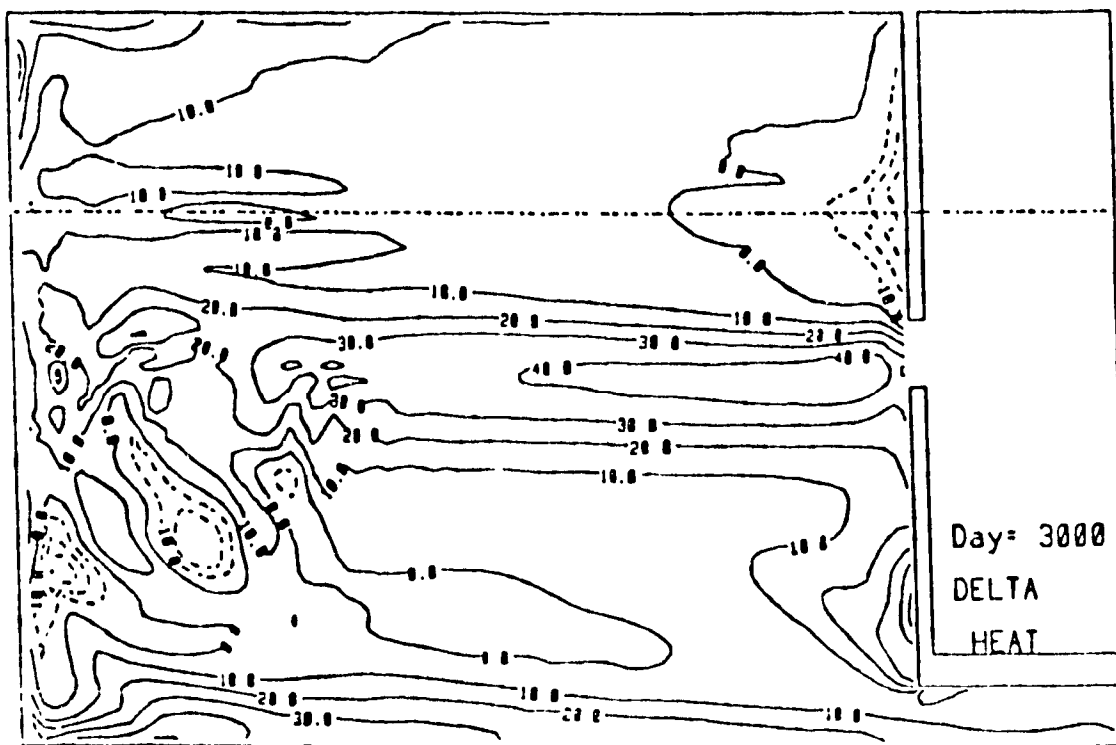


Fig.4.22. Difference in surface heat flux (Leeuwin - Peru) in W/m^2 . Positive (solid) contours indicate that the Leeuwin ocean is releasing more heat to the atmosphere.

other parameters are as defined in Section 3.2.

The total advection can be decomposed into the Ekman transport (calculated from the surface wind stress and the temperatures in the top model layer), a barotropic gyre transport F_{zmean} (advection of the vertically averaged temperature by the vertically averaged velocity) and a baroclinic term F_{zeddy} (which involves the departures of v and T from the vertical mean).

$$(18) \quad F_{Ekman} = -\frac{C_p}{f \lambda_w} \int_{\lambda_w}^{\lambda_e} r^\lambda \{ T_1 - (\bar{T}) \} (a \cos \phi d\lambda)$$

$$(19) \quad F_{zmean} = \rho_0 C_p H \int_{\lambda_w}^{\lambda_e} (\bar{v}) (\bar{T}) (a \cos \phi d\lambda)$$

$$(20) \quad F_{zeddy} = F_{adv} - F_{Ekman} - F_{zmean}$$

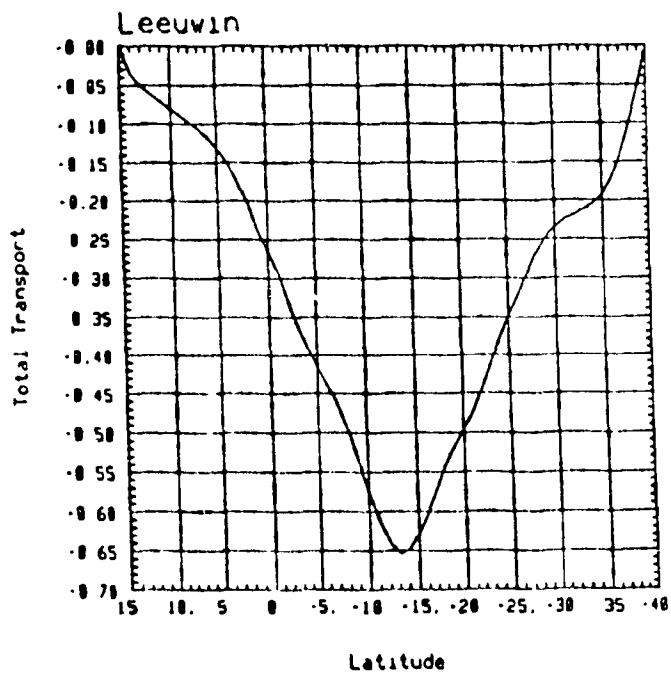
where $(\bar{\quad})$ represents a vertical average over the whole depth H (assumed constant) and T_1 is the temperature in the first model layer. Alternatively, the advective component can be sorted out into F_{xmean} (advection of the zonally averaged temperature by the zonally averaged velocity) and a remainder F_{xeddy} (variations of T and v along a latitude circle).

$$(21) \quad F_{xmean} = \rho_0 C_p L \int_{-H}^0 [v] [\bar{T}] dz$$

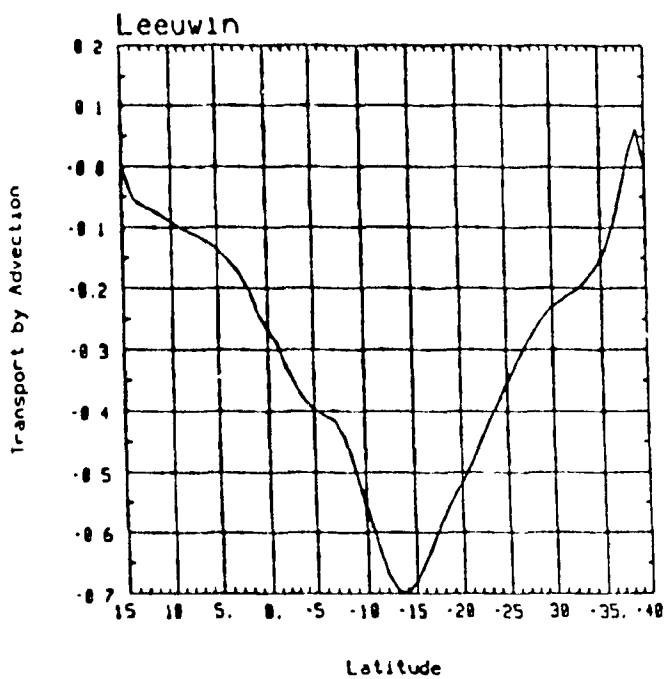
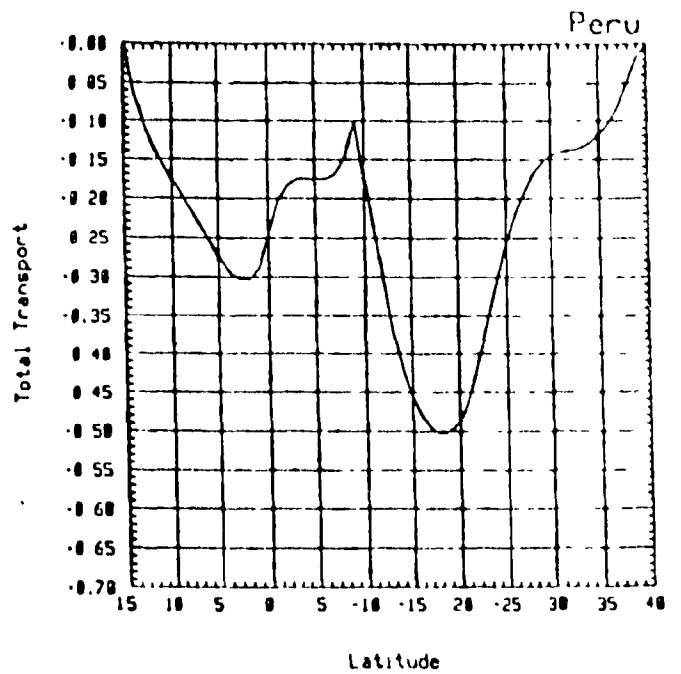
$$(22) \quad F_{xeddy} = F_{adv} - F_{xmean}$$

where $[\quad]$ represents a zonal average over the width of the basin and L is the width of the basin at that latitude, i.e. $L = a \cos(\lambda_e - \lambda_w)$.

The components of the northward heat transport are illustrated in Fig.4.23 a through h (the appropriate vertical scale differs from plot to plot). In both runs, the meridional heat transport is southward at all latitudes and is dominated by the advective component (Fig.4.23b) (the diffusive term (Fig.4.23c) is small and usually opposite in sign). The "zmean" term is very small because in the wind-driven gyres, transports in opposite directions at different longitudes almost cancel one another, and also because the barotropic velocity is very small. The Ekman transport in the warm surface



a



b

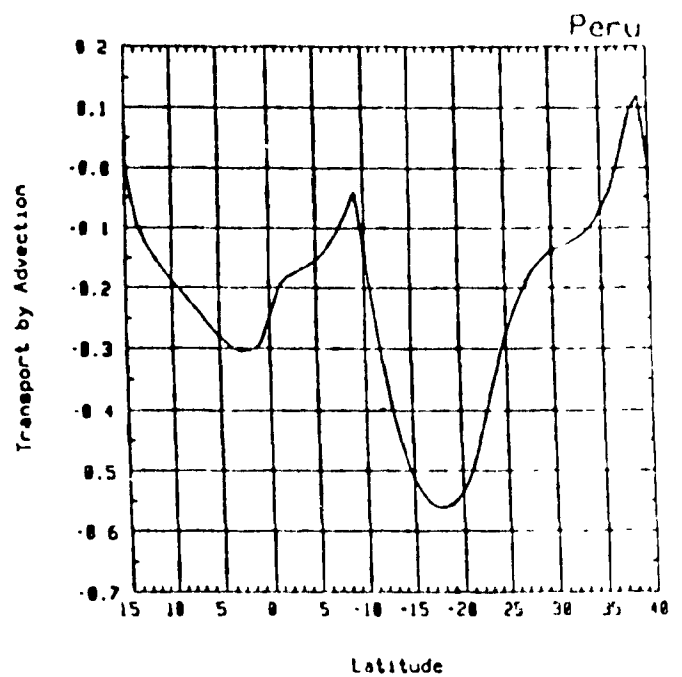
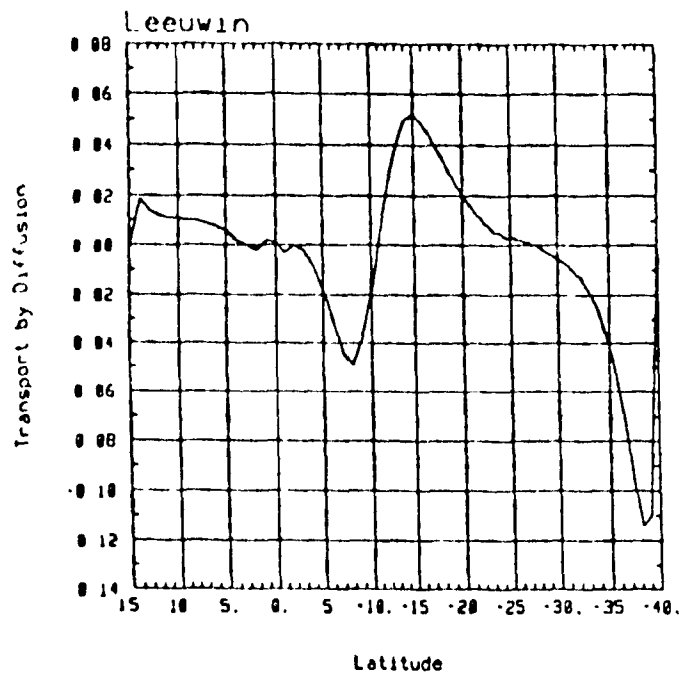
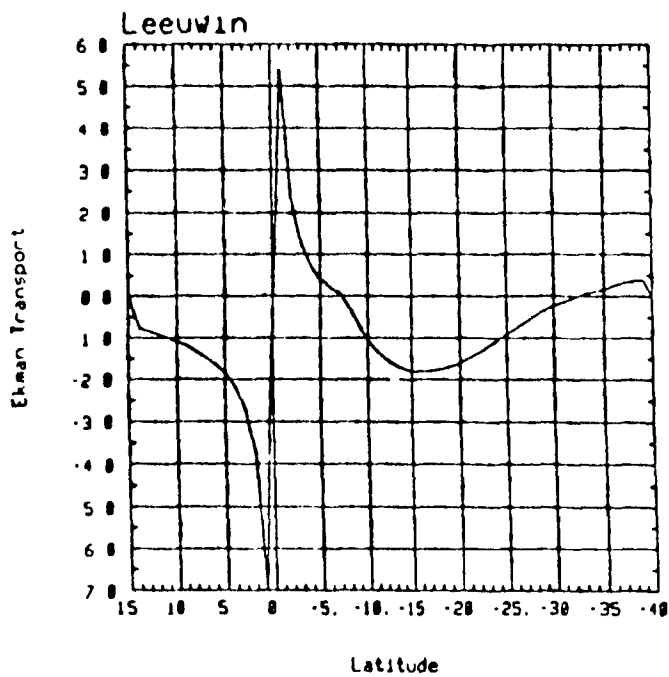
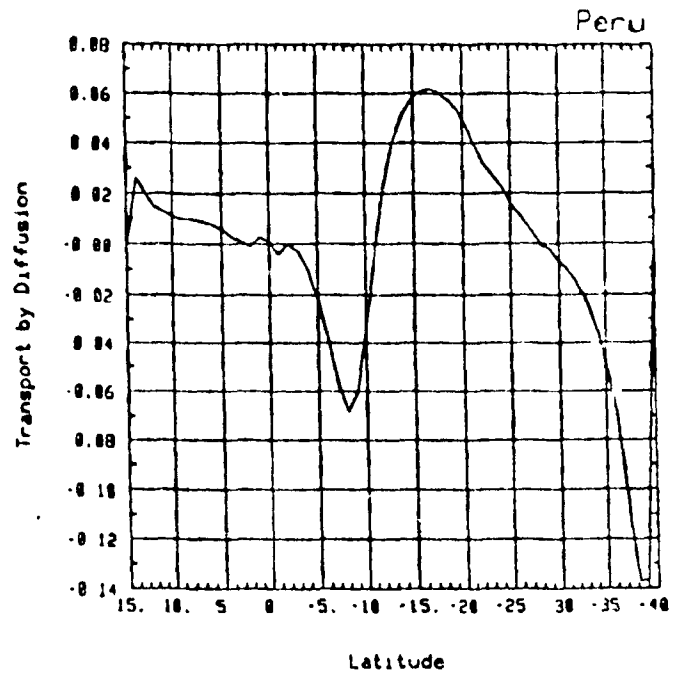


Fig.4.23. Northward heat transport in 10^{15} W for the Leeuwin and Peru runs: a) total transport b) total transport by advection c) transport by diffusion d) Ekman transport e) transport by zmean f) transport by zeddy g) transport by xmean h) transport by xeddy.



c



d

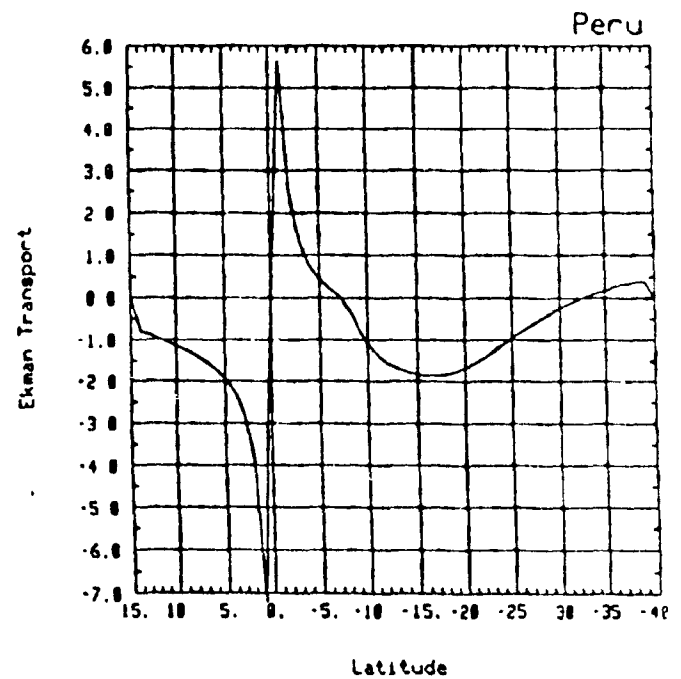


Fig 4 23 Cont. Northward heat transport in 10^{15} W for the Leeuwin and Peru runs:
 a) total transport b) total transport by advection c) transport by diffusion d) Ekman transport e) transport by zmean f) transport by zeddy g) transport by xmean h) transport by xeddy.

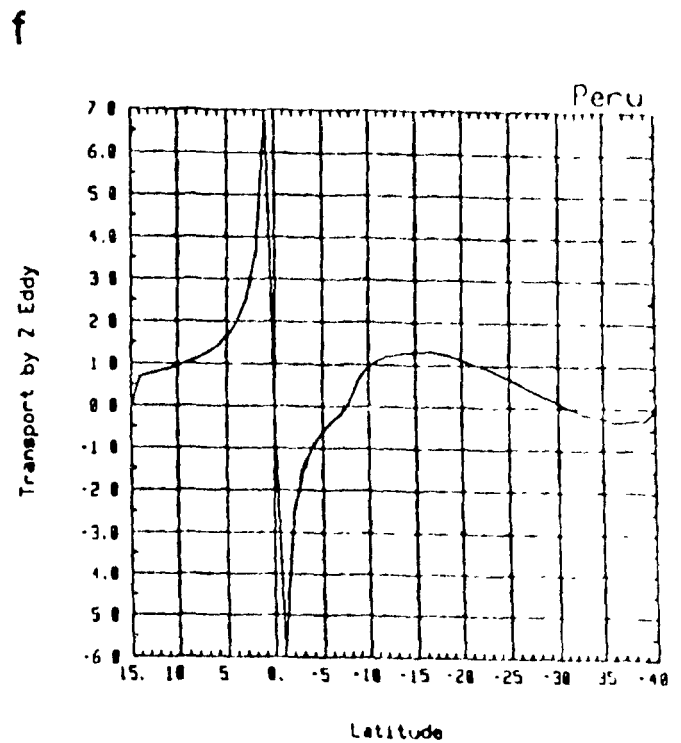
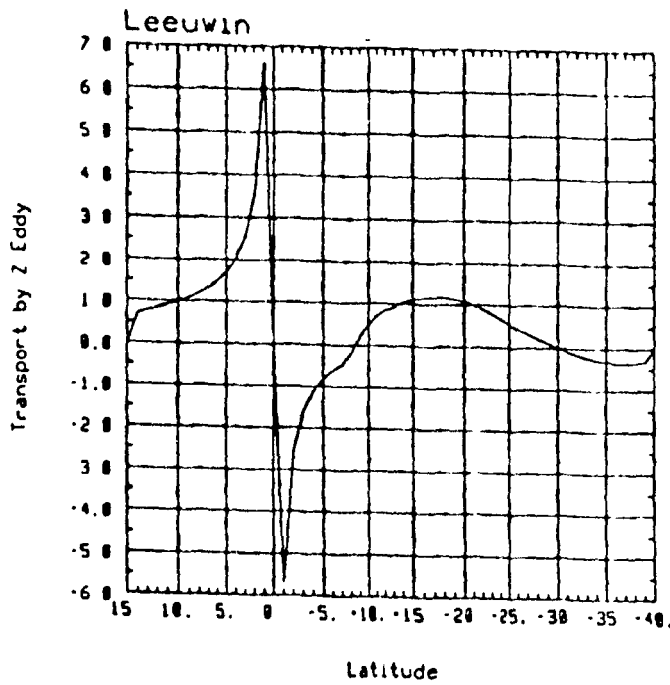
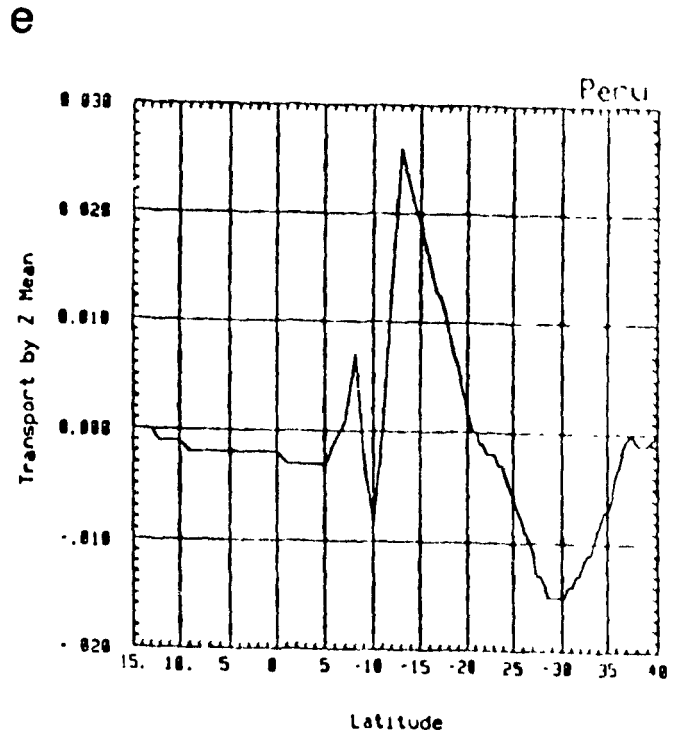
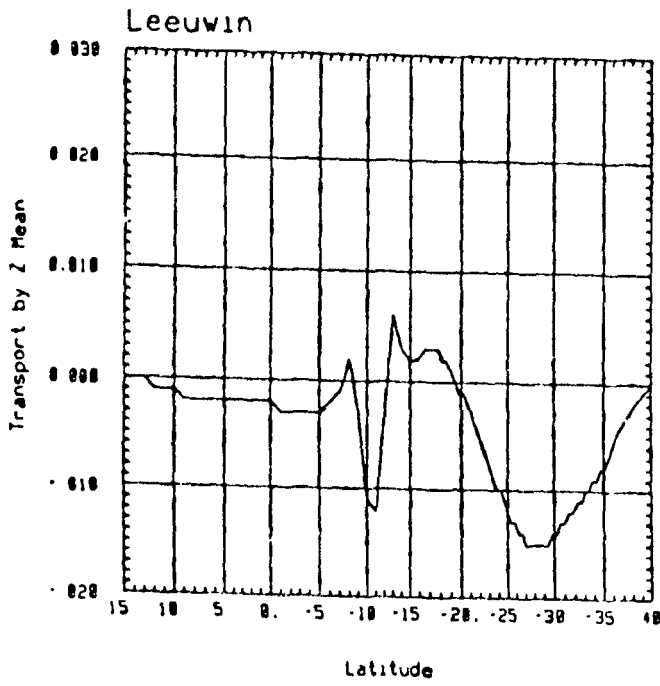


Fig.4 23. Cont. Northward heat transport in 10^{15} W for the Leeuwin and Peru runs
 a) total transport b) total transport by advection c) transport by diffusion d) Ekman transport e) transport by zmean f) transport by zeddy g) transport by xmean h) transport by xeddy.

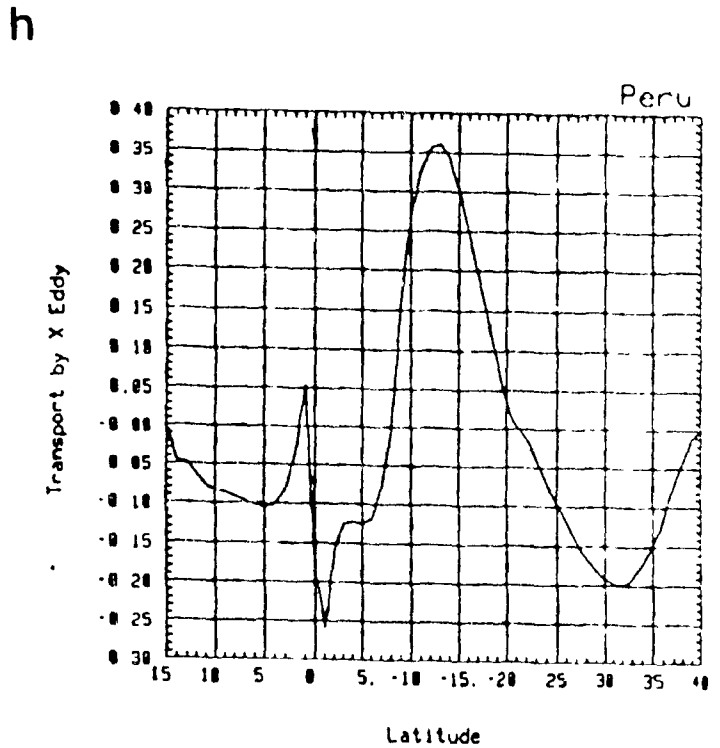
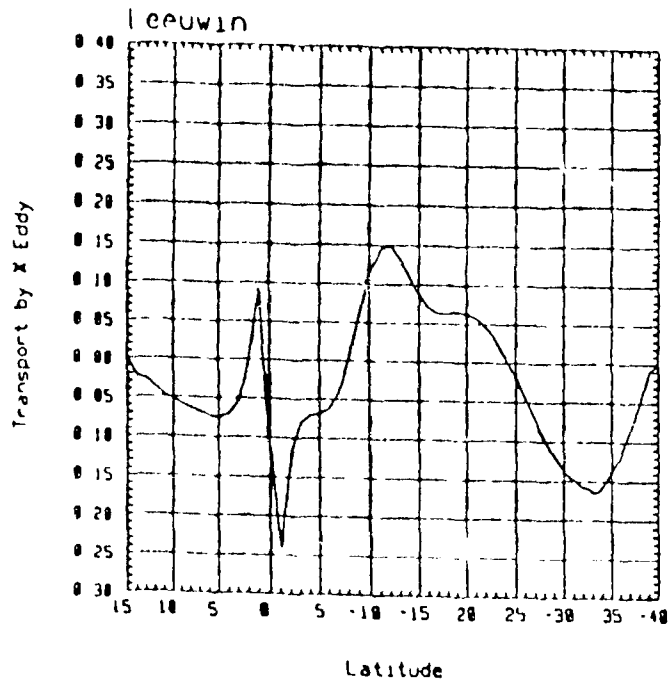
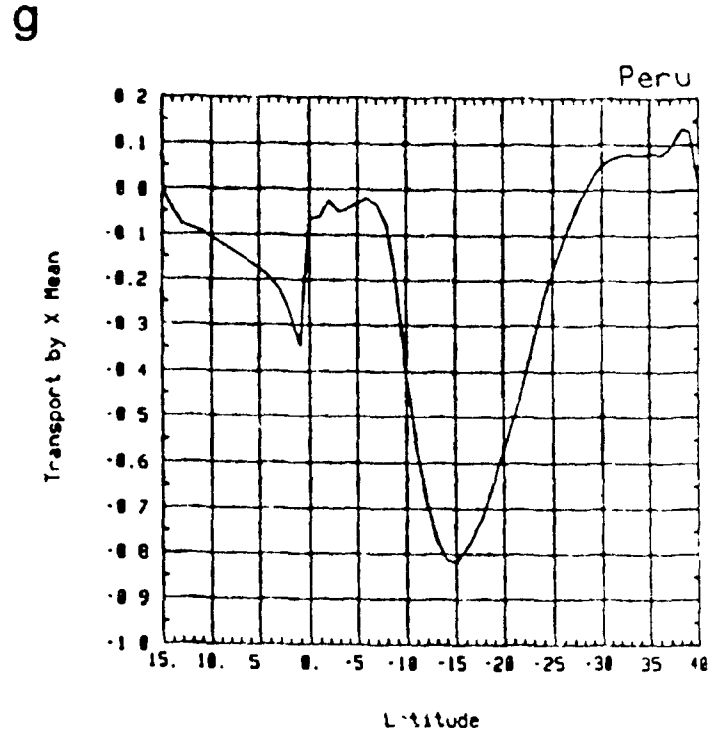
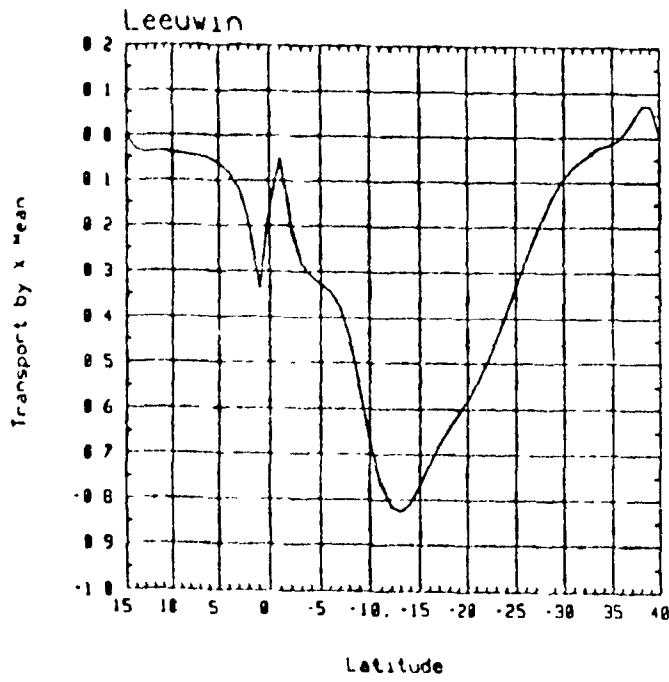


Fig 4.23. Cont Northward heat transport in 10^{15} W for the Leeuwin and Peru runs:
 a) total transport b) total transport by advection c) transport by diffusion d) Ekman transport e) transport by zmean f) transport by zeddy g) transport by xmean h) transport by xeddy.

layer is very large, especially near the equator where the Coriolis parameter is small, but is nearly balanced by the "zddy" term, because water pumped by the Ekman convergences and divergences is diverted into shallow closed cells, so the surface drift is compensated for at slightly greater depths. The strong peaks caused by the Ekman convergence onto the equator are not quite identical for the two runs, because the surface temperature distribution is different. The "zddy" term also contains the thermohaline contribution from all levels. The Leeuwin run is seen to transport more heat southward. The same is true of the total heat transport the Leeuwin run has more heat to advect southward because the whole water column is warmer. Only in the northern hemisphere does the Peru run produce a greater southward transport, because the thermohaline overturning cell there (northward advection of warm surface water and an equatorward return branch at $z = 275\text{m}$) contributes slightly more in the warmer Leeuwin run, and because the northward western boundary current is cooler in the Peru run (cool water transported northward is equivalent to warm water transported southward).

The real Indian Ocean exports heat to other oceans because it receives more energy at low latitudes than it can lose at high latitudes (Hsiung, 1985). The zonally-integrated SST (sea surface temperature) in Fig 4 24a shows the Indian Ocean to be distinctly warmer than either the Atlantic or Pacific, and Fig 4 24b shows that the reason must be at least partly due to the cool eastern boundaries of the latter two oceans (compared to the western boundaries), a feature that is not present in the Indian Ocean.

The appearance of the curve of total southward heat transport versus latitude that we have obtained in our Leeuwin run is almost surprisingly good. Three independent calculations of the transport in the Indian Ocean are given in Fig 4 25. The three estimates are all based on the surface energy balance method (Hsiung, 1985) which relies on bulk parametrization formulas and long term compilations of ship data (wind speed, relative humidity, cloud cover, sea surface temperature SST and air temperature at ship level). Hsiung (1985) explains that the disagreement between her estimate (Fig.4.25b) and the others is at least partly due to the different choice of an eastern limit for

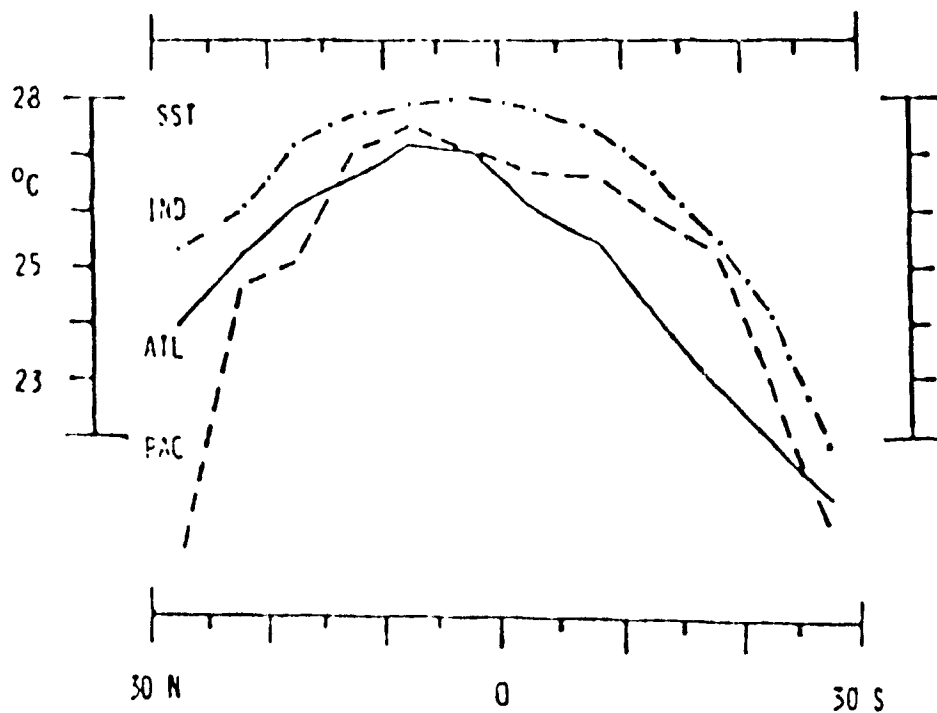


Fig 4 24 a) Annual mean meridional profiles of sea surface temperature in °C for the Indian, Atlantic and Pacific Oceans (taken from Hastenrath, 1980)

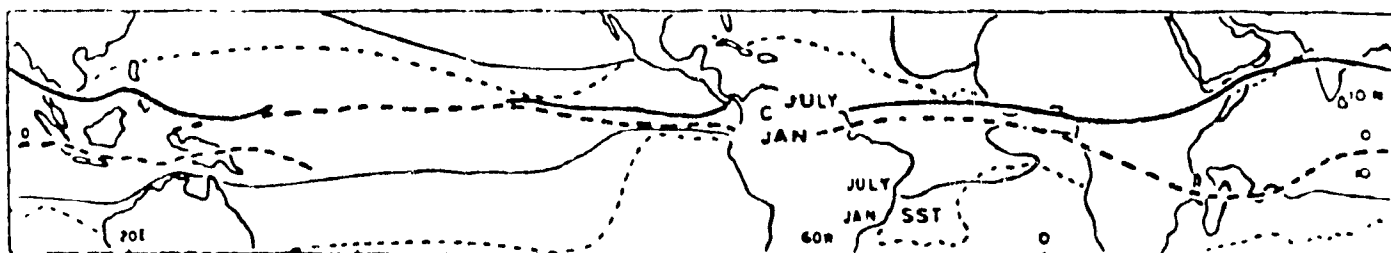


Fig 4 24 b) 25°C isotherm of sea surface temperature (thin lines) for January (broken) and July (solid) [and major cloud bands (heavy lines)] (taken from Hastenrath, 1980)

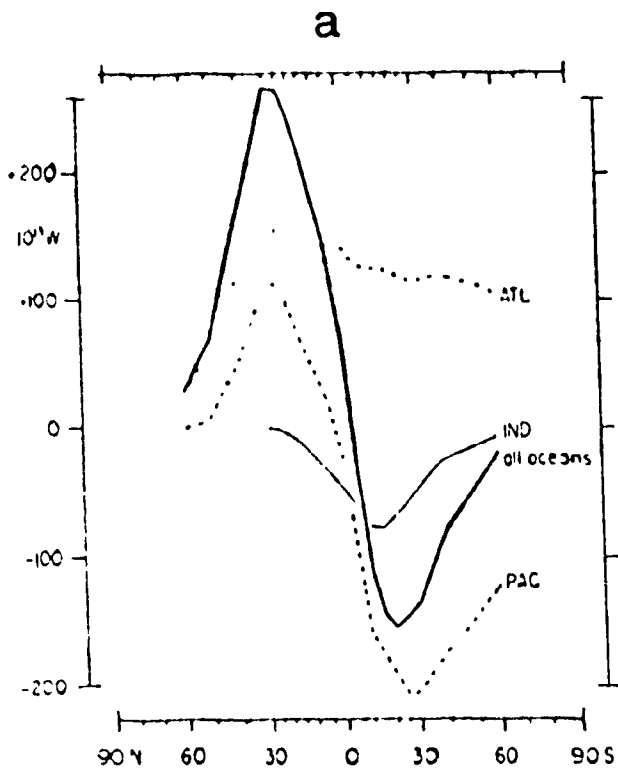


FIG. 4. Annual mean meridional heat transport within the oceans: Pacific broken, Atlantic dash-dotted, Indian Ocean thin solid, and all oceans combined heavy solid line. No. wind transport positive units in 10^{13} W [sources: Fig. 6 and Table 2 for 30° N- 30° S, Budyko (1973) for 30° - 66° N, and 30° - 60° S, and A. Wood and Greisman (1975) for 66° - 90° N].

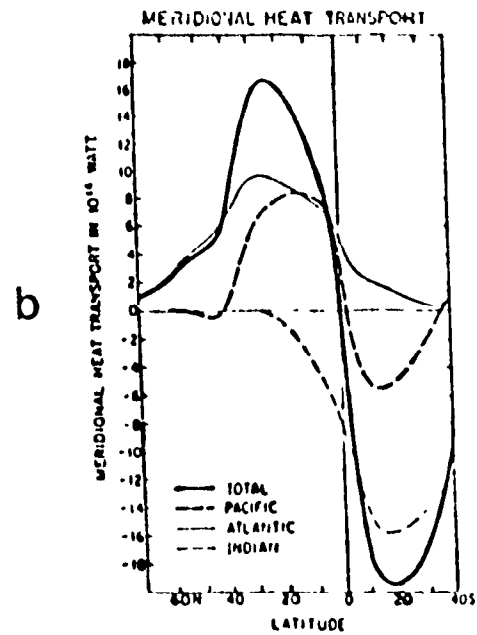


FIG. 3. The meridional heat transport for each of the three oceans and for all oceans combined. Positive value indicates a northward transport.

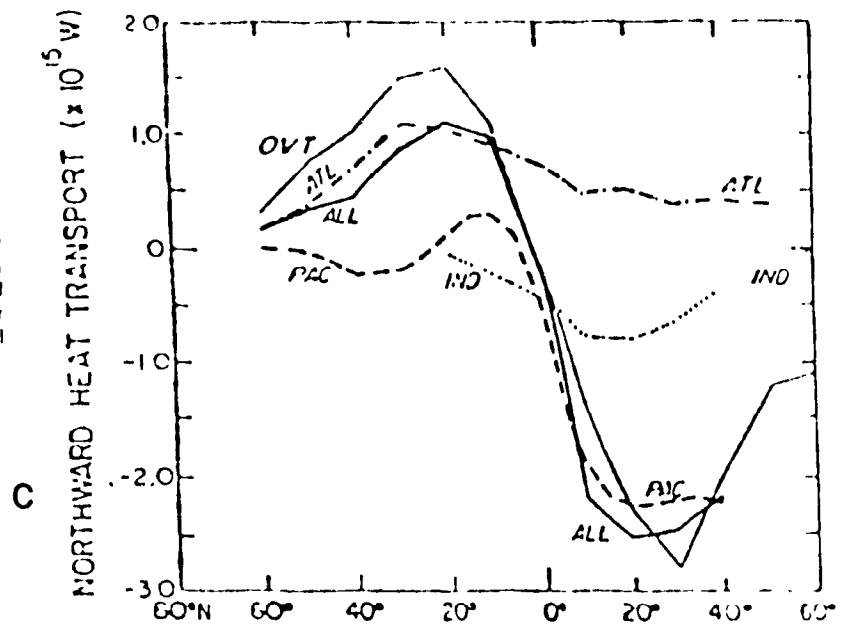


FIG. 3. Annual mean meridional heat transported by all ocean all based on surface heat fluxes calculated using Bunker's method. The Atlantic Ocean heat fluxes were calculated by Hall and Bryden (1982). Oort and Vonder Haar's (1976) and Trenberth's (1979) ocean heat transports for the Northern and Southern Hemisphere, respectively, are shown for comparison (OVT).

Fig 4.25. Annual mean meridional heat transports by the Indian, Atlantic and Pacific Oceans a) in 10^{13} W from Hastenrath (1980) b) in 10^{14} W from Hsiung (1985) and c) in 10^{15} W from Talley (1984).

the ocean. We see that the model transport in the Leeuwin run has the correct magnitude, the correct shape and even peaks at the right latitude.

We do not compare the Peru transport to real data because the Peru run does not represent a real ocean. Furthermore, the curve of heat transport at 3200 days (Fig.4.26) shows that the barotropic eddies are contributing quite strongly to the meridional advection. The curve has the same general shape as at 3000 days but a northward bias has been added. The Leeuwin heat transport is more stable.

The model is not in a state of climatic equilibrium, which would require integration for thousands of years. This would be inappropriate with this model: the solution would in fact become meaningless as will become clear from what follows. After 3000 days, the deep water in the Indian Ocean is warmer than the deep water in the Pacific Ocean in both runs, because the net Haney surface heat exchange is warming the whole ocean by downward diffusion. In our experiment, there is no possibility of cold deep water formation, as we have excluded the high latitudes and no provision is made for salinity forcing at the surface. The only communication with the deep ocean is via the vigorous barotropic eddies in the western region: in the baroclinic overturning streamfunction, the ocean is almost undisturbed below the first kilometre, except for a deep vertical cell between the equator and about 20°S. The cell appears stronger in the Leeuwin run, but only because in the more developed eddies of the Peru run, there is more perfect cancellation in a zonal average.

A measure of the equilibrium achieved is the difference between the net surface heat flux integrated over the Indian Ocean basin and the net export of heat to the Pacific through the Indonesian passage (see Table 4). The heat transport from the Indian to the Pacific is again the sum of the advective and diffusive components:

$$(23) \quad F_{I-P} = \rho_0 C_p \int_{\phi_s}^{\phi_n} \int_{-H}^0 \{ uT - A_{TH} (\text{acos}\phi)^{-1} T_x \} dz d\phi$$

The numbers given in Table 4 confirm that the advection term dominates the heat budget. The Leeuwin Indian Ocean is importing heat from the Pacific reservoir while the fast surface currents into

Day=3200

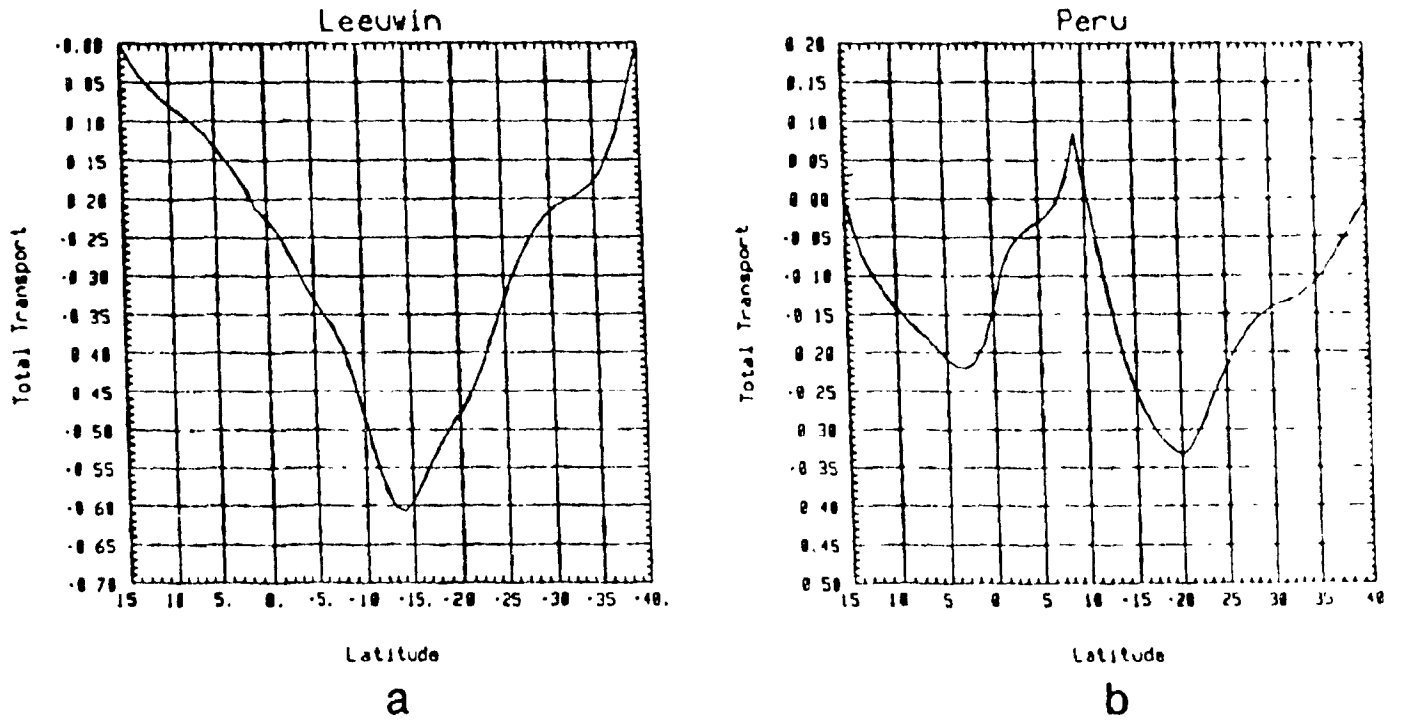


Fig.4 26. Northward heat transport (total transport) in 10^{15} W for a) the Leeuwin run b) the Peru run at 3200 days

TABLE 4				
Heat Budgets				
	This model		Model of G-W	
	Leeuwin run 3000 days	Peru run 3000 days	Leeuwin run 1500 days	Peru run 1000 days
Heat transport from Indian to Pacific in 10^{15} W				
i) by advection	-0 092	+0 513	-0 079	+0 183
ii) by diffusion	-0 001	-0 002	+0 0004	+0 002
iii) total	-0 091	+0 515	-0 079	+0 183
Total surface heating of the Indian Ocean in 10^{15} W	0 291	0 785	-0 050	0 195
Mean surface heat flux into the Indian Ocean in W, m ⁻²	6 43	17 33	-3 07	11 86
Mean departure from Haney temperature in °C	-0 179	-0 481	+0 085	-0 329
Mass exchanged between Pacific and Indian Oceans in Sv	3 5	7 7	6 6	7 1
Mean temperature difference of the exchanged waters in °C	6 5	16 7	3 0	6 5

the Pacific in the Peru run are exporting heat. In neither run does the transport through the gap balance the surface heating but the Peru run is closer to equilibrium. (This was also the case for G-W who found the cause to be the generation of internal Rossby waves by the deepening thermocline near the eastern boundary in the Leeuwin run. The temperature signal is then radiated across the basin, increasing the adjustment time.) The Indian Ocean is still being heated in both runs, the mean surface heat flux over the area of the basin is 6.43 W/m^2 in the Leeuwin run, and nearly three times as much in the Peru run. However, this represents only a small mean departure from the Haney apparent atmospheric temperature: less than 0.5°C even in the Peru run. As G-W found with their model, the purely thermohaline forcing is inducing mass fluxes in either direction through the gap comparable to the real Indonesian throughflow. The mean temperature difference of the exchanged water is calculated as:

$$(24) \quad \Delta T = \frac{(\text{heat transport through the gap } F_{I-P})}{\rho_0 C_p (\text{mass transport in either direction})}$$

4.4. Comparison with Godfrey and Weaver (1990)

In their model with no Sverdrup circulation, G-W obtain a much stronger throughflow into the Indian Ocean in their Leeuwin run, comparable in magnitude to the flow out of the ocean in their Peru run (Fig.4.27). The westward Leeuwin throughflow travels undiminished to their imaginary barrier at 84°E then turns south to form a fairly fast western boundary current. Opposite southern Australia, the surface flow turns again to form the eastward onshore flow. Warm water is thus advected all the way around the basin, producing significantly higher surface temperatures than in their Peru run.

A similar basinwide thermohaline circulation appears to exist in our model, with some differences. The throughflow in our Leeuwin run is very weak. Only in the difference field can we clearly see a westward jet, but we know from the pronounced difference in temperature between the South

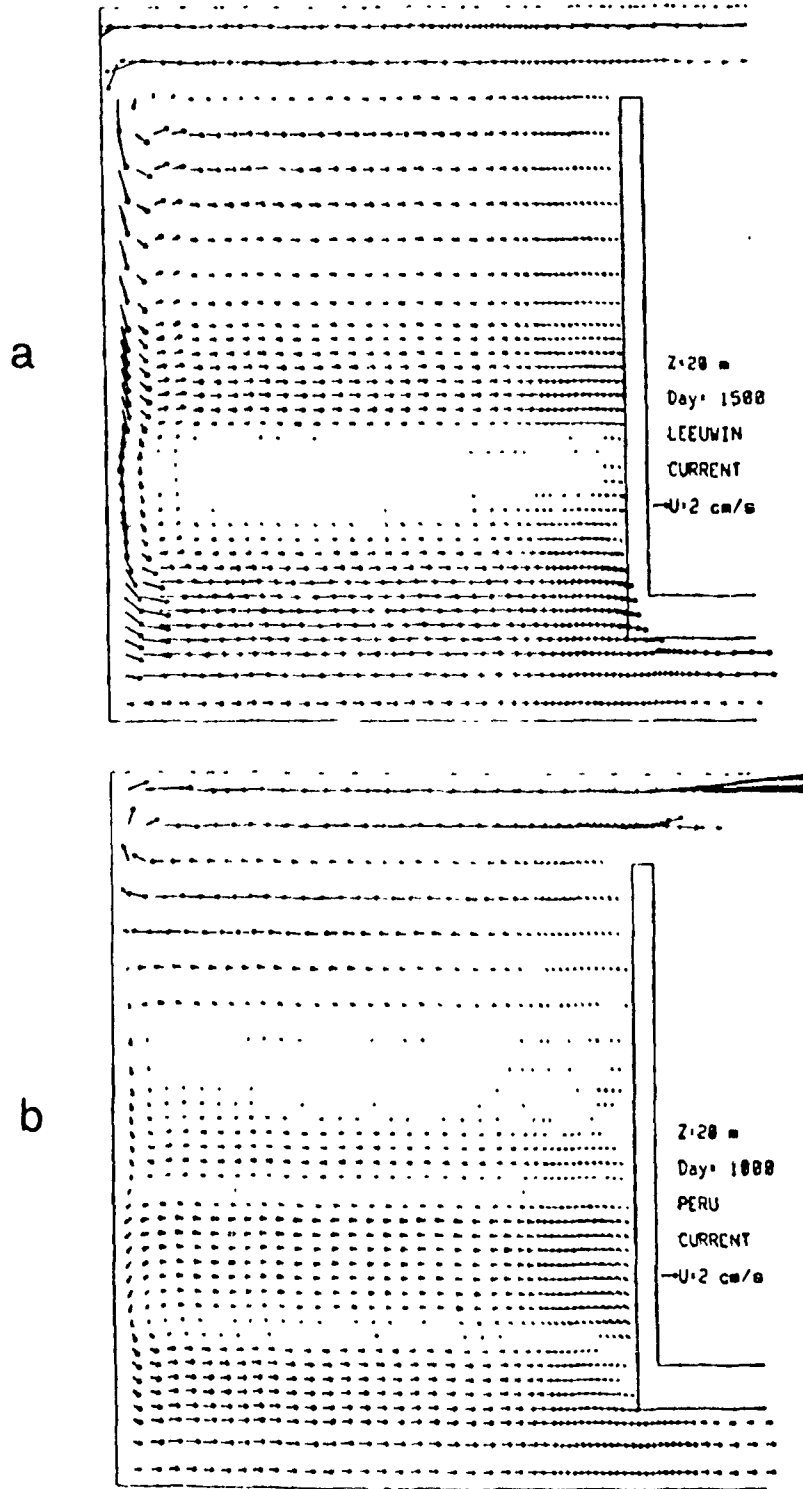


Fig 4 27. Horizontal velocities at $z=20\text{m}$ (level 1) from G-W: a) Leeuwin run b) Peru run.

Equatorial Currents of the two runs (Fig.4.18) that the Leeuwin throughflow is feeding into the SEC and that extra heat is being carried across to the western boundary. The wind-forced western boundary currents are slightly intensified opposite the Indonesian opening but locally only. The zonal onshore flow is certainly present but is more equatorially trapped (although it turns south as it approaches the coast). Nevertheless, the suggestion by G-W that heat introduced from the Pacific may be transported for long distances before being lost to the atmosphere is borne out by the results described herein.

We expect much larger surface heat fluxes in the present runs because the Haney condition constraining the surface isotherms to a zonal orientation is more easily violated in the presence of the fast wind-driven circulation. As in G-W, the southwest corner of the domain is distinctly warmer in the Leeuwin run. However, G-W find heat being released to the atmosphere along the western boundary by 5°S in their Leeuwin run (Fig 4 28), while our Indian Ocean is still being heated as far south as 17 or 18 °S (Fig.4.21). Their model also produces upward heat fluxes along the southern boundary in their Leeuwin run comparable to those along their western boundary. In our model too, the southern boundary is relatively warm (warmer than the Haney temperature at that latitude) but not to that degree. In both models though, the southern border is warmer in the Leeuwin run than in the Peru run.

The heat budget is primarily advective in both our model and the model of G-W (compare columns in Table 4). Approximately the same mass is exchanged between the Pacific and Indian Oceans in the Peru runs of both models and nearly the same amount is exchanged in their Leeuwin run. In our Leeuwin run, half as much mass travels either way through the gap because the sill prevents even a weak throughflow below 1200m. Nevertheless, the heat transport in our Leeuwin run is comparable to theirs because the surface currents are so much faster. In our Peru run, nearly three times more heat is exported to the Pacific than in their Peru run. The mean temperature difference of the exchanged waters is therefore much greater in our model.

Because their model included only the eastern boundary region and lacked the northern

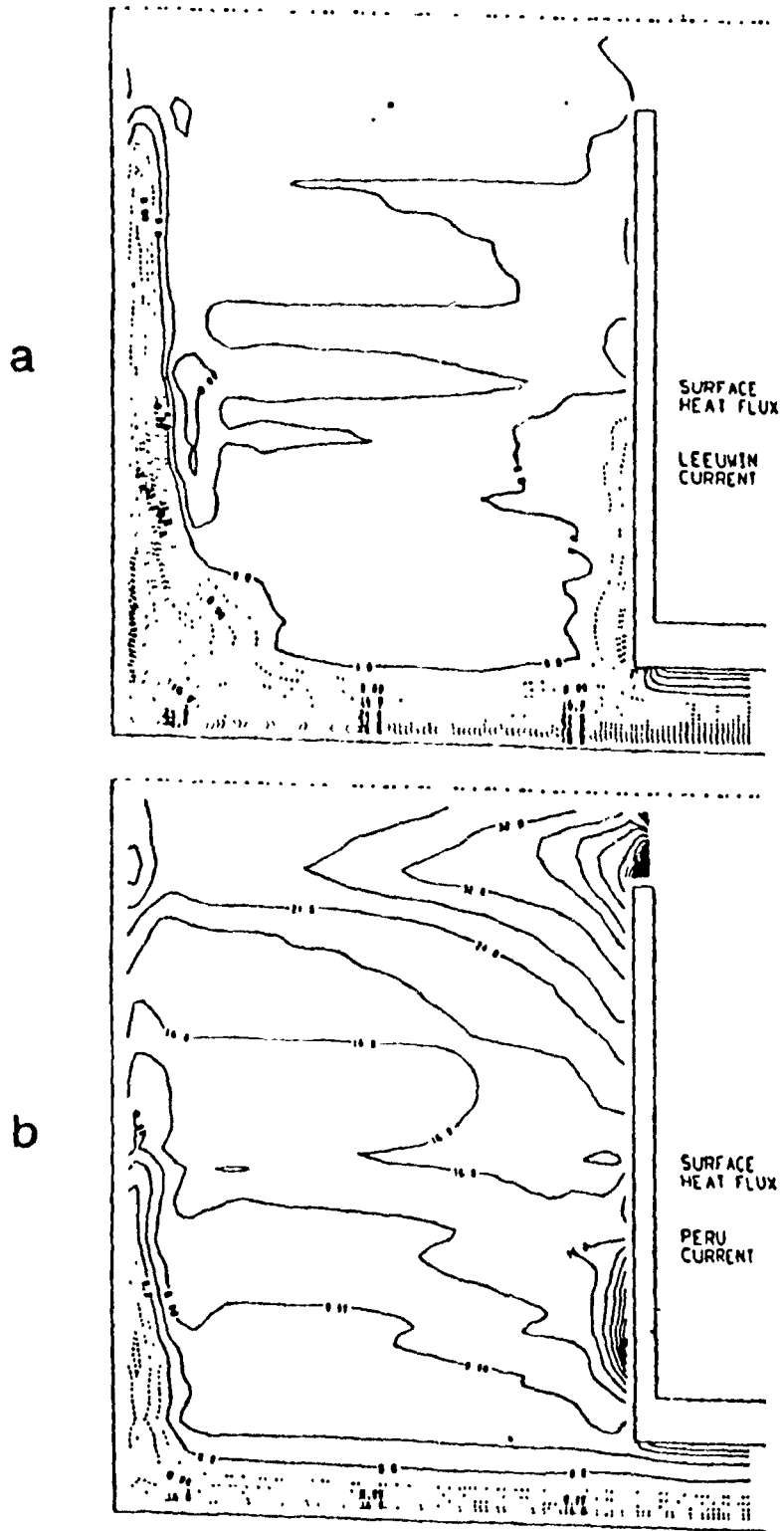


Fig 4 28. Surface heat fluxes in W/m^2 from G-W: a) Leeuwin run b) Peru run. The sign convention is opposite to Fig 4.23 so here solid contours indicate a heat flux into the ocean.

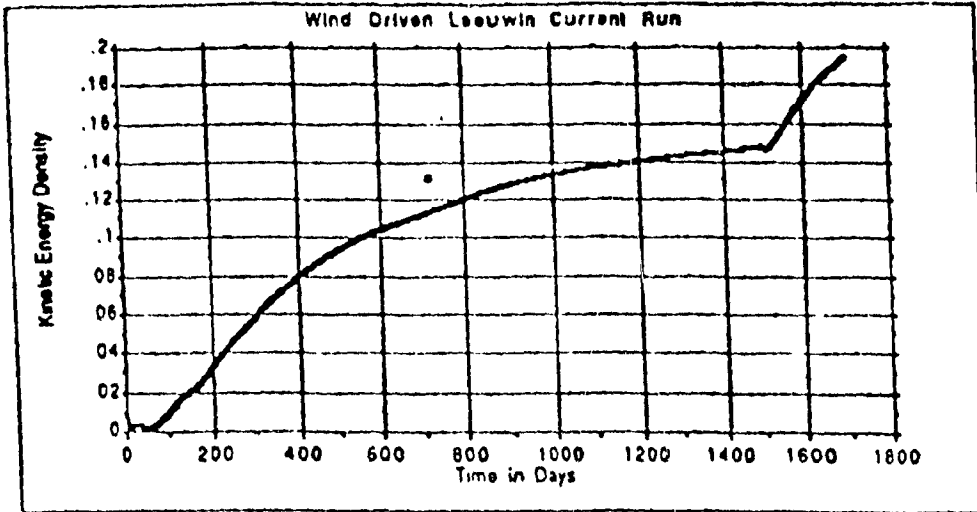
hemisphere (a region of heat gain), the heat flux integrated over the surface of their warm Leeuwin run is actually positive (out of the ocean). Our net heat flux is negative in both runs and is rather larger than theirs because of the larger surface area. The surface temperatures in our model are also slightly further from the Haney temperatures (on average) because of the more dynamic wind-driven circulation. Both their runs are closer to equilibrium, and their kinetic energy has reached a plateau after only about 1000 days (Fig. 4 29). (The later drop in their kinetic energy is because the model resolution was increased at that point.) Our kinetic energy has levelled out by 3000 days but superimposed on the mean is a fairly large amplitude oscillation due to the eddies in the western region.

4.5. Shear Instability in the Model South Equatorial Current

The wind stress curl that we have used produces currents that are reasonably representative of the real Indian Ocean. In the equatorial region, the westward current between roughly 14°S to 17°S is equivalent to the South Equatorial Current, and the eastward current immediately to the north is in the right location for the North Equatorial Countercurrent (during the southern hemisphere summer). The eastward flow north of the equator is more reminiscent of the winter conditions, when the eastward Monsoon Current appears.

The strong horizontal shear between these zonal currents is the cause of the fast eddies so prominent in the western quarter of the basin. The eddies are especially energetic in the Peru run where the surface currents are stronger and the internal deformation radius is larger (the temperature difference between the first two layers is greater). The scale of the eddies is around 1000 km in the Peru run and slightly less (about 850 km) in the Leeuwin run. They are clearly barotropic, and in the Peru run, they have a pronounced northwest-southeast tilt (Fig 4 20). Also, the meridional velocity associated with the instabilities is up to 15 cm/s at the surface in the Peru run, but less than one third of that in the Leeuwin run. However, from velocity plots at 3000 and 3200 days, the Leeuwin eddies

a



b

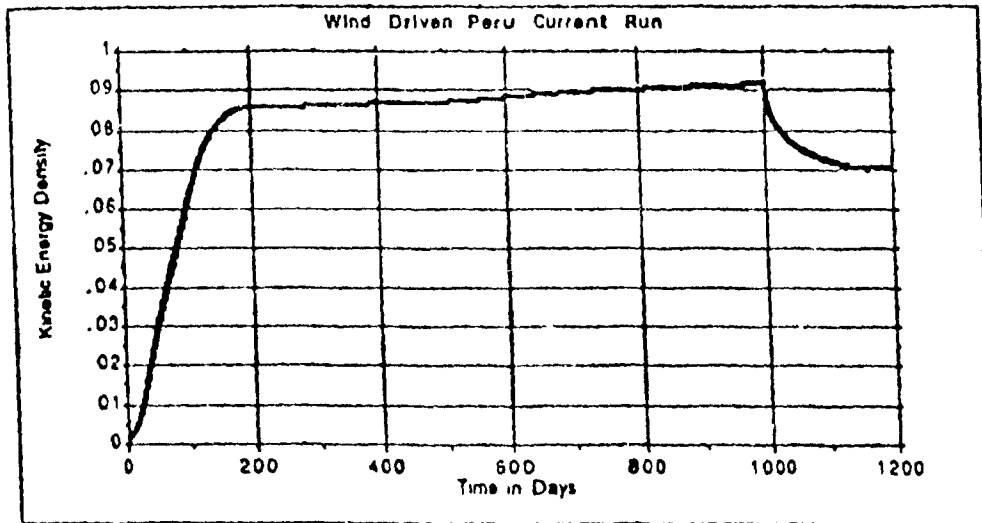


Fig 4.29. Kinetic energy density in $10^{-1} \text{ kg/m}^2 \text{ s}^2$ from G-W: a) Leeuwin run b) Peru run.

are still growing. The eddies appear to be the explanation for the kinetic energy oscillations (Fig 3.7) this would indicate a period just over a hundred days for the Leeuwin run and somewhat longer (150-200 days) in the Peru run (where nonlinear effects are occurring due to the large eddy velocities)

In linear theory, the necessary condition to determine if barotropic instability will occur in a steady zonal current with meridional shear only and bounded by a flat bottom and a rigid lid is the vanishing of the meridional gradient of the absolute vorticity ($\beta - U_{yy}$) along a latitude line (Leblond and Mysak, 1978). Here, the eddies are still accelerating, the perturbation amplitudes are not small and the current is neither zonally nor vertically uniform, nor horizontally non-divergent, so the test is not really applicable. However, it is certainly true that the absolute vorticity has a number of zero crossings both in the region where eddies are observed and away from it.

The suggested mechanism for the generation of the eddies is given further credibility by the previous occurrence of barotropic instability in both observations and models of equatorial zonal currents and the western Indian Ocean. Kindle and Thompson (1989) list the evidence for 20- to 30-day period oscillations of wavelength 800-1600 km in the equatorial waveguides of all three tropical oceans. Shear instability between the SEC and the SAC was found to be the cause of the near-equatorial oscillations in the Atlantic and Pacific Oceans (Philander, 1978 and Cox, 1980) and Kindle and Thompson (1989) successfully modelled similar 26-day waves in the western Indian Ocean, although they suggest a more complicated trigger associated with the seasonal migration of the southern gyre. Kindle and Thompson (1989) also noted energy in the 40- to 60-day period band between 3°S and 8°S, which in their model had to come from lateral shear in the westward flow. Mysak and Mertz (1984) first documented a 40- to 60-day oscillation in the source region of the Somali Current, but related it to fluctuations in the wind forcing. Quadfasel and Swallow (1986) followed their example in interpreting a 50-day wave measured in the Indian Ocean in 1975 in the SEC, and Moore and McCreary (1990) recently produced current oscillations whose amplitude were comparable to observations using a linear model forced by a wind field oscillating with a 60-day period. However, Schott et al. (1988), who measured substantial boundary current fluctuations east of Madagascar near

12°S in the 40- to 55-day period band, could not relate these to the observed winds. They also found that in their model driven by mean monthly winds, the area between Madagascar and the equator was characterized by intense eddy activity (although on longer time-scales (70-80 days) than observed). Similarly, the simulation by Woodberry et al. (1989), driven by the same climatological monthly mean winds, also features 40- to 50-day oscillations in the western region, which must again be attributed to barotropic instability.

While we shall not support this with more evidence, we note the possible role of the Seychelles-Mauritius ridge at 60°E, and Madagascar to the west of it, in braking the acceleration of the zonal wind-driven currents in the Indian Ocean.

For the purposes of this study, the effect of the eddy circulation on mass and heat transport is of more importance than the dynamics of the generation and maintenance of the unstable regime. We mentioned in Section 4.3 the large variability of the meridional heat transport due to the eddies in the Peru run. The apparent deep overturning cell in the streamfunction of the Peru run also changes radically between 3000 (Fig.4.4) and 3200 days (Fig.4.30). In the individual eddies, very large changes also occur in the local surface heat flux, although adjacent eddies undergo opposing changes. The presence of the eddies in the Peru run makes the comparison between the two runs more difficult and frustrates any interpretation of the heat transport. This was a strong motivation for the two new runs described in the next chapter.

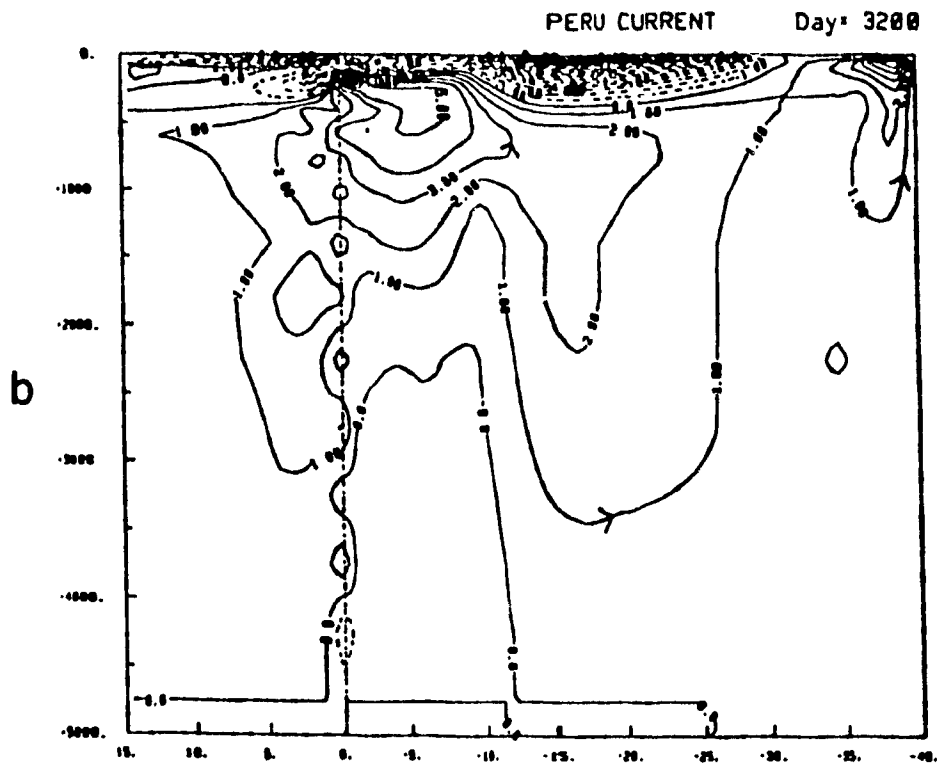
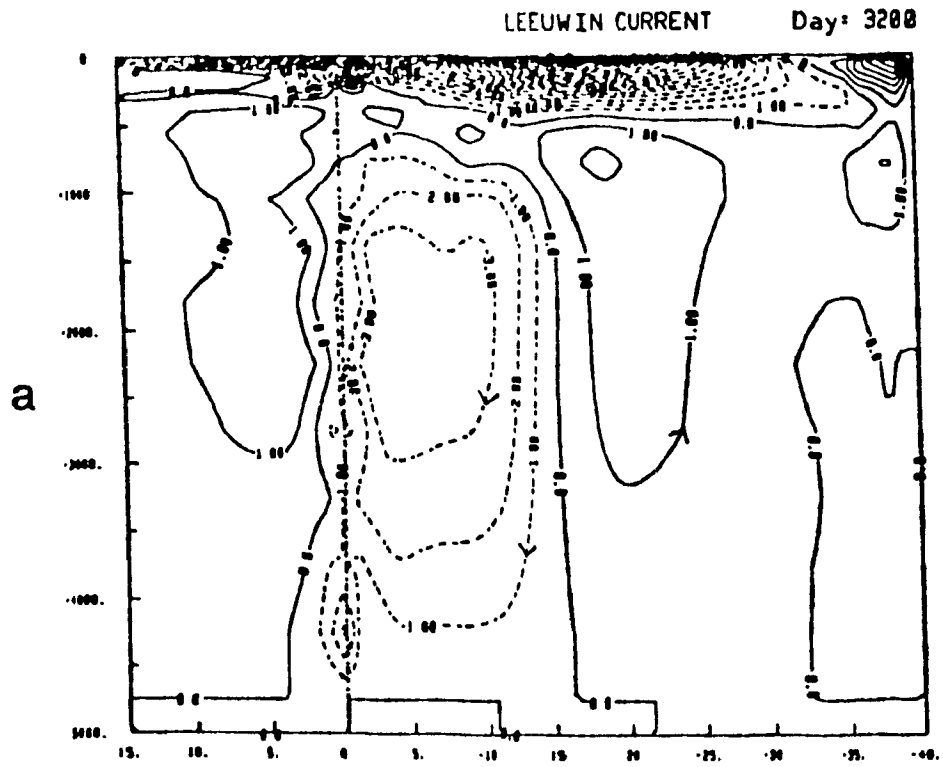


Fig.4.30. Overturning (zonally-integrated) streamfunction in Sv as a function of latitude for a) the Leeuwin run b) the Peru run at 3200 days.

5. LIMITATIONS OF THE MODEL AND FURTHER EXPERIMENTS

5.1. Difficulties with the first two runs

The finite difference approximation of the continuous flow carries with it some risks, and the equator is particularly subject to numerical problems. Spurious equatorial cells appear in the overturning streamfunction (Fig.4.4). These are associated with the checkerboard pattern of meridional velocity seen in the vertical section at 0°N (Fig 5.1) although this may also be due to transient waves propagating along the equator (see also Fig 5.2). Pools of upwelling and downwelling are produced along the equator (Fig.5.3) Weaver and Sarachik (1990) were able to eliminate such cells by increasing the vertical resolution, however the large number of levels used in this model is already computationally demanding. The spurious cells would affect the meridional heat transport in longer term climate models but over a short integration of only 3000 days, local effects only are expected.

A more serious numerical flaw is the small patch of positive surface heat flux on the equator against the eastern boundary (Fig.4.21). This requires a surface temperature greater than the local Haney temperature of 29°C (as is observed in Fig.4.3), which is both the highest value possible in the apparent atmosphere, and the highest temperature in the vertical profile to which the Pacific Ocean of the Leeuwin run is restored (the Peru Pacific is even cooler). A temperature greater than 29°C cannot therefore be accounted for physically. Yin and Fung (1990) have shown that in the Bryan-Cox model a non-uniform spacing of the vertical levels and a low vertical diffusivity may, in a region of strong downwelling, produce a negative effective vertical diffusivity. That is, we are witnessing negative diffusion, or heat passing from cooler water to warmer water. Associated with this are unrealistic temperature jumps between adjacent vertical levels: in the zonal-vertical section of temperature at 5°N (Fig.5.4), the isotherms diverge noticeably near the eastern boundary. (The

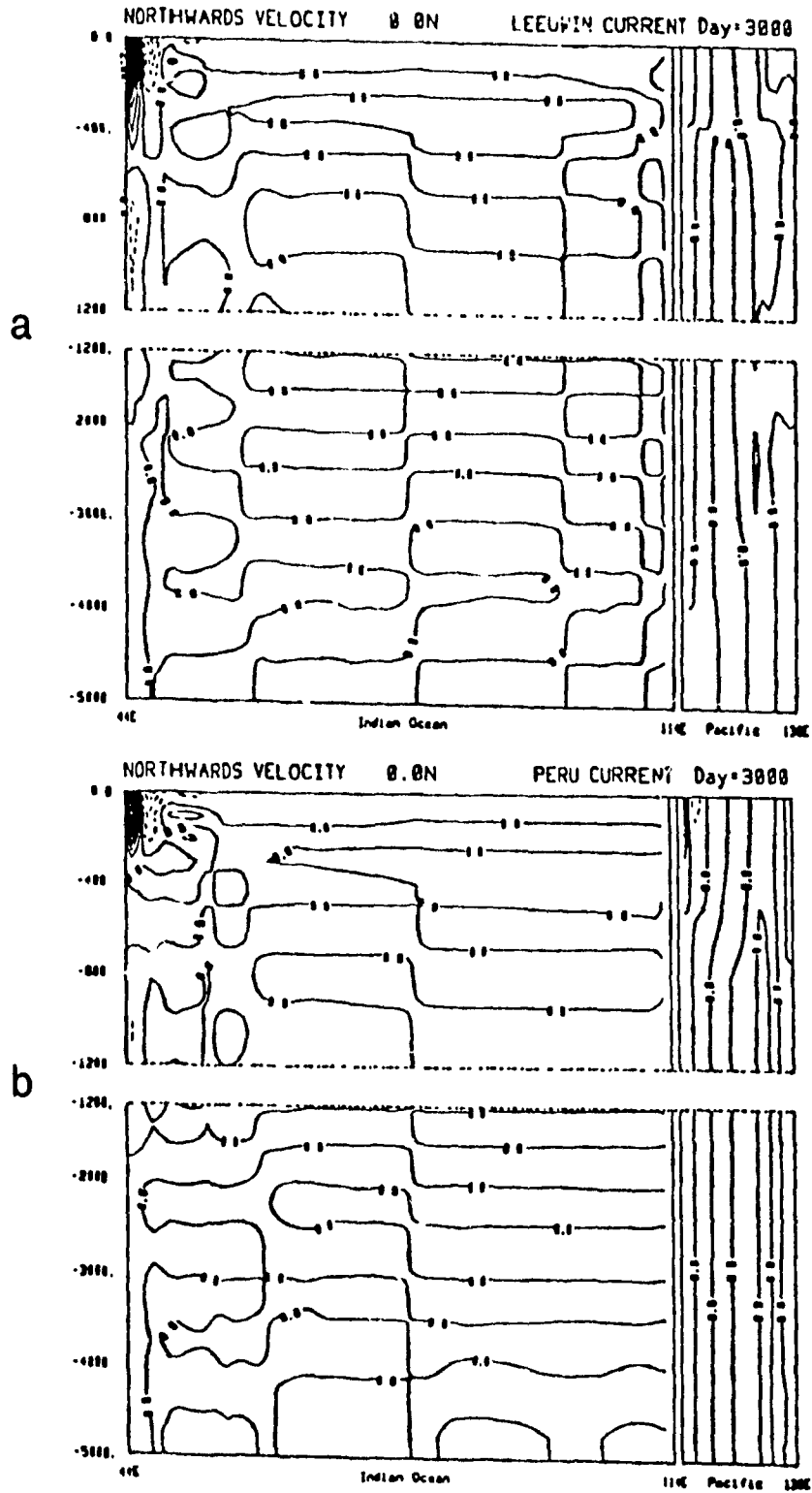
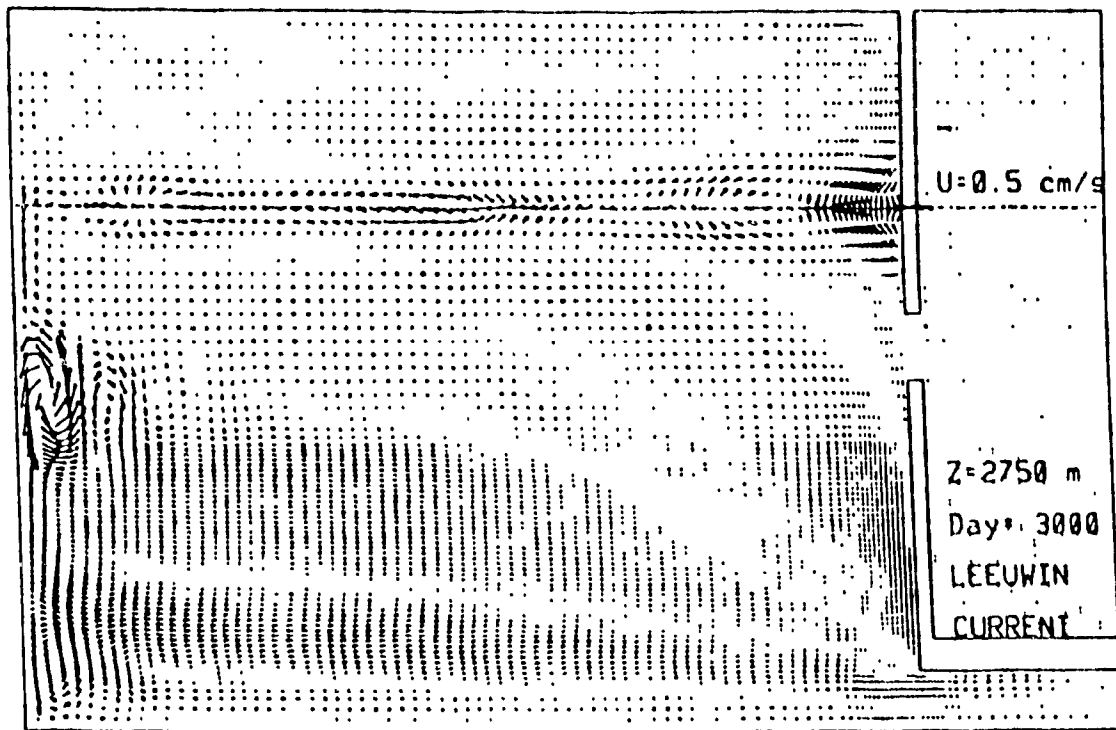
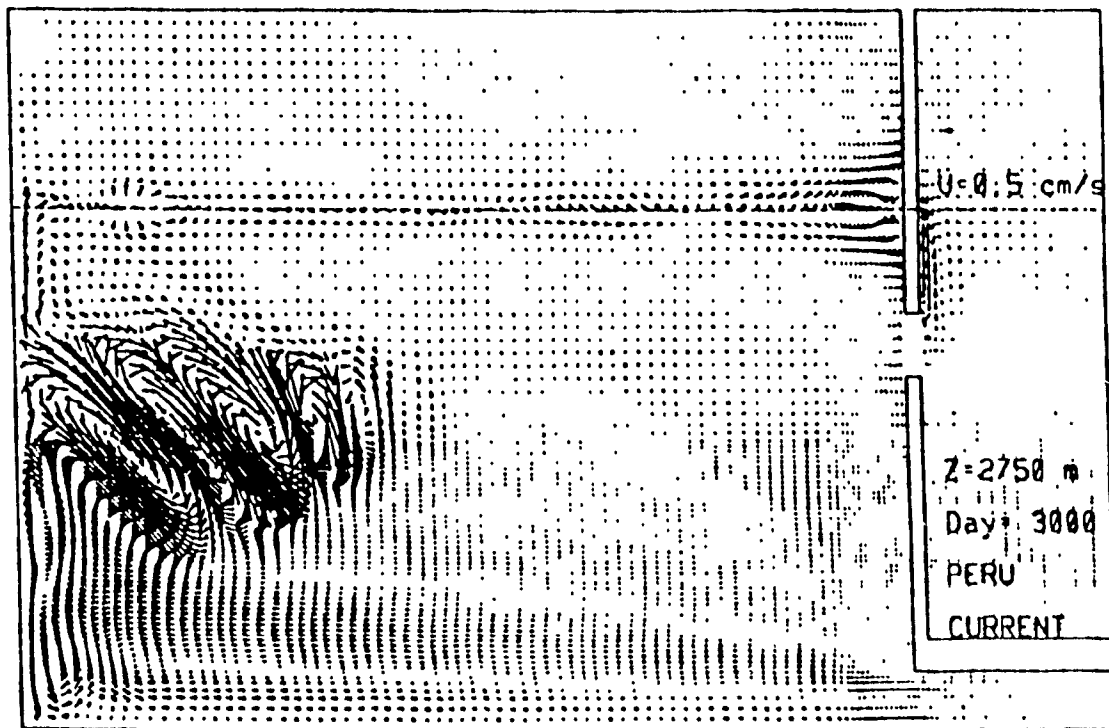


Fig 5.1. Zonal-vertical section of northward velocity at 0.0°N: a) Leeuwin run b) Peru run.

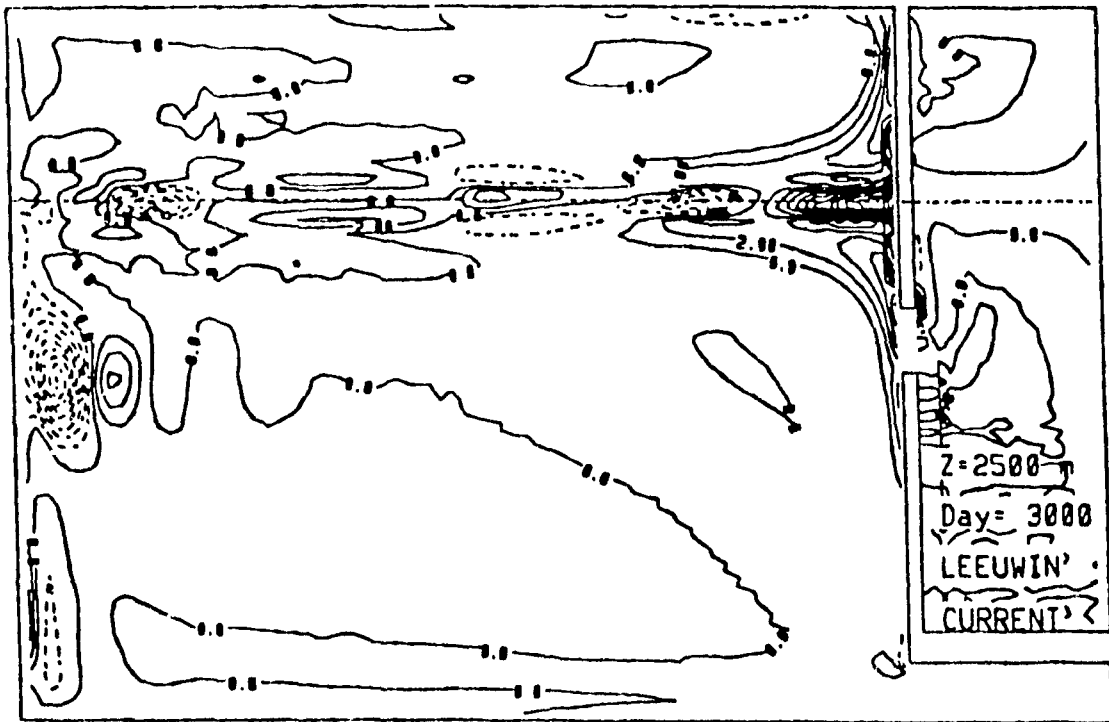


a

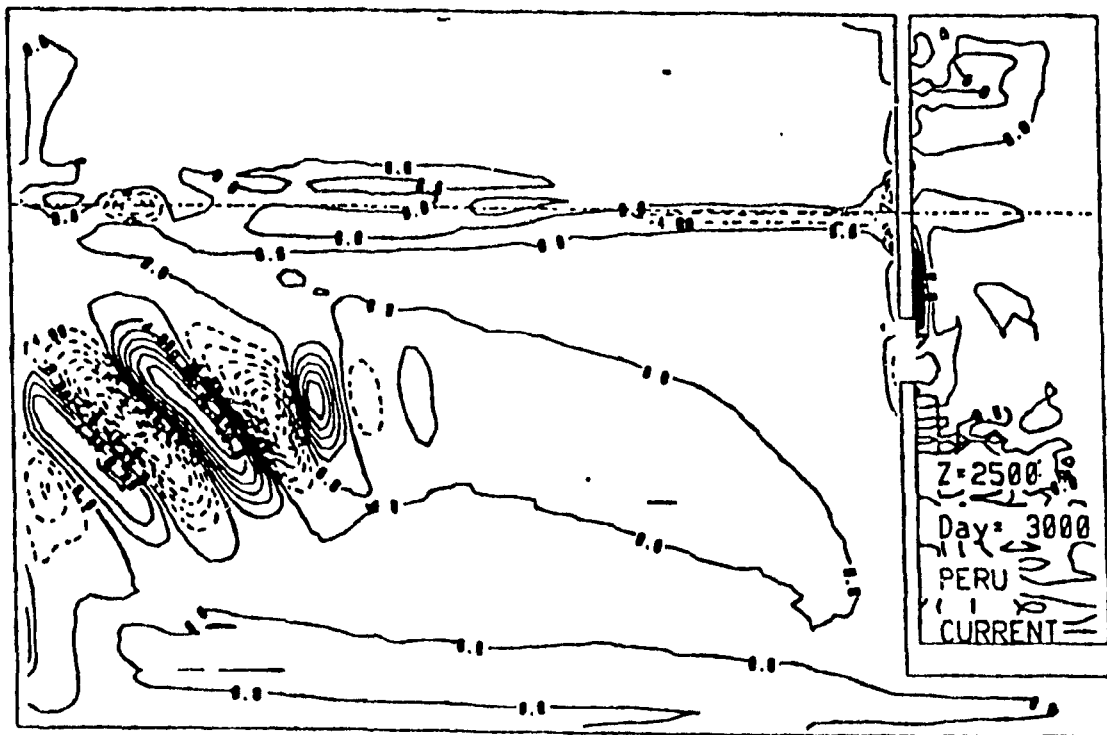


b

Fig.5.2. Horizontal velocities at $z=2750\text{m}$ (level 13) a) Leeuwin run b) Peru run.



a



b

Fig.5.3. Vertical velocities in 10^{-4} cm²/s at z=2500m (interface 12) a) Leeuwin run
 b) Peru run. Solid contours indicate upwelling and dashed contours
 downwelling.

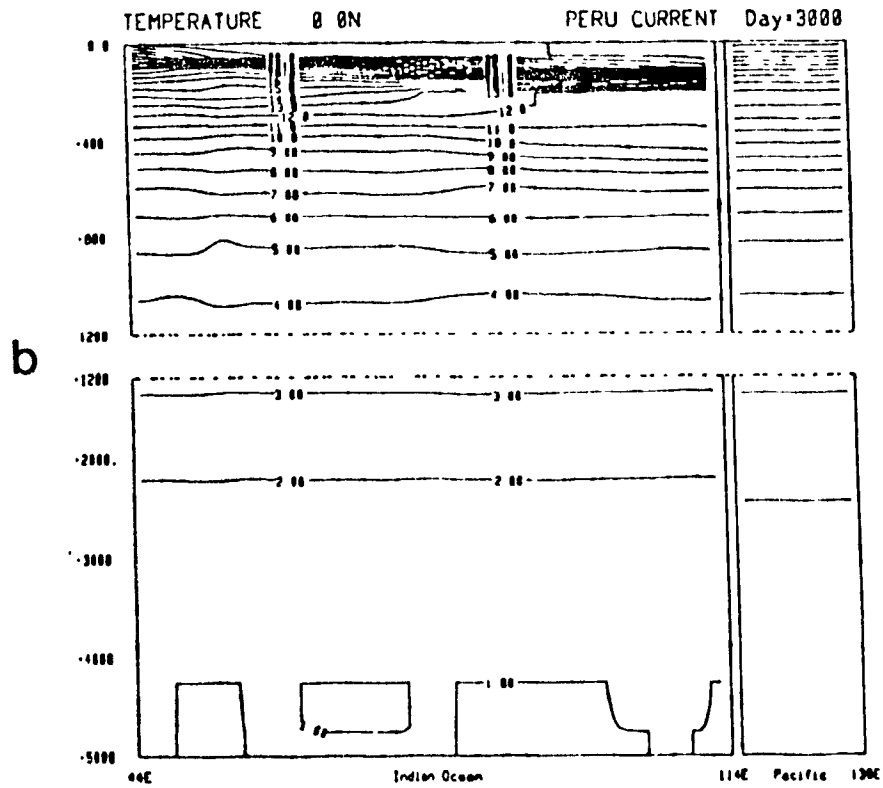
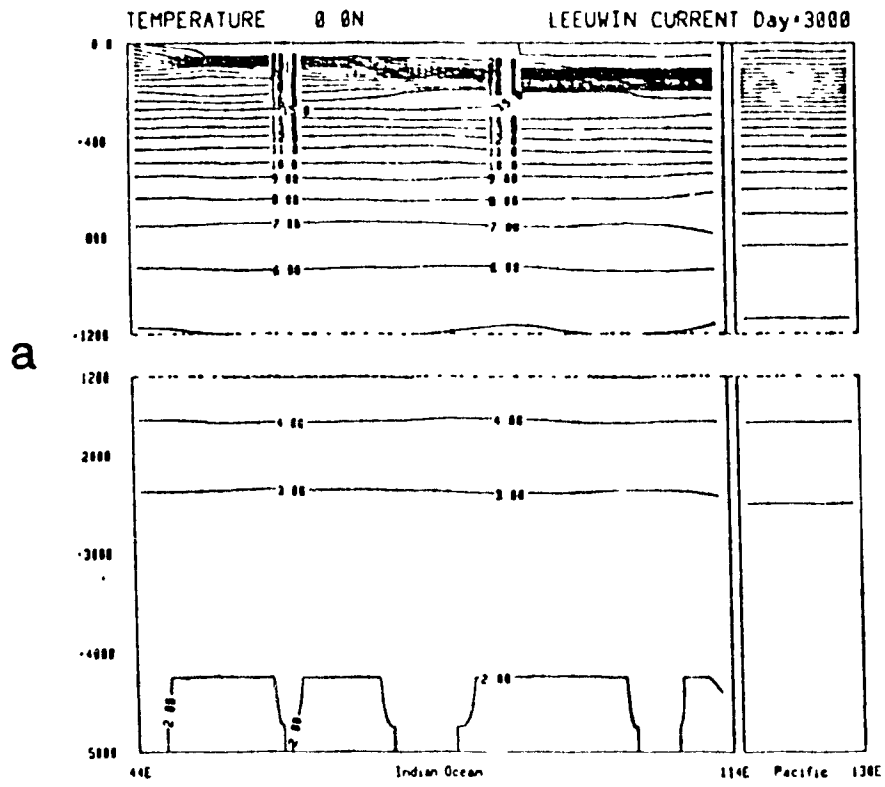


Fig.5.4. Zonal-vertical section of temperature (in °C) at 0°N: a) Leeuwin run b) Peru run.

problem is occurring only at the eastern boundary because of the strong downwelling there forced by the eastward wind on the equator driving water towards the coast)

To resolve the above problems, it was decided to carry out another Peru run with increased vertical viscosity. the value of A_{TV} in the Peru-2 run is twenty times higher (see Table 3). The very low vertical diffusivity at the surface has also been changed: A_{TV} is now $1.0 \text{ cm}^2/\text{s}$ at all depths. The reasoning behind this was first to overcome the numerical deficiencies just described, but also, by allowing more energy to be dissipated in sub-grid scale processes, to avoid the large-scale wave-type phenomena otherwise produced by barotropic instability.

Another question may be raised in connection with the first runs: whether the different initial conditions (on temperature and salinity) in the two runs may not bias the final results. To speed up the convergence, the Indian Ocean of the Leeuwin run was initialised with the warm profile of the Leeuwin throughflow. This is justified if the warm throughflow is able in the long run to warm all corners of the model basin. To test this assumption, we performed another Leeuwin run in which the Pacific was restored throughout to the warm profile but the two basins were initialised with the cooler temperatures and higher salinities of the Peru runs. The increased vertical viscosity and diffusivity were also used in this run, again as a way of dealing with numerical shortcomings.

One defect of the model which we will not undertake to correct at this time is the weakness of the simulated Leeuwin Current. The eastern boundary regime produced by the warm throughflow is qualitatively correct. that is, we obtain a poleward surface current with an equatorward undercurrent, deep mixed layers and downwelling at the coast, and a positive surface heat flux everywhere along Australia. However, the current itself is much too slow. G-W list a number of reasons for this: the 0.4° resolution (of the same order as the radius of deformation) is too coarse to resolve the narrow Leeuwin Current and entail a larger A_{MH} (through equation 11) than is perhaps desirable there, the Haney condition at the surface tends to damp latitudinal temperature variations (and hence, through geostrophy, meridional velocities), there is no forcing of salinity at the surface (monsoon precipitation in the equatorial region and evaporation at high latitudes would otherwise enhance the steric height

gradient) and there is no topography, when the presence of the continental shelf is known to be important in trapping the coastal current, and in enhancing it through the JEBAR effect.

We emphasize again here that this is not a climate model in the true sense. The relatively short integration allows us to simplify the model in ways which preclude a true equilibrium. We have no exchange with the Antarctic therefore no source of cold water for the deep ocean. Over 3000 days, the deep layers are therefore warming up (this can be seen by comparing the Indian and Pacific basins in a zonal-vertical section such as at 0°N in Fig.5.4). We noted earlier that the heat budget was not balanced. The model has reached a quasi steady-state but it is not in diffusive equilibrium.

5.2. High Viscosity Experiments

As hoped, the increased viscosity and diffusivity improved the numerical problems and eliminated the barotropic instability in both runs. The spurious cells in the overturning streamfunction have been strongly damped (compare Figs. 5.5, 5.6 and 5.7 with Figs. 5.1, 5.2 and 5.3). The surface convergence onto the equator which was producing downwelling and deep mixed layers along 0°N has been much reduced (compare Figs. 5.8 and 5.9 with Figs. 4.2 and 4.3). The patch of surface water warmer than 29°C is still unfortunately present at the eastern boundary, but is now very much smaller (Fig.5.10 shows the zonal-vertical sections at 0°N for the Leeuwin-2 and Peru-2 runs - see Fig.5.4 for the same section for the Leeuwin and Peru runs) and the divergence of the isotherms at the eastern boundary has been much reduced. The thermocline is now much less compact because of the higher vertical diffusivity. From the temperature field at $z=60\text{m}$ (Fig 5.9), we see that the cool tropical gyre has been considerably weakened (the gyre centre is 5°C warmer in the new Peru run and perhaps 3.5°C warmer in the new Leeuwin run). The southern half of the basin has not changed much, nor has the northern hemisphere. The maps of surface heat fluxes for the new runs are similar to the previous ones (compare Figs 5.11 and 4.21) however the whole surface is cooler in both the

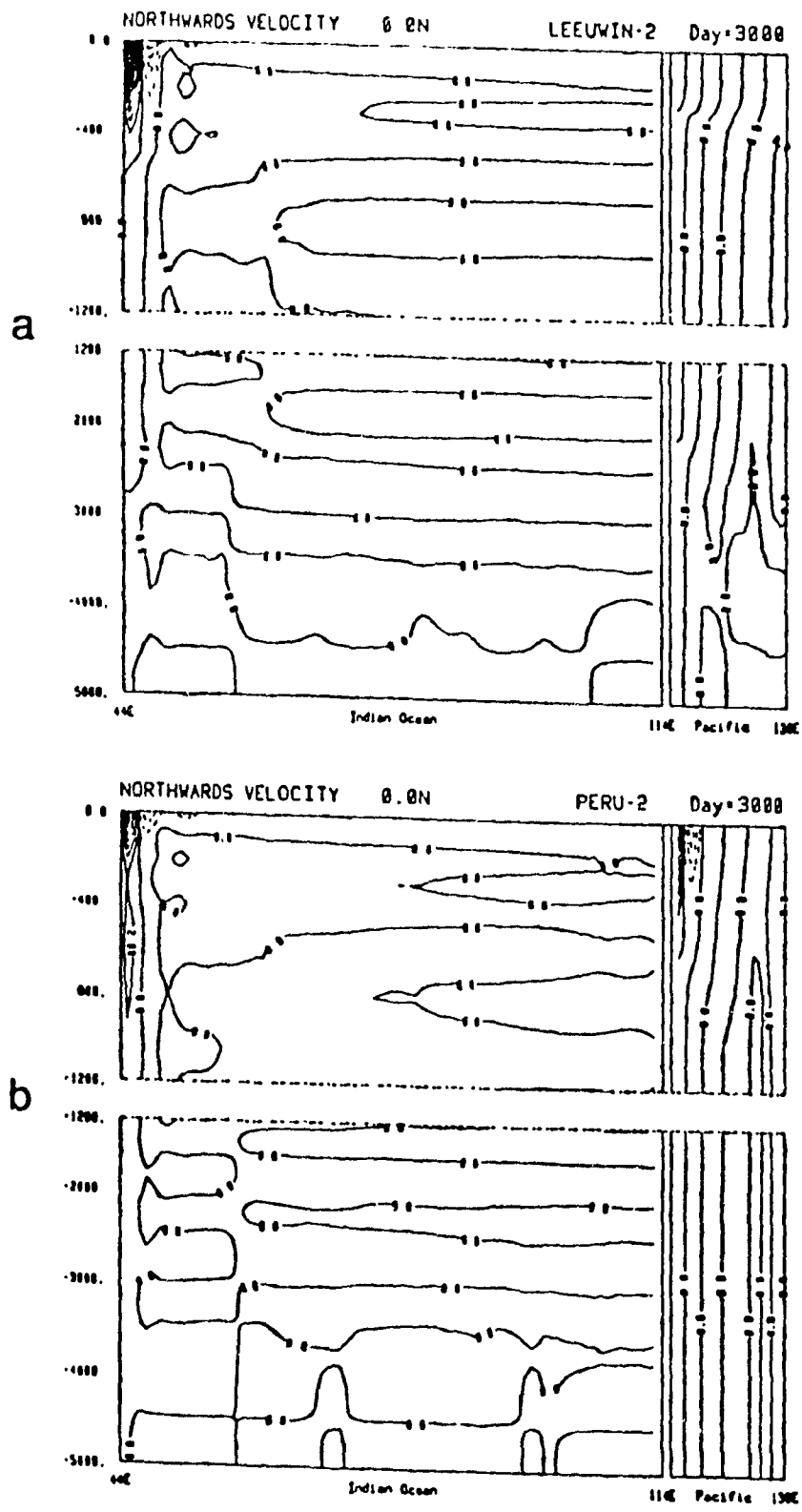


Fig 5.5. Zonal-vertical section of northward velocity at 0°N: a) Leeuwin-2 run
 b) Peru-2 run (cf. Fig. 5.1).

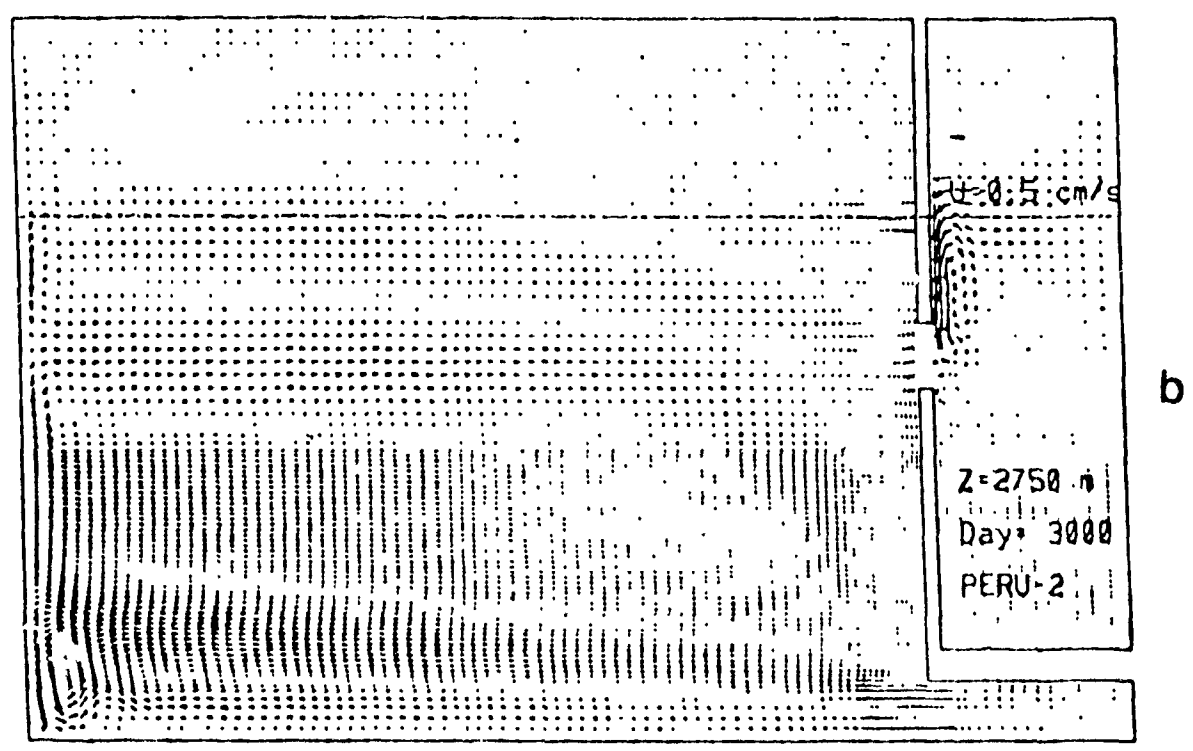
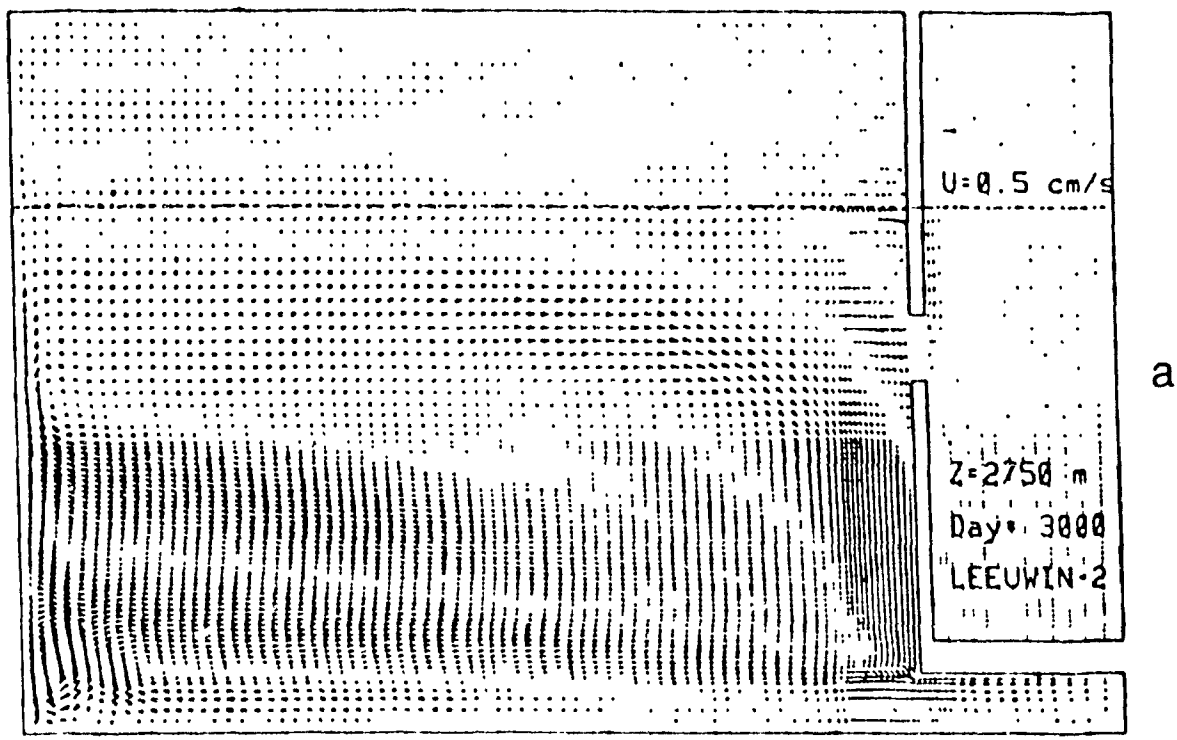
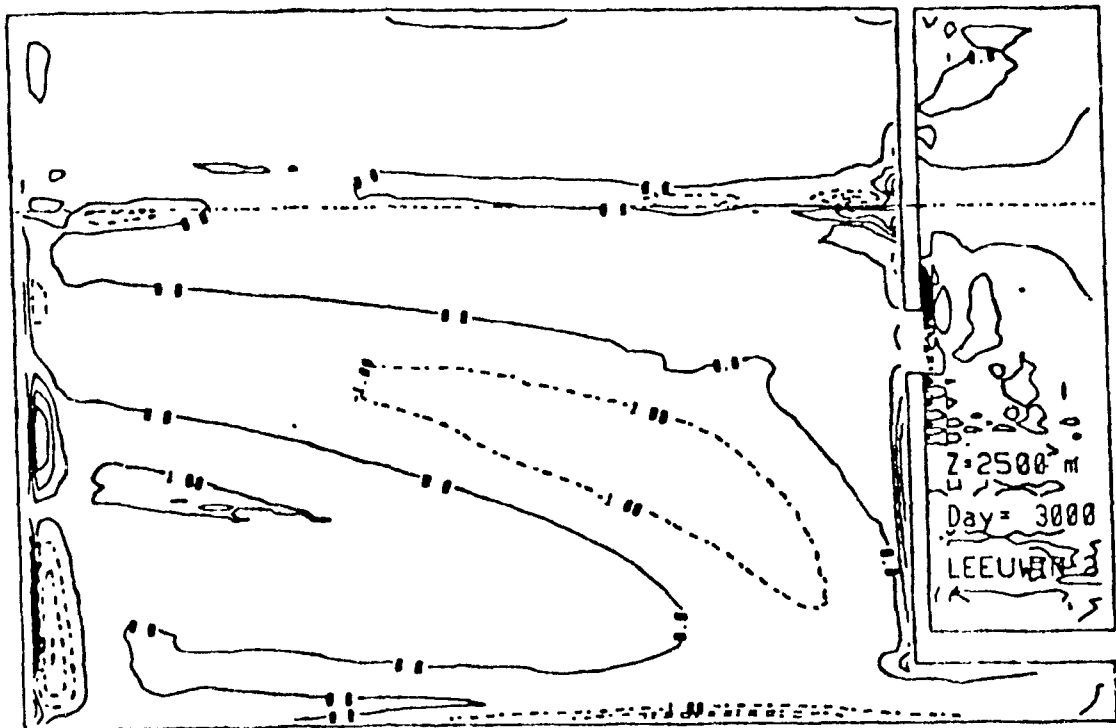
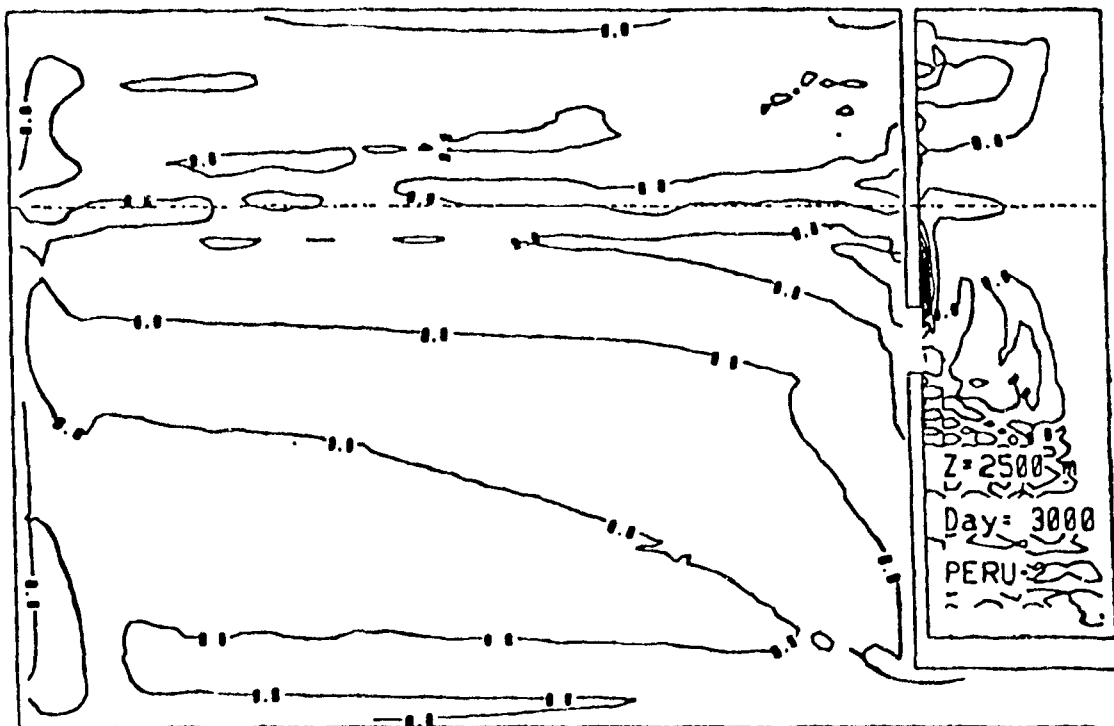


Fig.5.6. Horizontal velocities at z=2750m (level 13) a) Leeuwin-2 run b) Peru-2 run (cf Fig. 5.2)

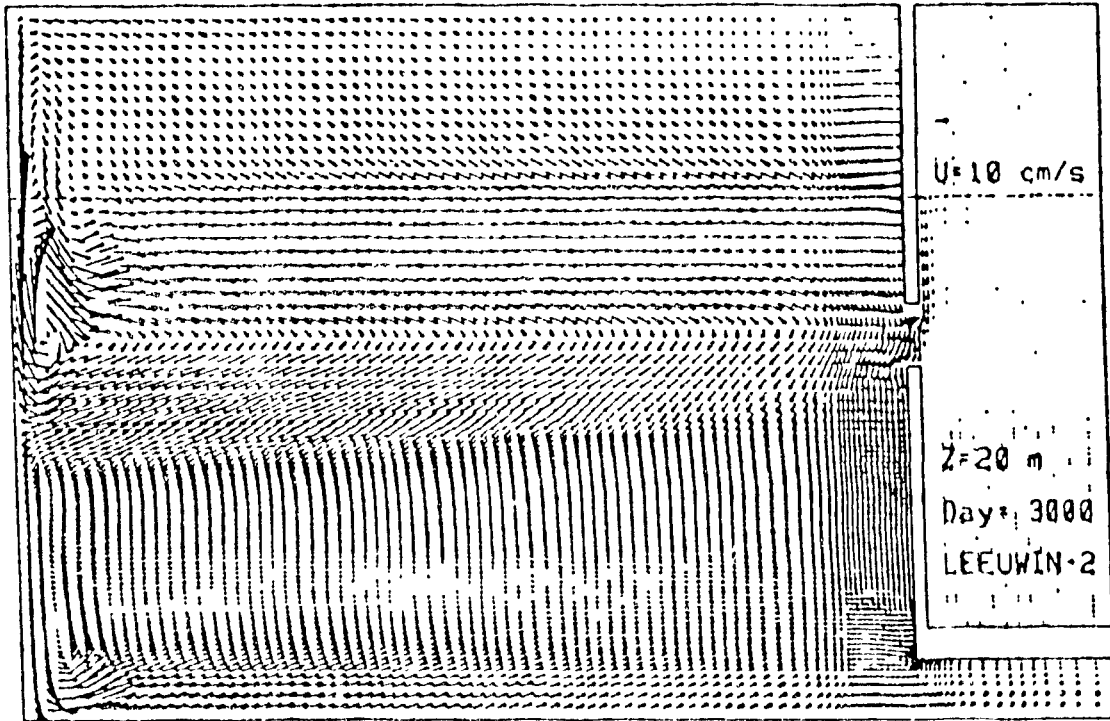


a

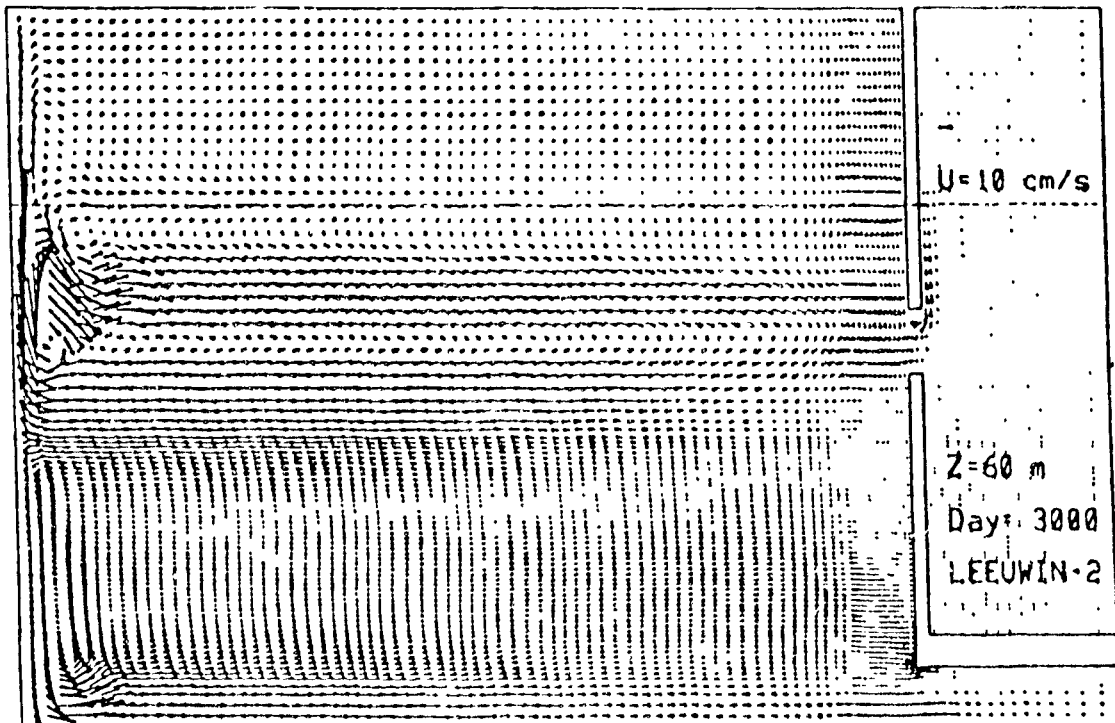


b

Fig.5.7. Vertical velocities in 10^{-4} cm^2/s at $z=2500\text{m}$ (interface 12) a) Leeuwin-2 run b) Peru-2 run. Solid contours indicate upwelling and dashed contours downwelling (cf Fig. 5.3).

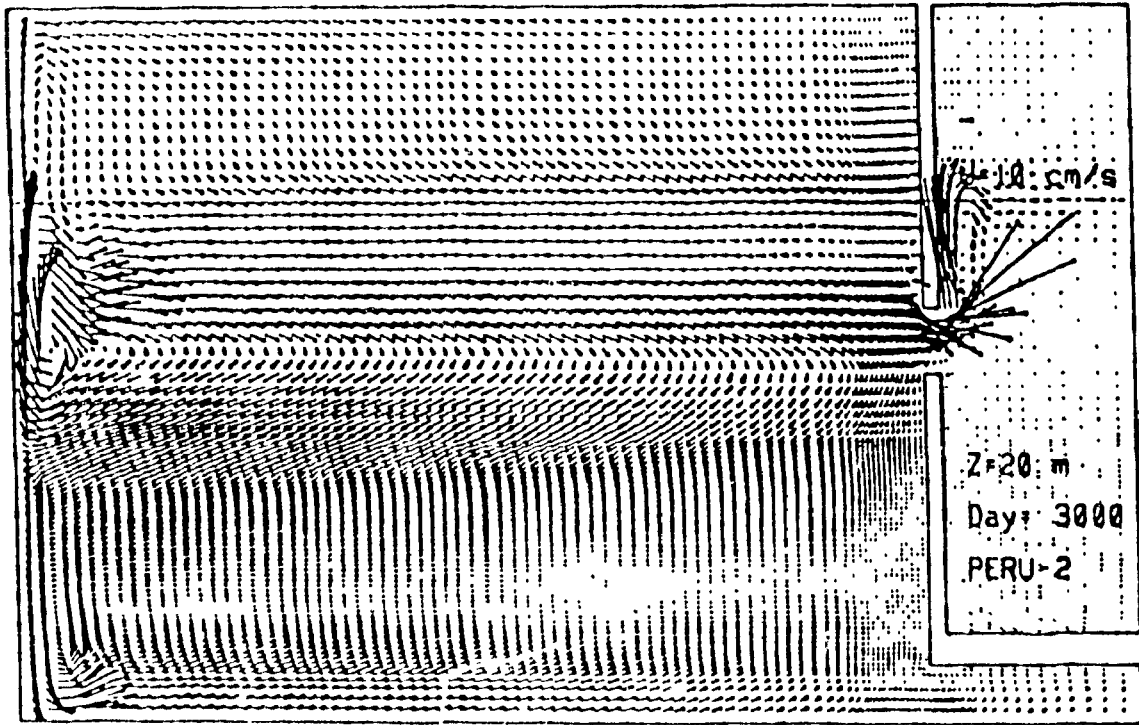


a

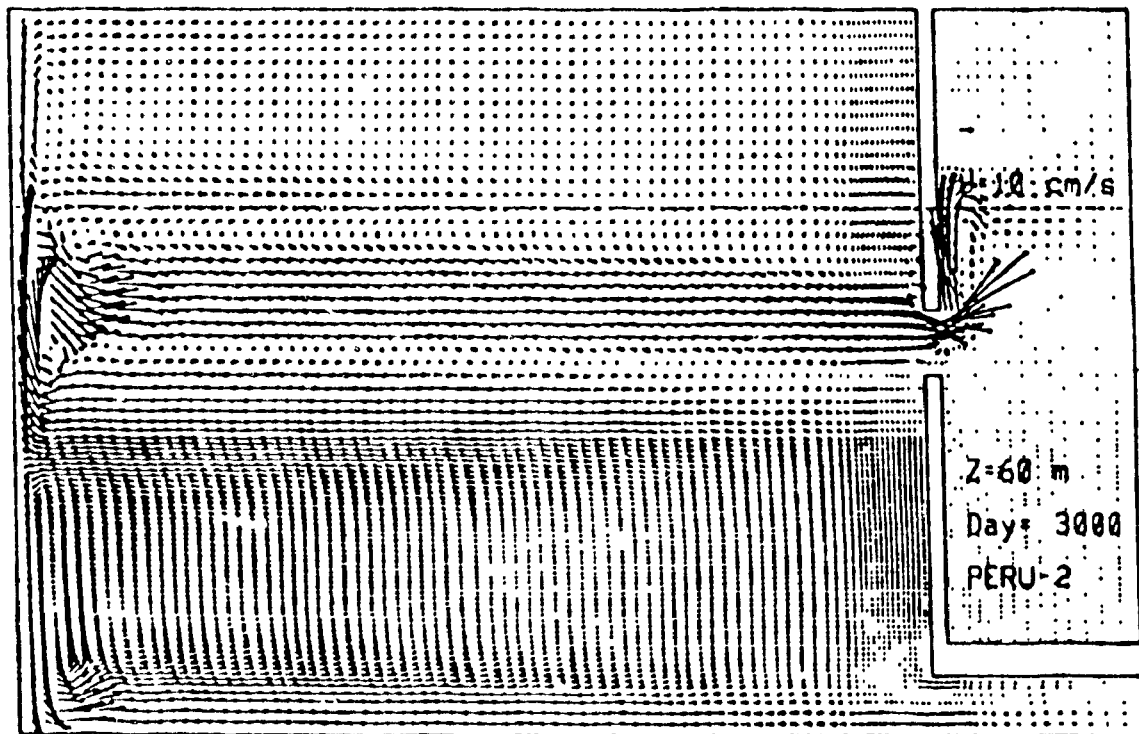


b

Fig 5 8. Horizontal velocities at $z=20\text{m}$ and $z=60\text{m}$ (levels 1 and 2) a) and b) Leeuwin-2 run c) and d) Peru-2 run (cf. Fig. 4 2).

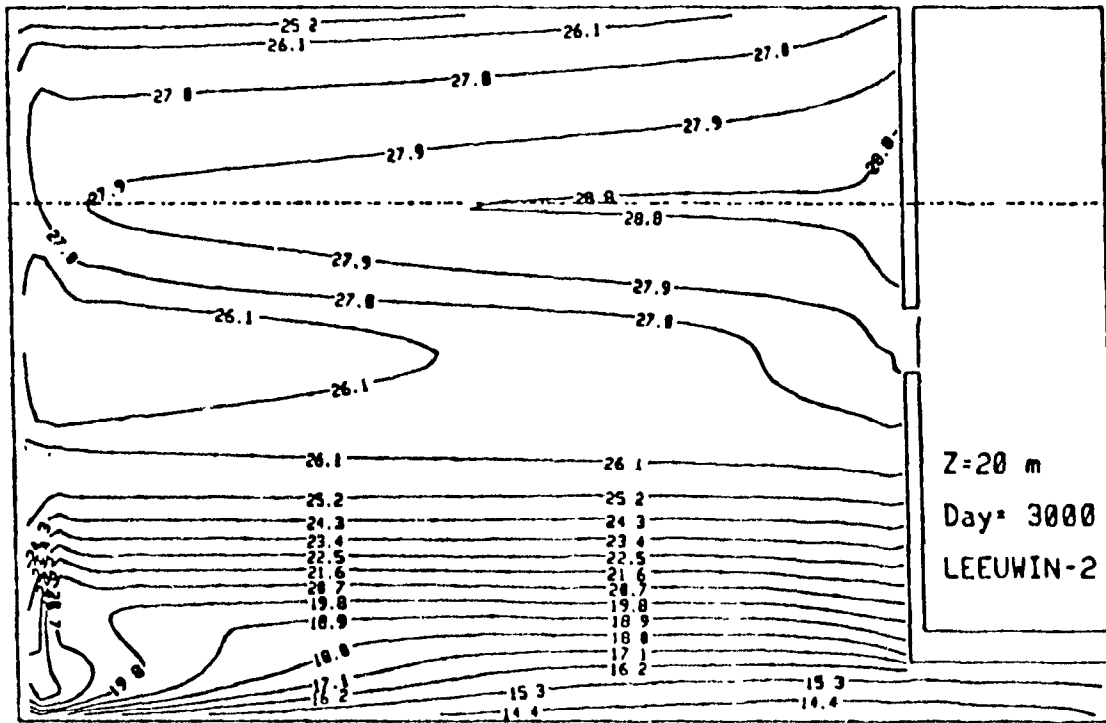


c

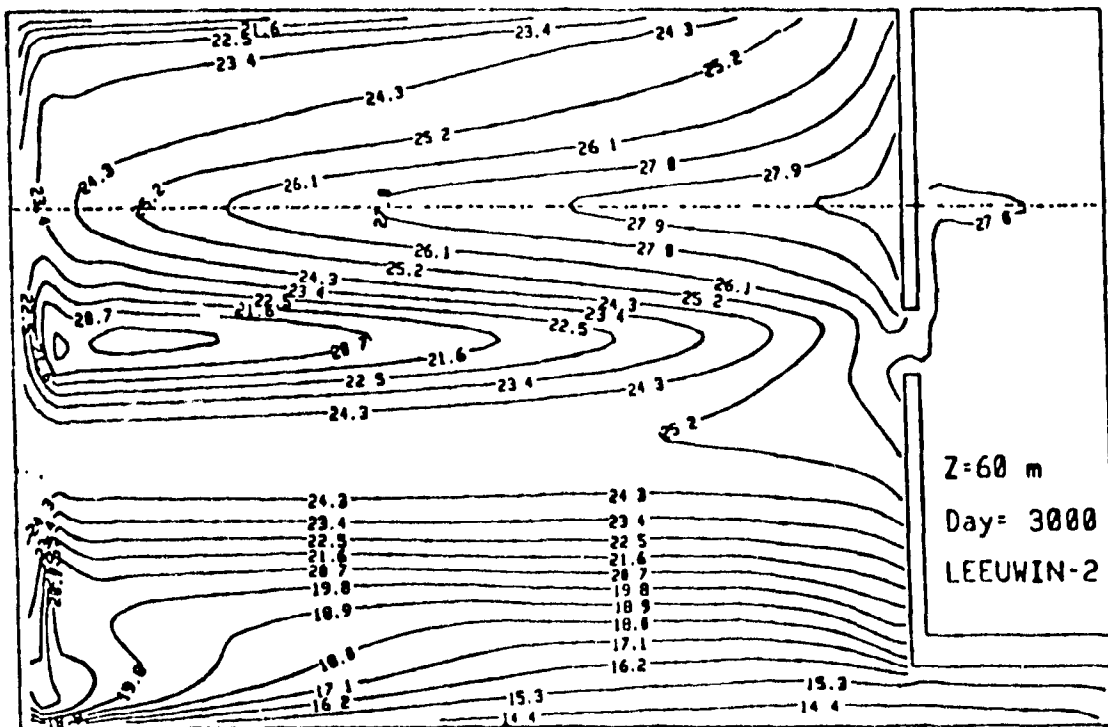


d

Fig.5.8. Cont. Horizontal velocities at $z=20\text{m}$ and $z=60\text{m}$ (levels 1 and 2): a) and b) Leeuwin-2 c) and d) Peru-2 (cf. Fig. 4.2).



a



b

Fig.5.9. Temperatures in °C at z=20m and z=60m (levels 1 and 2): a) and b) LEEUWIN-2 run c) and d) Peru-2 run (cf. Fig. 4.3).

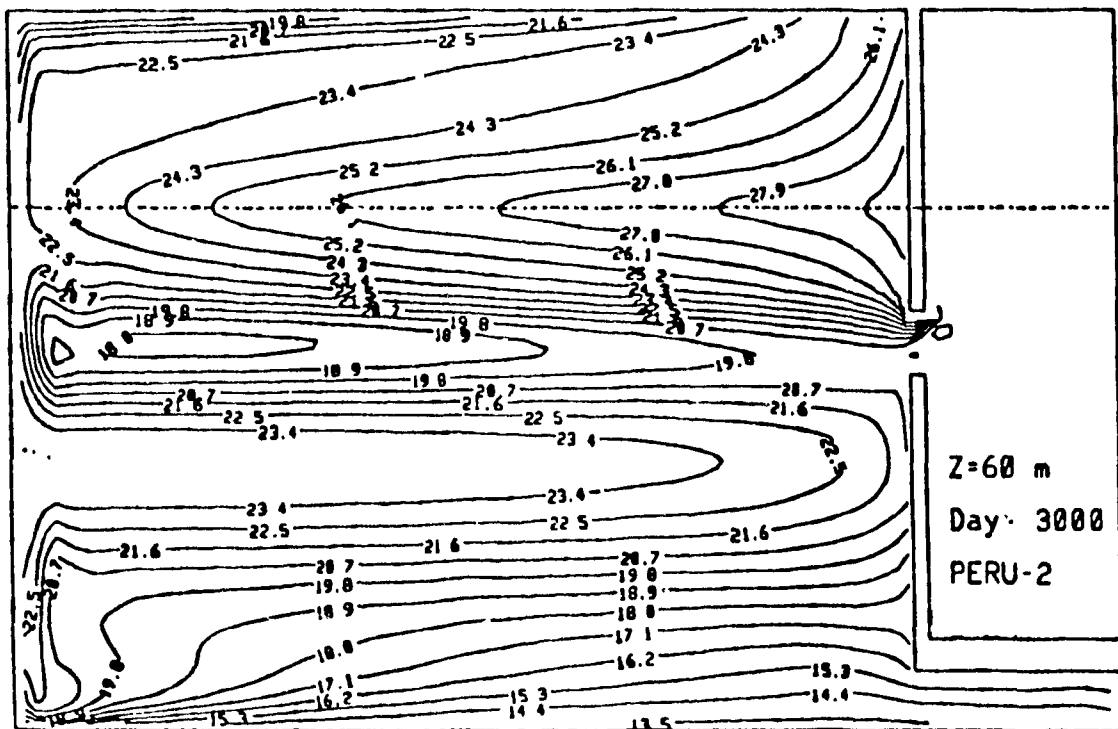
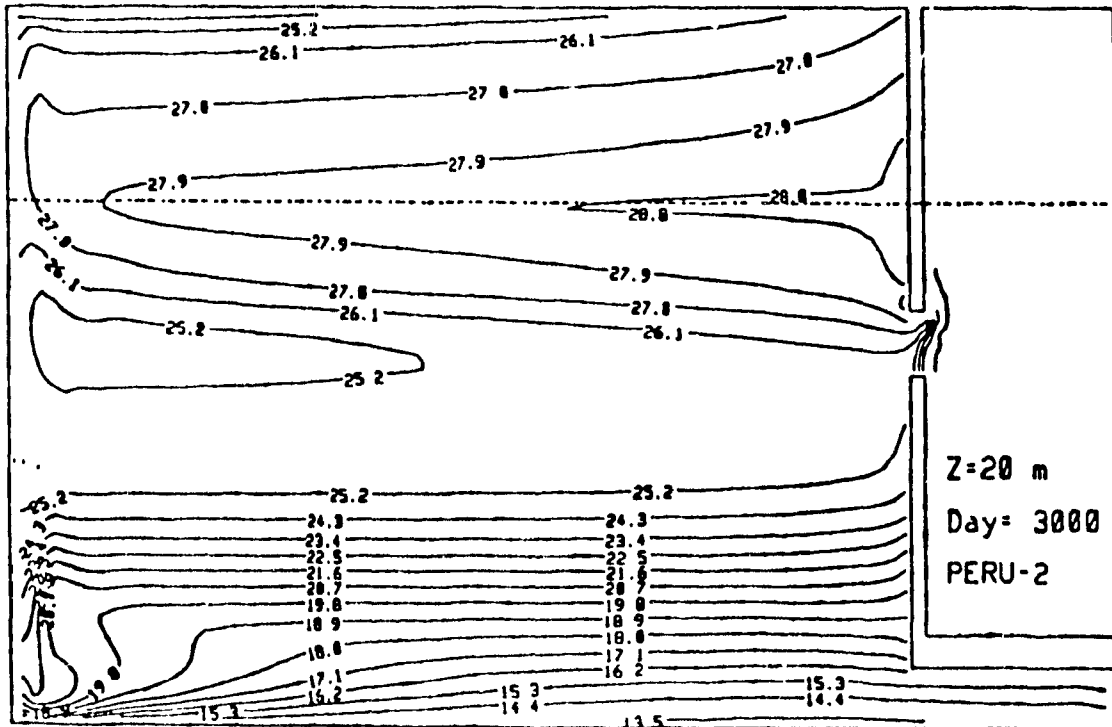


Fig.5 9. Cont. Temperatures in °C at z=20m and z=60m (levels 1 and 2): a) and b) Leeuwin-2 c) and d) Peru-2 (cf. Fig. 4.3).

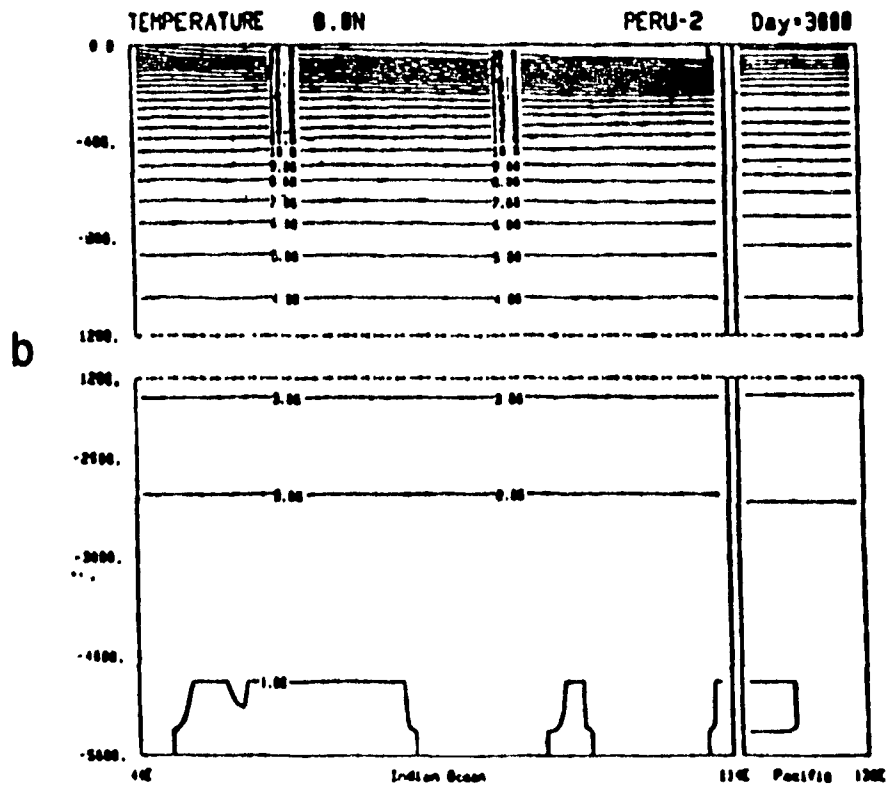
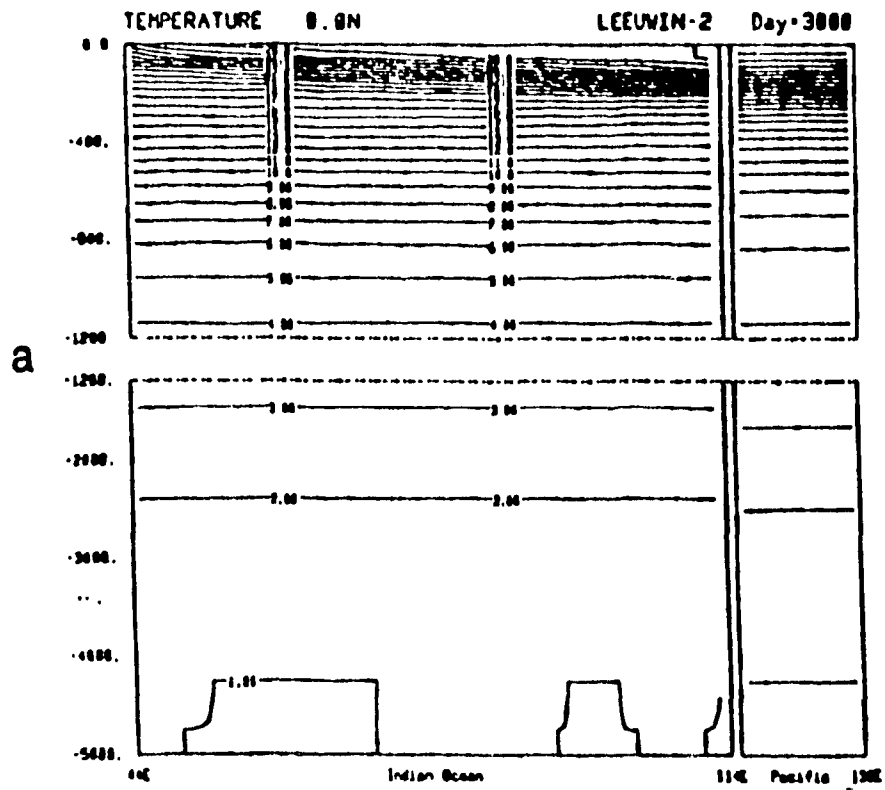


Fig.5.10. Zonal-vertical section of temperature (in °C) at 0°N: a) Leeuwin-2 run b) Peru-2 run (cf. Fig. 4.6).

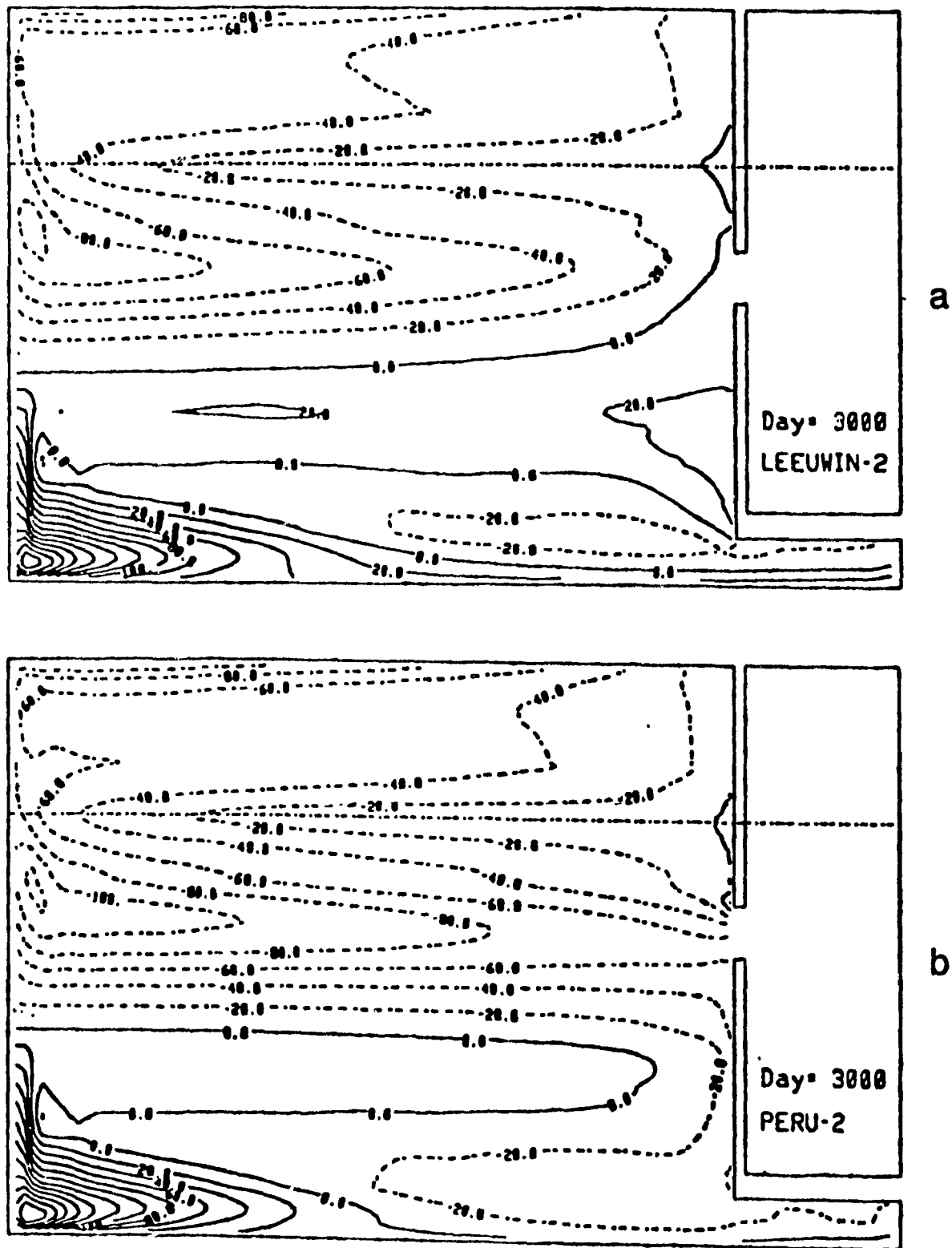
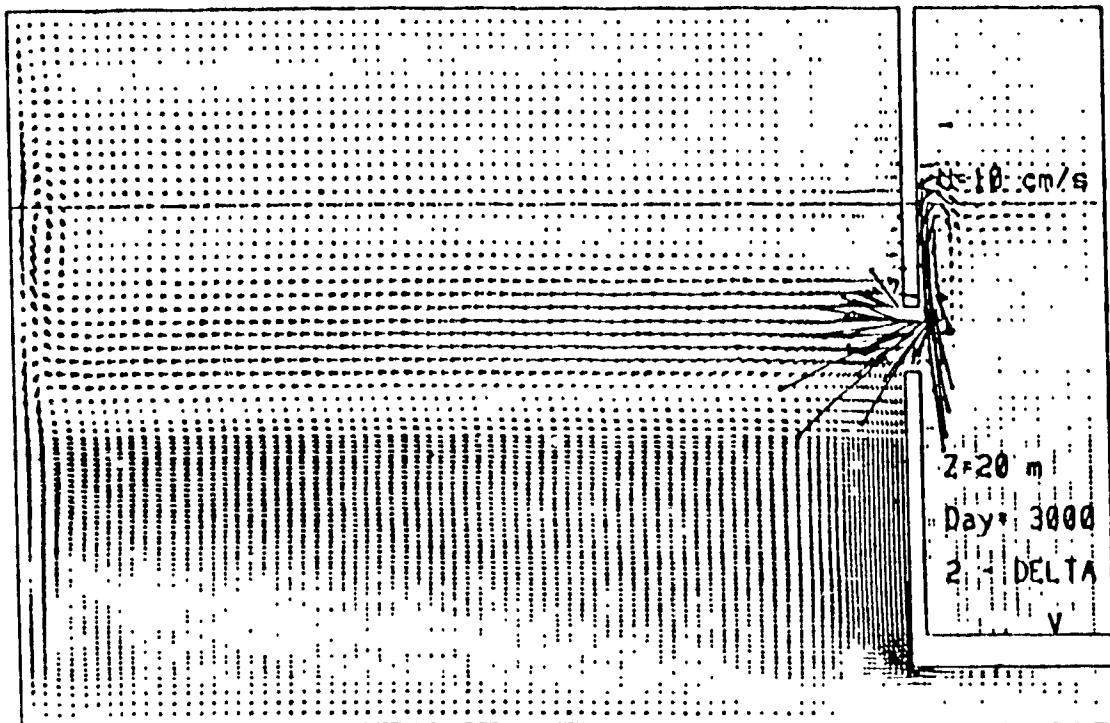


Fig.5.11. Surface heat fluxes in W/m^2 a) Leeuwin-2 run b) Peru-2 run. Positive (solid) contours indicate that heat is being released by the ocean (cf. Fig. 4.28).

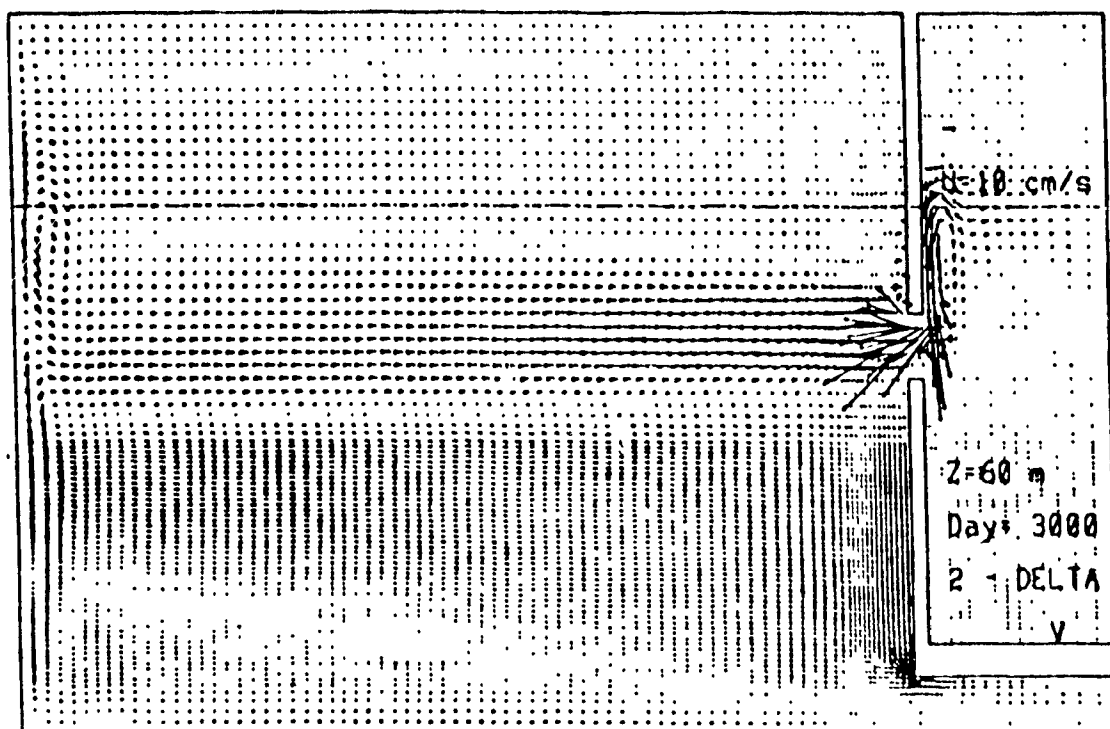
new ones (heat fluxes have been changed by about 20 W/m^2 negatively everywhere) because heat is diffused downward much more readily. In the Peru-2 run, there is now no positive heat flux anywhere along the eastern boundary. The total surface heating has doubled in both runs; the new mean surface heat fluxes are -16.8 W/m^2 for the Leeuwin-2 run and -29.9 W/m^2 for the Peru-2 run (Table 5). The heat budgets are even further from equilibrium. The throughflow in the Peru-2 run is even stronger (14.2 Sv compared to 7.7 Sv in the first Peru run) because the temperature jump between the two basins is being emphasized as the intermediate depths in the Indian Ocean are being warmed more efficiently. Nearly the same masses are exchanged in the two Leeuwin runs, but the mean temperature difference of the exchanged waters has been halved (because the surface of the new run is not as warm), while it has changed very little between the Peru and Peru-2 runs. The heat transport from the Indian Ocean to the Pacific is greater in the new Peru run but the heat transport in the other direction is less in the new Leeuwin run.

In the difference field (Fig 5.12), the thermohaline circulation is much more distinct now that the eddies have disappeared. The westward jet from the gap and the eastward flow towards Australia can now be seen to reach all the way to the western boundary. The poleward decay of the geostrophic onshore flow has lessened, but the western boundary currents are still only locally intensified. The differences in surface heat fluxes (Fig.5.13) at the Indonesian gap and along the eastern boundary are even larger, but once again, the warm and cool throughflows do not seem to be affecting the surface temperature along the western boundary. Furthermore, the difference in heat flux in the northwest and southwest corners has been reduced: the Leeuwin-2 run is barely warmer there than the Peru-2 run. However, the whole surface of the Indian Ocean in the Leeuwin-2 run is warmer than in the Peru-2 run, so heat from the Pacific is being spread over large areas, supporting our choice of initial condition in the first Leeuwin run. This can be seen even more clearly from the meridional-vertical sections (near the eastern boundary, in the interior and near the western boundary) shown in Fig.5.14. The deep oceans of the two runs are at the same temperature (unlike in Fig 4 18 where the Leeuwin run was 1°C warmer) but just below the surface, a layer nearly 700 metres thick

TABLE 5			
Heat Budgets			
	High viscosity runs		
	Leeuwin-2 run 3000 days	Peru-2 run 3000 days	Leeuwin-2 run 5000 days
Heat transport from Indian to Pacific in 10^{15} W			
i) by advection	-0.050	+0.953	+0.375
ii) by diffusion	0.0007	-0.003	-0.002
iii) total	-0.051	+0.956	+0.377
Total surface heating of the Indian Ocean in 10^{15} W	0.760	1.355	0.809
Mean surface heat flux into the Indian Ocean in W/m^2	16.80	29.92	17.88
Mean departure from Haney temperature in $^{\circ}C$	-0.467	-0.831	-0.497
Mass exchanged between Pacific and Indian Oceans in Sv	3.4	14.2	9.5
Mean temperature difference of the exchanged waters in $^{\circ}C$	3.6	16.8	9.9



a



b

Fig.5.12. Velocity difference (Leeuwin-2 - Peru-2) at a) $z=20\text{m}$ and b) $z=60\text{m}$ (levels 1 and 2) (cf. Fig. 4.6).

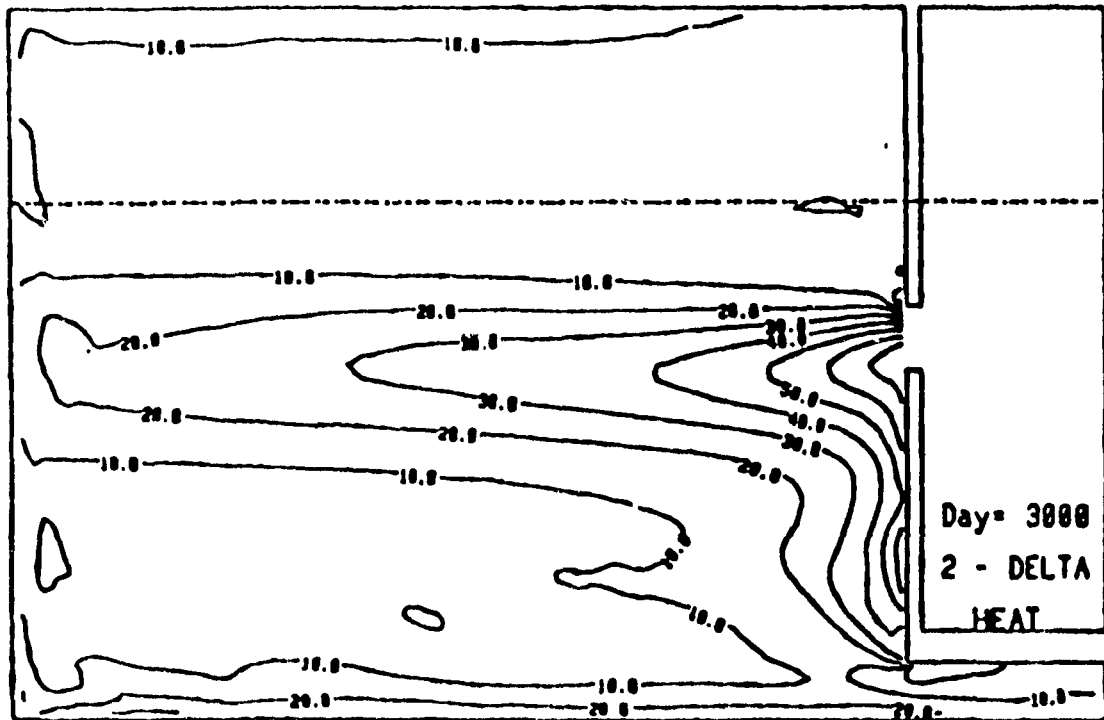


Fig.5.13. Difference in surface heat flux (Leeuwin-2 - Peru-2) in W/m^2 . Positive (solid) contours indicate that the Leeuwin-2 ocean is releasing more heat to the atmosphere (cf. Fig. 4.22).

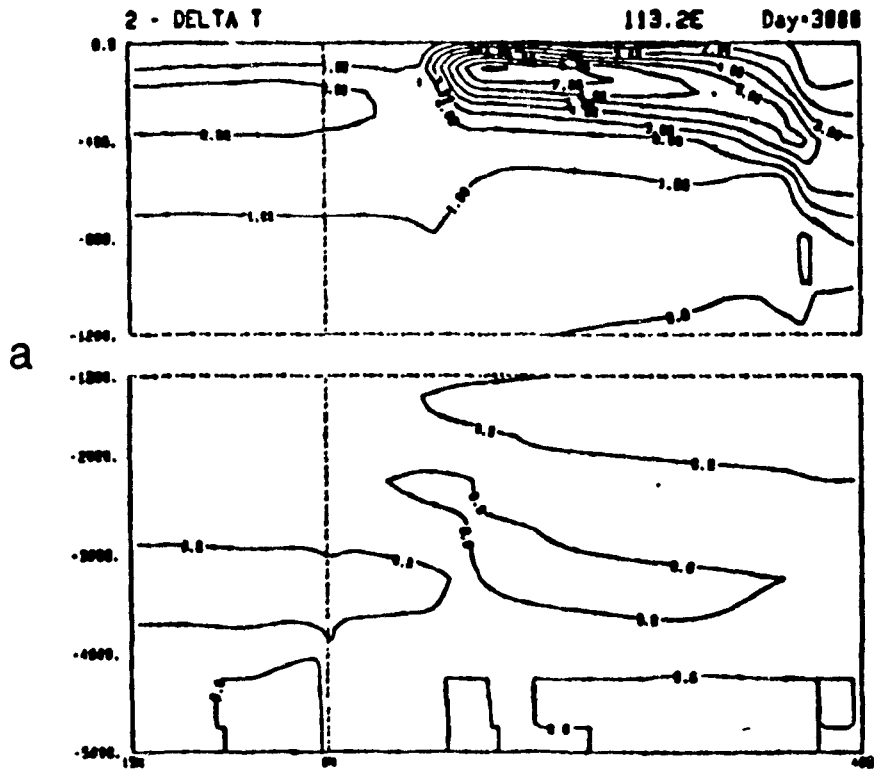


Fig.5.14. Difference in temperature (Leeuwin-2 - Peru-2) along a) $113.2^{\circ}E$ b) $74^{\circ}E$ c) $46^{\circ}E$ (cf. Fig. 4.18).

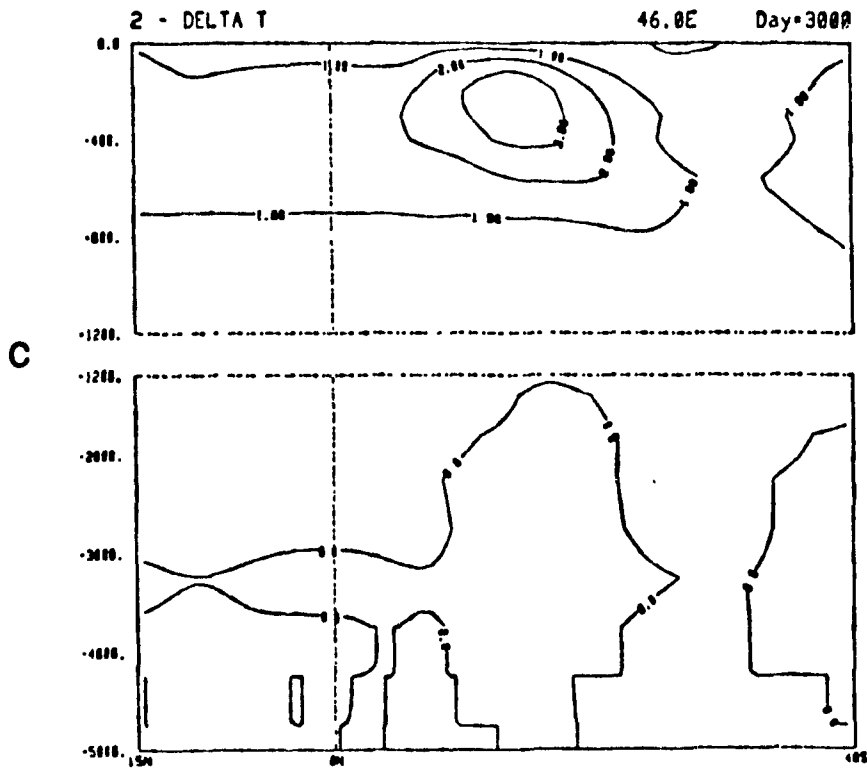
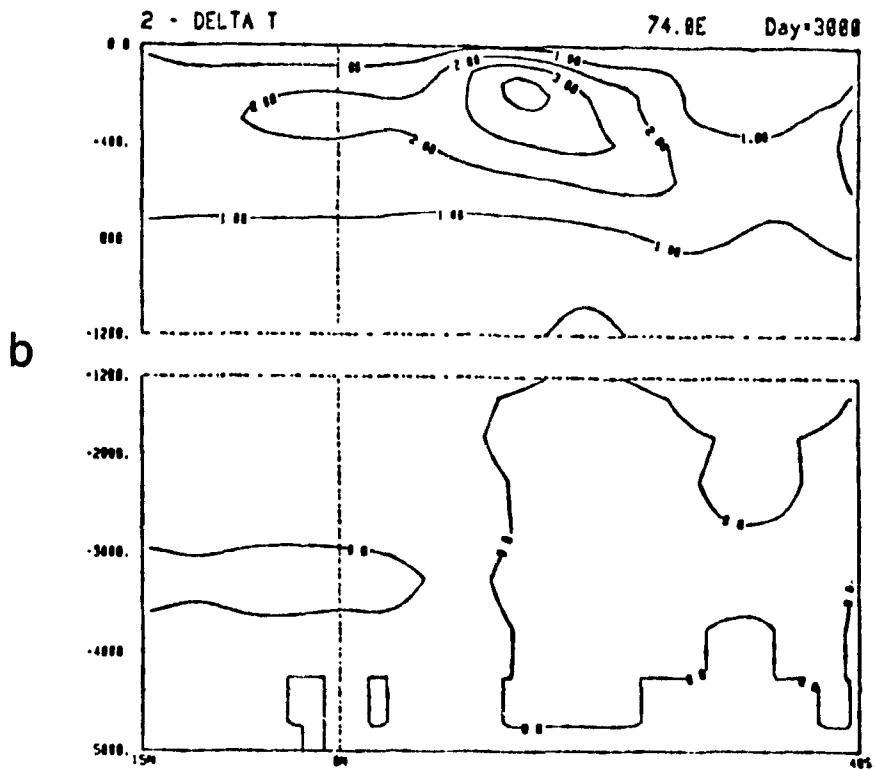
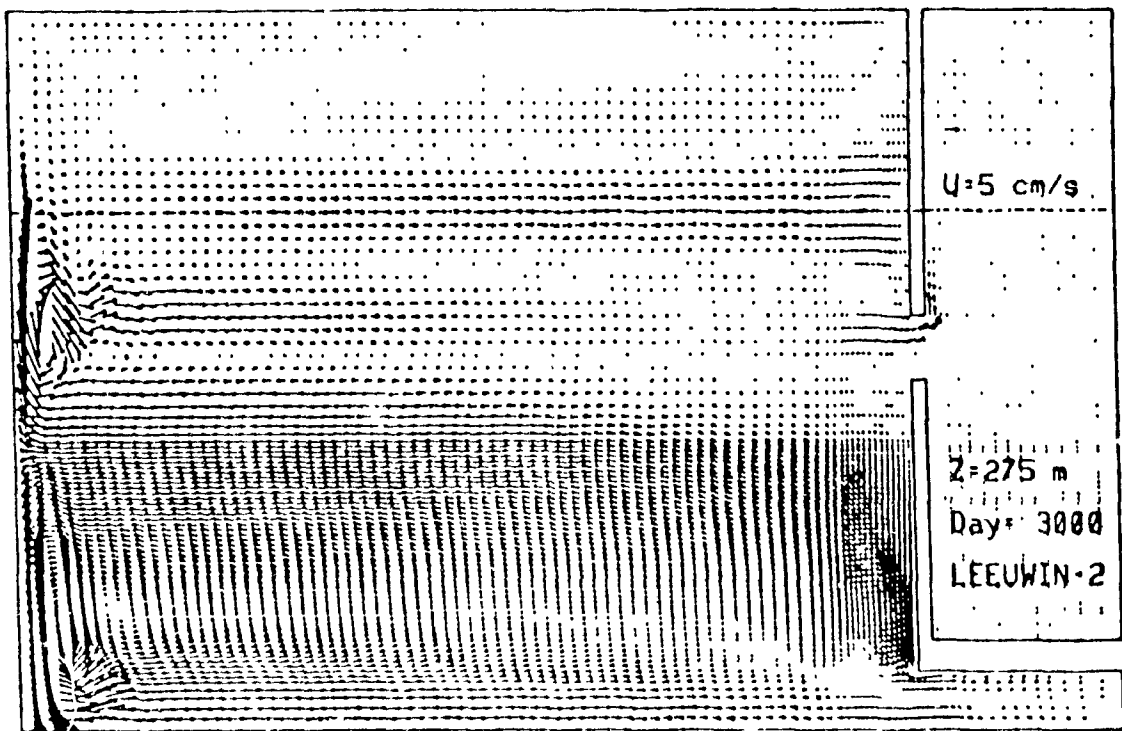


Fig.5.14. Cont. Difference in temperature (Leeuwin-2 - Peru-2) along a) 113.2°E b) 74°E c) 46°E (cf. Fig. 4.18).

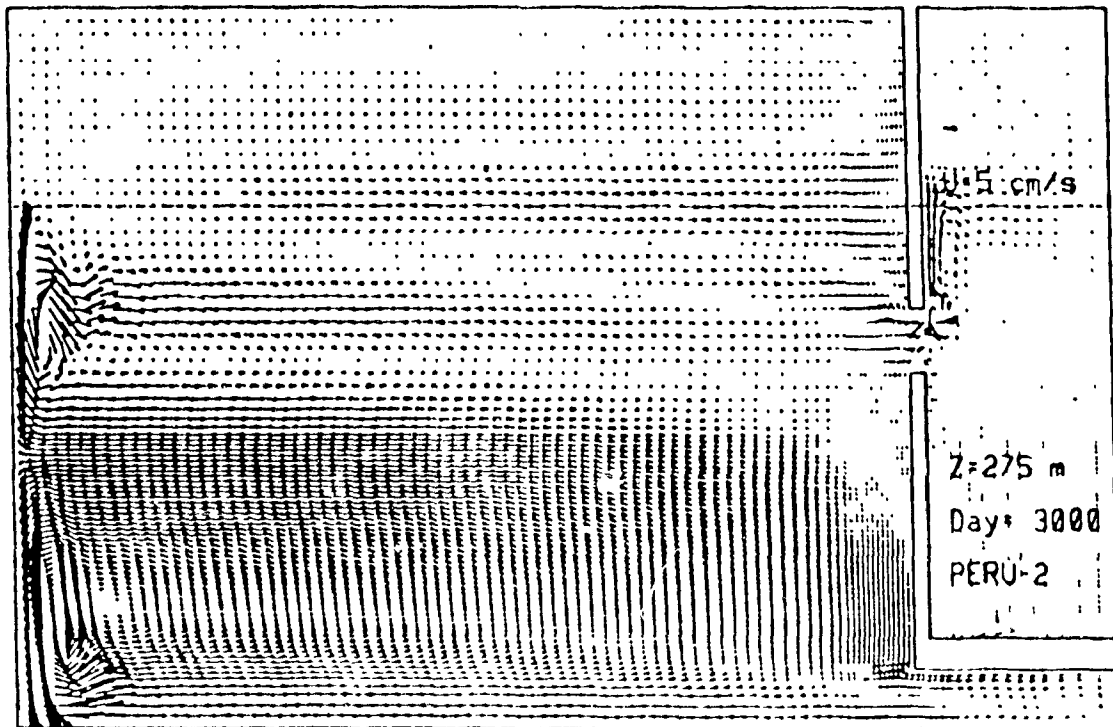
over the whole ocean has been heated by the warm throughflow. The South Equatorial Current is once again the carrier of the heat in tropical regions.

At $z=275\text{m}$, the offshore flow associated with the reversed meridional steric height gradient in the Leeuwin runs seems slightly weaker in the Leeuwin-2 run. We no longer see quite so distinctly the cold water tongue being advected northwestward from the eastern boundary (compare Figs 4.13a and 5.16a). (The salinity gradient along the coast is however greater as the throughflow is now fresher than the rest of the ocean) The deep ocean fields of T and S are very flat because of the higher diffusivity, but the higher baroclinic modes are now even more clearly seen in the deep ocean of the Leeuwin-2 run. The deep ocean of the Leeuwin-2 run is cooler than in the first run because of the different initial condition, but in the Peru-2 run, the whole ocean is now slightly warmer, because of the higher diffusivity. We still find a deep cell in the overturning streamfunction of the Peru run (Fig 5.17), but this seems to be due to the vertical velocities induced on the Pacific side of the Indonesian continent.

The oscillations in the kinetic energy have disappeared with the eddies (Fig.5.18). The total kinetic energy is also less in the new more viscous runs. The two peaks at less than 100 days and roughly 1400 days are related to the propagation of barotropic Rossby waves due to the wind forcing and 1st mode baroclinic waves. In both the new runs, the southward heat transport (Fig 5.19) is less. In the Peru-2 run, we actually find a band of northward heat transport between 3 to 13 °S. Only in the northern hemisphere, are the new runs actually transporting more heat southward. By comparing the northward heat transport at 2600 (not shown), 2800 (Fig.5.20) and 3000 days (Fig.5.19), we can get an indication of whether a steady-state has been reached. The Peru-2 run is in fact changing very little over this period. However, the Leeuwin-2 transport is still shrinking considerably and it was decided to allow the integration to continue another 2000 days for this reason. The meridional heat transport does then stabilize further but after 5000 days, the downwards diffusion of heat has become destructive. The intermediate depths are now so warm that the throughflow at the Indonesian gap has actually reversed direction! The meridional steric height gradient along the

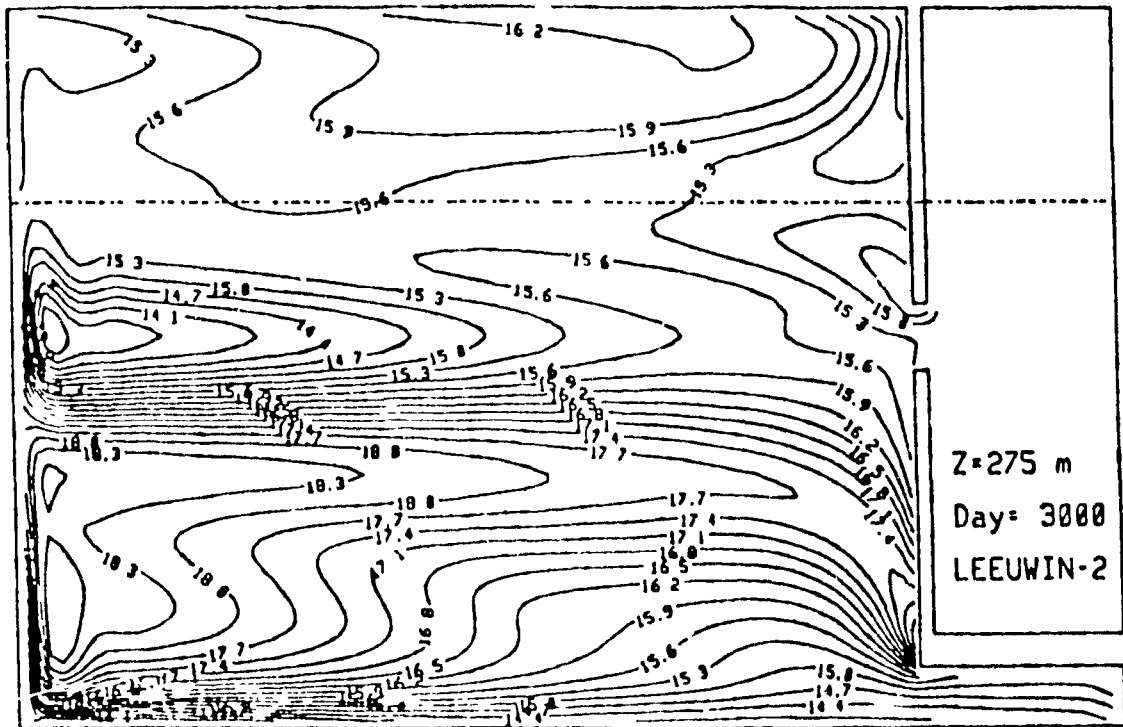


a

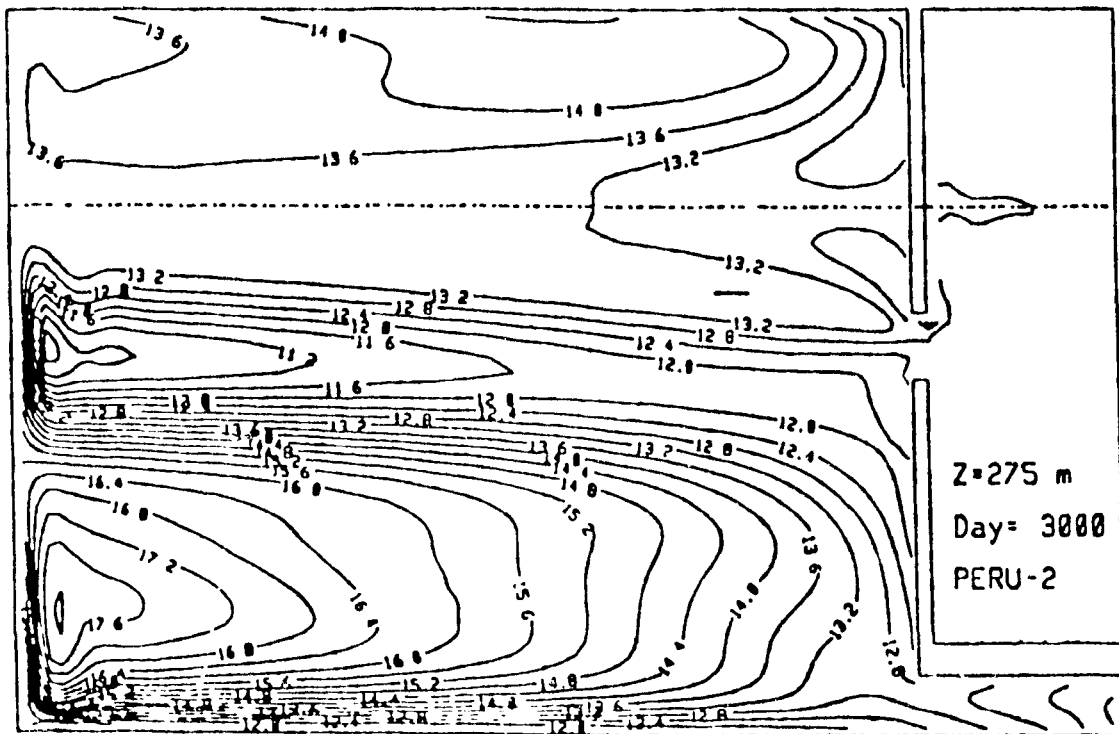


b

Fig 5.15 Horizontal velocities at $z=275\text{m}$ (level 5): a) Leeuwin-2 run b) Peru-2 run (cf. Fig. 4 11).

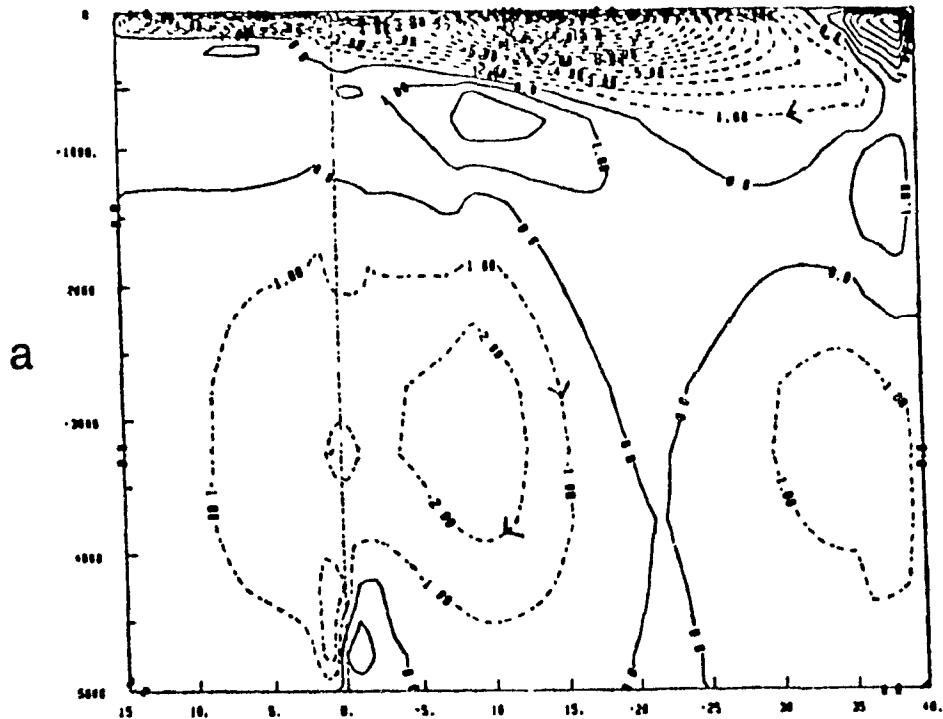


a

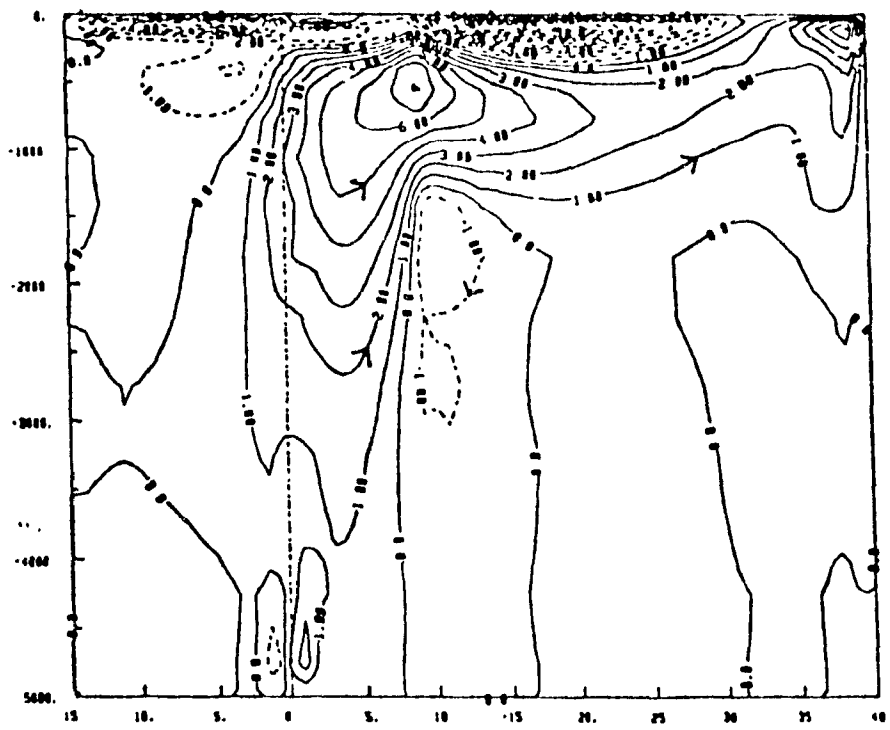


b

Fig 5.16. Temperatures in °C at $z=275\text{m}$ (level 5): a) Leeuwin-2 run b) Peru-2 run (cf. Fig. 4.13).



a



b

Fig.5.17. Overturning (zonally-integrated) streamfunction in Sv as a function of latitude for a) the Leeuwin-2 run b) the Peru-2 run (cf. Fig. 4.4).

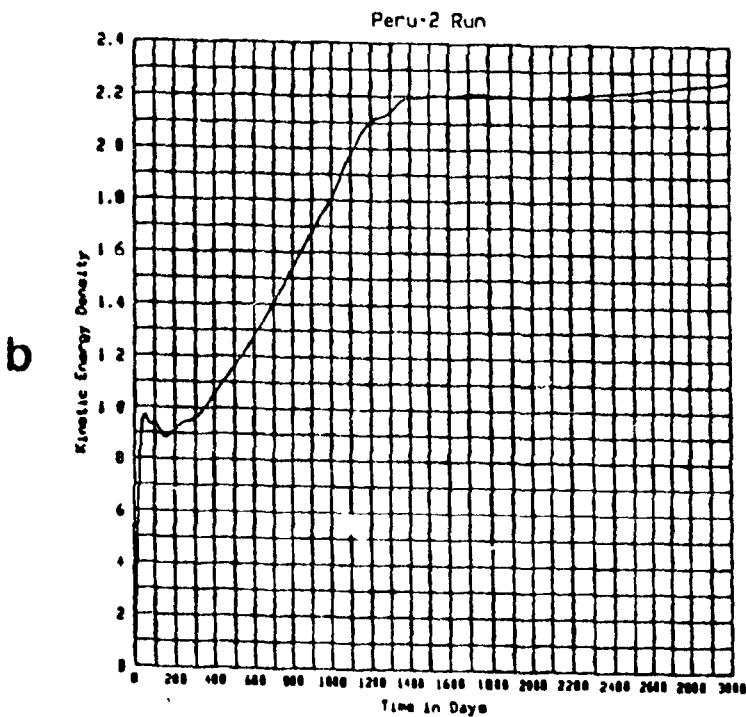
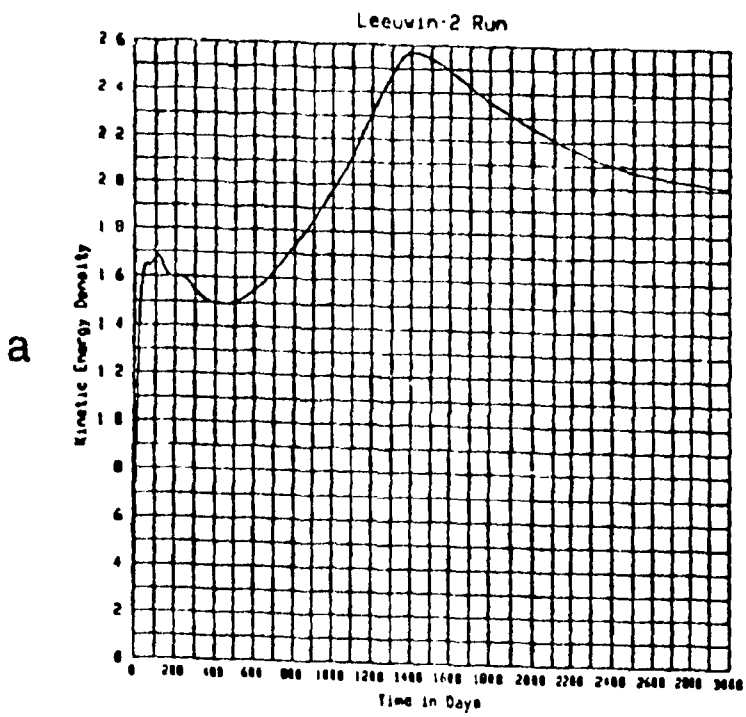
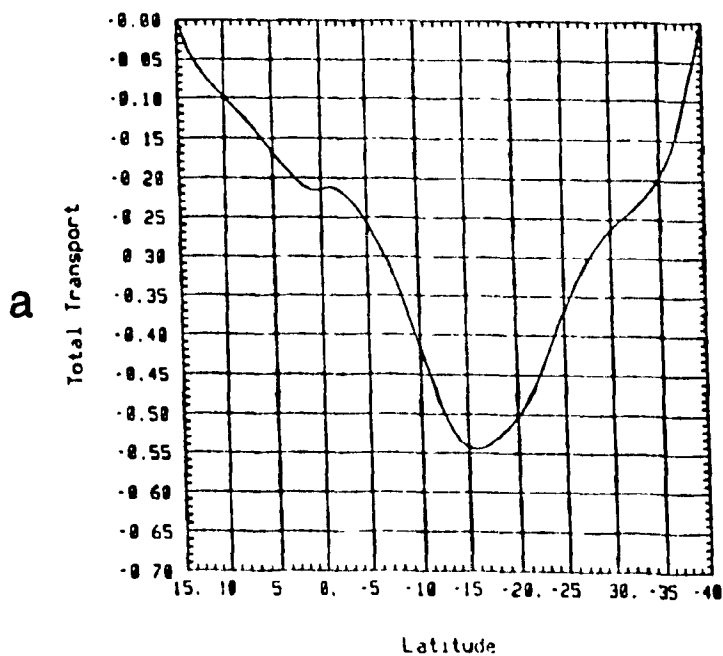


Fig.5.18. Kinetic energy density in 10^{-1} kg/m s^2 for a) the Leeuwin-2 run b) the Peru-2 run (cf. Fig. 3.6).

Leeuwin-2 Heat Transport Day=3000



Peru-2 Heat Transport Day=3000

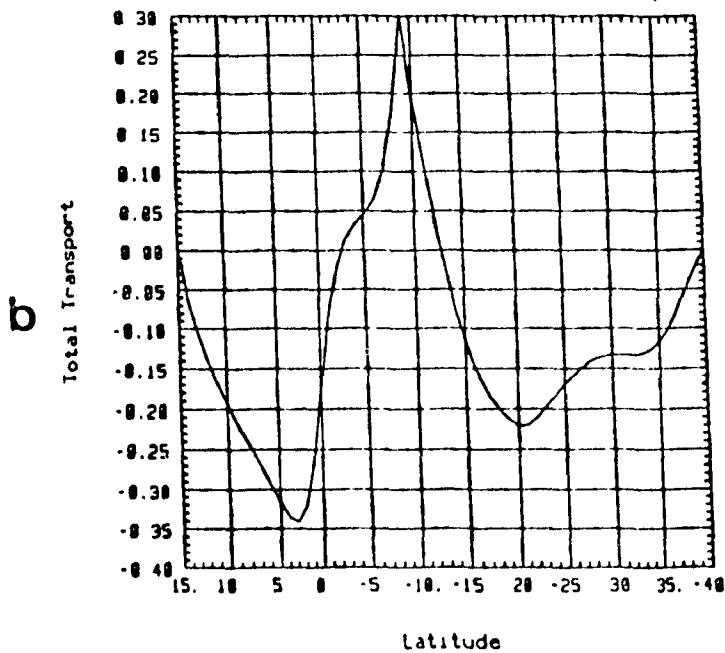
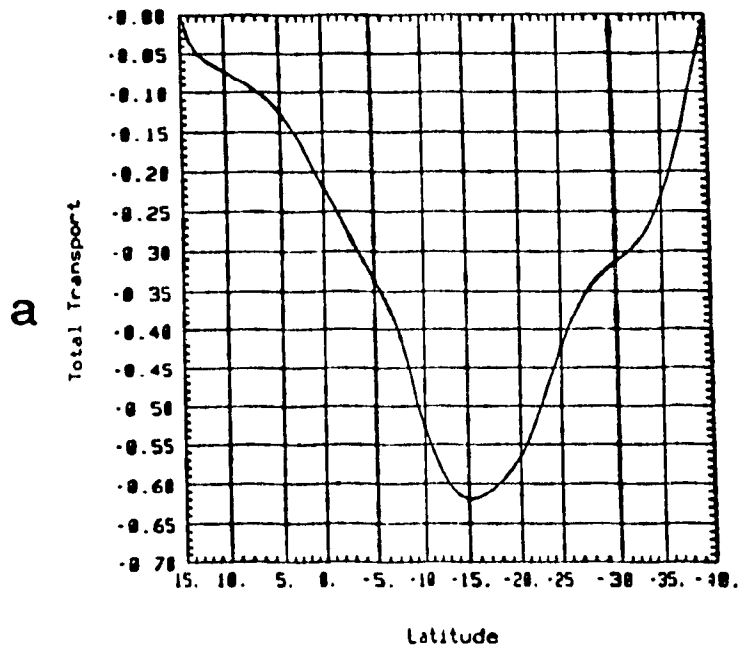


Fig.5.19. Total northward heat transport in 10^{15} W for a) the Leeuwin-2 run b) the Peru-2 run (cf. Fig. 4.23a).

Leeuwin-2 Heat Transport Day=2800



Peru-2 Heat Transport Day=2800

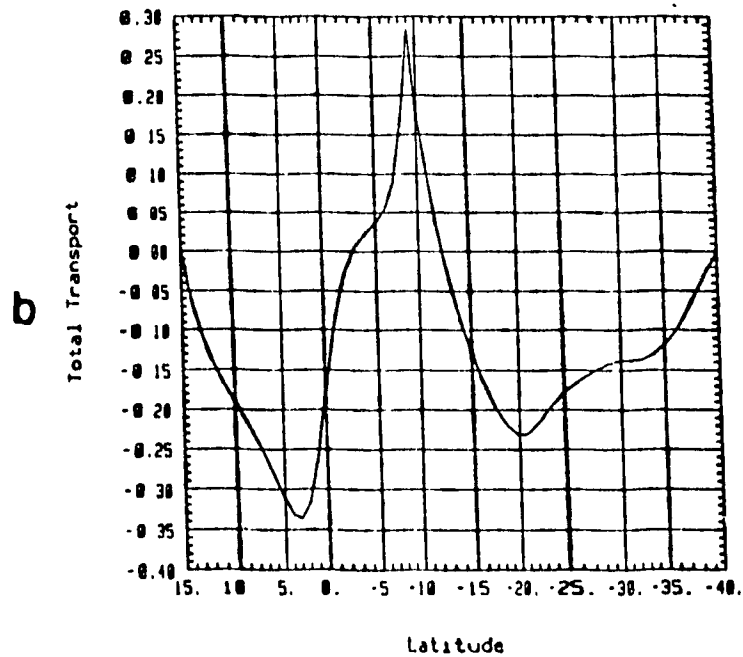


Fig.5.20. Total northward heat transport in 10^{15} W at 2800 days for a) the Leeuwin-2 run b) the Peru-2 run.

eastern boundary is still producing the onshore flow and downwelling typical of the Leeuwin Current, but the Indian Ocean is now a net exporter of heat to the Pacific. The overturning streamfunction is evolving a deep cell similar to that in the Peru-2 run. The kinetic energy is increasing again (albeit very slowly).

The results described in this section tend to weaken our confidence in our curves of meridional heat transport. However, the similarities between the surface heat flux maps of the new and old Leeuwin runs are reassuring as to the validity of the initial condition in the first Leeuwin run. Besides speeding up the equilibrium process, matching the initial temperature profile of the Indian Ocean basin to that of the Pacific reservoir minimized the difficulties with downwards diffusion of heat from the thermally forced surface - in the absence of a cold water source - which started to become important in the second run.

6. SUMMARY AND CONCLUSIONS

In this study, the Indian Ocean was modelled (using the Cox, 1984 version of the Bryan-Cox Ocean General Circulation Model) as a rectangular flat-bottomed ocean 5 km deep and separated from an idealized Pacific Ocean by two narrow land barriers representing the Indonesian and Australian 'continents'. The artificial Pacific in these simulations was simply a reservoir restored to chosen vertical profiles of salinity and temperature throughout the integration. The two basins were linked by a single near-equatorial channel 1200 m deep. The surface temperatures in the Indian Ocean basin were restored towards a latitude-dependent Haney-type atmospheric temperature; no direct salinity forcing was however imposed as this was expected to be of secondary importance (Godfrey and Weaver, 1991). The magnitude of the real net mass throughflow into the Indian Ocean is still uncertain, so only the purely thermohaline circulation induced by warm surface waters flowing through the gap in one direction and cooler waters balancing them at depth was considered here. Although the depth integral of the model throughflow vanishes, a sizeable exchange of mass between the Pacific and Indian Oceans and a net transport of heat from one basin to the other were produced.

The goal of the experiments was to compare the effect on the climate of the Indian Ocean of two different TS profiles in the model Pacific. The Pacific reservoir was restored to either a warm profile with a fresh surface layer representative of the Indonesian seas or the western equatorial Pacific (the 'Leeuwin run') or to a cooler more saline profile more typical of the eastern equatorial Pacific (the 'Peru run'). Godfrey and Weaver (1991) used a very similar model for the eastern boundary region to show that the warm fresh throughflow near the equator is the cause of the unique large meridional steric height gradient off western Australia. This is geostrophically balanced by a zonal onshore flow which turns south at the coast to form the anomalous poleward-flowing Leeuwin Current. G-W found that simply replacing the warm TS profile in the 'Pacific' by the cooler one resembling the waters off South America was enough to change the coastal circulation to a more typical equatorward eastern

boundary current (such as the Peru current at corresponding latitudes in the eastern Pacific). In their model, this also had a major impact on the surface heat fluxes along the Australian coast, where the southward transport of heat by the Leeuwin Current is considered to be a crucial factor in moderating the local climate (see for example, Weaver, 1990).

In the present study, the domain was expanded to include the whole Indian Ocean north of 40°S, and especially the northern hemisphere, an area of large heat gain by the ocean. Annual mean winds were also imposed. It was found that the warm throughflow in the Leeuwin run drives a basinwide thermohaline circulation very similar to that proposed by G-W. The westward surface flow through the gap feeds the model South Equatorial Current and warm water is transported all the way across the ocean to the western boundary. The enhanced steric height at low latitudes causes an eastward return flow south of the SEC, intensifying as it nears the eastern boundary. This purely thermohaline circulation can only be seen by comparing the two runs (Leeuwin and Peru) as it is masked by the stronger Sverdrup circulation in most regions. The exception is at the eastern boundary where it is manifested as the buoyancy-driven Leeuwin Current.

At the southern tip of Australia, the release of heat to the atmosphere at the surface of the ocean causes the upper part of the water column to become unstable. Warm water is then mixed downward by convection. At intermediate depths, the steric height along the coast therefore increases poleward, driving a northwestward flow back into the interior which travels back across the ocean, reflects off the western boundary and feeds into an eastward undercurrent for the SEC, effectively tracing out the reverse path of the warm water at the surface.

The circulation described above depends critically on the presence of the warm throughflow. The cooler profile of the Pacific reservoir in the Peru run (corresponding to more typical conditions for the eastern boundary of an ocean) leads to a reversal of the throughflow (which now contributes negatively to the SEC) and destroys the meridional steric height gradient driving the eastward flow south of the SEC.

This also suggests an alternative route to the "warm water path" described by Gordon (1986) in

which the warm water transported by the SEC passes into the western boundary current flowing southward along Africa, a fraction of which then escapes into the South Atlantic. In our model, the western boundary current is enhanced only slightly by the warm throughflow and the difference in surface heat flux between the two runs is negligibly small. The effect of the warm throughflow is rather to increase the surface temperature in a wide band extending zonally right across the ocean and centred on the SEC (although the difference in temperature does diminish westward), as well as along the eastern boundary (the site of the largest difference in surface heat flux). Over the rest of the domain, the surface of the Indian Ocean in the Leeuwin run is always slightly warmer, and especially in regions of upwelling since the temperature stratification in the upper layers of the Peru run is greater. The total surface heating by the atmosphere is more than doubled in the cooler Peru run. This is evidence that the Indonesian throughflow does indeed significantly contribute to the exceptionally warm climate of the Indian Ocean.

The model is also shown to produce meridional heat transports of the same order of magnitude as those observed in the Indian Ocean. The forcing by a warm throughflow further increases the resemblance to reality.

Another aspect of the model results discussed are the synoptic scale barotropic eddies that are generated in the western quarter of the basin by shear instability in the South Equatorial Current. While this is not one of the central results of this thesis, it is interesting to note that a number of other authors have reported barotropic instability in both models of the western Indian Ocean (e.g. Schott et al., 1988; Woodberry et al., 1989) and actual data from the region (e.g. Schott et al., 1988; Kindle and Thompson, 1989). Although the periods and wavelengths recorded by these authors tend to be shorter than in our model, this may be associated with the relatively high horizontal viscosity A_{HV} .

The eddies have the further consequence of seriously influencing the meridional heat transport, so compromising our analysis of the heat budget. For this reason, and to resolve a numerical problem associated with an effective negative vertical diffusivity in a region of strong downwelling, two additional runs were performed, with increased vertical viscosity and diffusivity. A different initial

I
condition in the Indian Ocean of the new Leeuwin run also allowed us to check that the surface heat fluxes at the end of the integration were not being unduly biased by the initial temperature profile

The single most important improvement that could be added to the model would be to allow a net mass throughflow from the Pacific. Other factors that might be explored would be the effects of salinity forcing by precipitation and evaporation at the surface and by the distinctive water masses of the northern seas, of the real topography of the sea floor and coastline, and of the seasonal variations in the wind-driving and the strength of the throughflow. Although the source of deep water from the South Pole would be an important influence in more extensive climate studies, the transport of heat across 40°S in the Indian Ocean is not so large that the imaginary barrier at that latitude in our model is a serious impediment.

REFERENCES

- Batteen, M.L. and M.J. Rutherford, 1990: Modelling studies of eddies in the Leeuwin Current: the role of thermal forcing. *J. Phys. Oceanogr.*, 20, 1484-1520.
- Boland, F.M., J.A. Church, A.M.G. Forbes, J.S. Godfrey, A. Huyer, R.L. Smith and N.J. White, 1988: Current meter data from the Leeuwin Current Interdisciplinary Experiment. CSIRO Marine Laboratories Report No. 198.
- Bryan, F.O., 1986. Maintenance and variability of the thermohaline circulation. Ph.D. Thesis. Princeton University.
- Bryan, K., S. Manabe and R.C. Pacanowski, 1975: A global ocean-atmosphere climate model. Part II. The oceanic circulation. *J. Phys. Oceanogr.*, 5, 30-46.
- , and L.J. Lewis, 1979: A water mass model of the world ocean. *J. Geophys. Res.*, 84, 2503-2517.
- Church, J.A., G.R. Cresswell and J.S. Godfrey, 1989: The Leeuwin Current. In Neshyba, S. (ed), *Poleward Flows Along Eastern Boundaries*. Springer-Verlag, in press.
- Cox, M.D., 1975: A baroclinic numerical model of the world ocean: Preliminary results. In *Numerical Models of Ocean Circulation*. National Academy Press, Washington, 364 pp.
- , 1980: Generation and propagation of 30-day waves in a numerical model of the Pacific. *J. Phys. Oceanogr.*, 10, 1168-1186.
- , 1984: A primitive equation, three-dimensional model of the ocean. GFDL Ocean Group Technical Report No. 1.
- Cresswell, G.R. and T.J. Golding, 1980: Observations of a south-flowing current in the southeastern Indian Ocean. *Deep-Sea Research*, 27A, 449-466.
- Fine, R.A., 1985: Direct evidence using tritium data for throughflow from the Pacific into the Indian Ocean. *Nature*, 315, 478-480.
- Fu, L., 1986: The general circulation and meridional heat transport of the South Atlantic determined by inverse methods. *J. Phys. Oceanogr.*, 11, 1171-1193.
- Gill, A.E., 1982: *Atmosphere-Ocean Dynamics*. Academic Press, 662 pp.
- Godfrey, J.S. and T.J. Golding, 1981: The Sverdrup relation in the Indian Ocean, and the effect of Pacific-Indian Ocean throughflow on Indian Ocean circulation and on the East Australian Current. *J. Phys. Oceanogr.*, 11, 771-779.
- , and K.R. Ridgway, 1985: The large-scale environment of the poleward-flowing Leeuwin Current, Western Australia: Longshore steric height gradients, wind stresses and geostrophic flow. *J. Phys. Oceanogr.*, 15, 481-495.
- , 1989: A Sverdrup model of the depth-integrated flow for the world ocean allowing for island circulations. *Geophys. Astrophys. Fluid Dynamics*, 45, 89-112.
- , and A.J. Weaver, 1991: Is the Leeuwin Current driven by Pacific heating and winds? *Prog. Oceanog.*, in press.
- Gordon, A.L. and A.R. Piola, 1983: Atlantic Ocean upper layer salinity budget. *J. Phys. Oceanogr.*, 13, 1293-1300.
- , 1986: Interocean exchange of thermocline water. *J. Geophys. Res.* 91(C4), 5037-5046.

- Haney, R.L., 1971: Surface thermal boundary condition for ocean circulation models. *J. Phys. Oceanogr.*, 1, 241-248.
- Hastenrath, S., 1980: Heat budget of tropical ocean and atmosphere. *J. Phys. Oceanogr.*, 10, 159-170
- Holland, W.R., 1973: Baroclinic and topographic influences on the transport in western boundary currents. *Geophys. Fluid Dynamics*, 4, 187-210.
- Hsiung, J., 1985: Estimates of global oceanic meridional heat transport. *J. Phys. Oceanogr.*, 15, 1405-1413.
- Kindle, J.C., G.W. Heburn and R.C. Rhodes, 1986: An estimate of the Pacific to Indian Ocean throughflow from a global numerical model. In Katz, E. and J. Witte (eds), *Further Progress in Equatorial Oceanography*. Nova University Press, Fla., pp 317-320.
- and J.D. Thompson, 1989: The 26- and 50-Day oscillations in the Western Indian Ocean Model results. *J. Geophys. Res.*, 94(C4), 4721-4736.
- Knox, R.A. and D.L.T. Anderson, 1985: Recent advances in the study of the low-latitude ocean circulation. *Prog. Oceanog.* 14, 259-318.
- Kundu, P.K. and J.P. McCreary, Jr., 1986: On the dynamics of the throughflow from the Pacific into the Indian Ocean. *J. Phys. Oceanogr.*, 16, 2191-2198.
- Leblond, P.H. and L.A. Mysak, 1978: *Waves in the Ocean*, Elsevier, 602 p.
- Levitus, S., 1982: *Climatological Atlas of the World Ocean*. NOAA Professional Paper 13. US Department of Commerce: National Oceanic and Atmospheric Administration
- Luther, M.E., 1987: Indian Ocean modelling. In Katz, E. and J. Witte (eds), *Further Progress in Equatorial Oceanography*. Nova University Press, Fla., pp 303-316
- McCreary, J.P., S.R. Shetye and P.K. Kundu, 1986: Thermohaline forcing of eastern boundary currents With application to the circulation off the west coast of Australia. *J. Marine Research*, 44, 71-92
- Moore, D.W. and J.P. McCreary, Jr., 1990: Excitation of intermediate-frequency equatorial waves at a western ocean boundary: With application to observations from the Indian Ocean *J. Geophys. Res.*, 95(C4), 5219-5231.
- Mysak, L.A. and Mertz, G.J., 1984: A 40- to 60-day oscillation in the source region of the Somali Current during 1976. *J. Geophys. Res.*, 89, 711-715.
- Oberhuber, J.M., 1988: *An Atlas Based on the "COADS" Data Set: The Budgets of Heat, Buoyancy and Turbulent Kinetic Energy at the Surface of the Global Ocean*. Max Planck Institut fur Meteorologie, Report No. 15.
- Philander, S.G.H., 1978: Instabilities of zonal equatorial currents, 2. *J. Geophys. Res.*, 83, 3679-3682.
- Pickard, G.L. and W.J. Emery, 1982: *Descriptive Physical Oceanography*. Pergamon Press, 249 pp
- Pond, S. and G.L. Pickard, 1983: *Introductory Dynamical Oceanography*. Pergamon Press, 329 pp
- Quadfasel, D.R. and J.C. Swallow, 1986: Evidence for 50-day period planetary waves in the South

- Equatorial Current of the Indian Ocean. *Deep-Sea Research*, 33, 1307-1312.
- Ross, D.A., 1988 *Introduction to Oceanography*. Prentice-Hall, 478 pp.
- Schott, F., M. Fieux, J. Kindle, J. Swallow and R. Zantopp, 1988: The boundary currents east and north of Madagascar - 2. Direct measurements and model comparisons. *J. Geophys. Res.*, 93, 4963-4974.
- Semtner, A.J., Jr., 1986: Finite-difference formulation of a world ocean model. In J.J. O'Brien (ed), *Advanced Physical Oceanographic Numerical Modelling*, D.Reidel Publishing Company, pp 187-202.
- Stommel, H.M., 1965: *The Gulf Stream: A Physical and Dynamical Description*. Berkeley, University of California Press, 248 pp.
- Talley, L.D., 1984. Meridional heat transport in the Pacific Ocean. *J. Phys. Oceanogr.*, 14, 231-241.
- Thompson, R.O R.Y., 1987: Continental-shelf-scale model of the Leeuwin Current. *J. Marine Research*, 45, 813-827.
- Toggweiler, J.R., K. Dixon and K. Bryan, 1989: Simulations of radiocarbon in a coarse-resolution world ocean model. 2. Distributions of bomb-produced carbon 14. *J. Geophys. Res.*, 94 (C6), 8243-8264.
- Weaver, A.J and J.H. Middleton, 1989: On the dynamics of the Leeuwin Current. *J. Phys. Oceanogr.*, 19, 626-648.
- , 1990: Ocean currents and climate. *Nature*, 347, p.432.
- , and J.H. Middleton, 1990 An analytic model for the Leeuwin Current off Western Australia. *Cont. Shelf Res.*, 10, 105-122.
- , and E.S. Sarachik, 1990: On the importance of vertical resolution in certain ocean general circulation models. *J. Phys. Oceanogr.*, 20, 600-609.
- Woodberry, K., M. Luther and J.O'Brien, 1989: The wind-driven seasonal circulation in the southern tropical Indian Ocean. *J. Geophys Res.* 94, 17985-18002.
- Wyrtki, K., 1961a: Physical oceanography of the Southeast Asian waters: Scientific results of maritime investigations of the South China Sea and Gulf of Thailand 1959-1961. NAGA Report 2, Scripps Institute of Oceanography, California, 195 pp.
- , 1961b: The thermohaline circulation in relation to the general circulation in the oceans. *Deep-Sea Research*, 8, 39-64.
- Yin, F.L. and I.Y. Fung, 1990: On the net diffusivity and viscosity in some numerical ocean general circulation models. *J. Geophys. Res.*, submitted.